Urban Wind Modeling with Application to Autonomous Flight

by

David Galway

A Thesis submitted to
the Faculty of Graduate Studies and Research
in partial fulfillment of
the requirements for the degree of
Master of Applied Science

Ottawa-Carleton Institute for
Mechanical and Aerospace Engineering

Department of Mechanical and Aerospace Engineering
Carleton University
Ottawa, Ontario, Canada

April 2009

The undersigned recommend to

the Faculty of Graduate Studies and Research

acceptance of the Thesis

Urban Wind Modeling with Application to Autonomous Flight

Submitted by **David Galway**

in partial fulfillment of the requirements for the degree of

Master of Applied Science

J. Etele, Supervisor

G. Fusina, Co-Supervisor

M. I. Yaras, Department Chair

Carleton University

2009

Abstract

Desirable surveillance applications of unmanned aerial vehicles (UAV) and micro-aerial vehicles (MAV) in urban areas provides motivation for the investigation of turbulent wind generated by the airflow around buildings in such areas, since this turbulence can potentially cause instability in aircraft flight. Urban canyons and single buildings are considered as the basic units of the urban geometry, and it has been shown that the airflow around such structures is classifiable with significant degrees of circulation and shear. An initial 'first generation' methodology is proposed by which wind data in an urban environment is selected, accessed and applied towards the simulation of aircraft flight. It is assumed that the wind in the urban environment through which the aircraft flies can be represented as a collection of isolated airflows around a number of discrete single buildings and canyons, each easily amenable to computational fluid dynamics (CFD). As such, the wind data necessary for the simulation of aircraft flight is contained in a pre-existing wind simulation database (WSD), populated with CFD simulations of the airflow around various single buildings and canyons. A set of single buildings and canyons typical to the North American urban environment is selected to provide a set around which the airflow is to be solved using CFD. A Selection Algorithm is proposed which uses single building and canyon wake volumes to determine if the flow at a location in a given urban environment fits a member of the WSD. Flight simulation through an urban environment is achieved by using the Selection Algorithm in conjunction with a modified dynamic model of the Aerosonde UAV and an autopilot/waypoint following routine. At each time step, the Selection Algorithm uses the aircraft position in the urban environment to select the appropriate wind data in the form of a wind velocity field, which is then used by the modified dynamic model to calculate the aerodynamic forces and moments experienced by the aircraft due to urban wind. The flight of the Aerosonde UAV along three paths in an urban environment is simulated, and it is

found that path deviations due to urban wind are consitent with expectations and are on the order of half a wing span, kept relatively small by the effectiveness of the autopilot. However, potentially dangerous aircraft paths are identified and control surface deflections prescribed by the autopilot are found to be significantly affected by the presence of urban wind.

Acknowledgements

First and foremost I would like to thank my Supervisor Dr. Jason Etele of Carleton University and my Co-Supervisor Dr. Giovanni Fusina from the Ottawa research centre of Defence Research and Development Canada (DRDC). This thesis was made possible in part by their guidance and confidence in my work. In particular, I would like to mention the tireless efforts of Dr. Etele in monitoring numerous deadlines and reviewing my written reports. I am also very grateful for the financial support that DRDC has given and is continuing to give to me. In this respect Dr. Fusina has been particularly helpful and diligent in acting as a crucial link between myself and DRDC.

I would also like to thank my friends and family for their support and my colleagues for their willingness to lend me their technical expertise when needed.

Table of Contents

List of Figures

List of Tables

Nomenclature

UAV	Unmanned Aerial Vehicle
MAV	Micro Aerial Vehicle
CFD	Computational Fluid Dynamics
A/C	Aircraft
CoG	Aircraft's Centre of Gravity
RBL	Rural Boundary Layer
UBL	Urban Boundary Layer
u_o	Freestream streamwise wind velocity component, m/s
S	Street width, m
H	Building height, m
H_{min}	Minimum building Height, m
W	Building width, m
b	Building width, m
L	Building length, m
CC	Canyon Centroid
Re	Reynolds number
LES	Large Eddy Simulation
$RANS$	Reynolds-Averaged Navier-Stokes
$R_{\perp}$	Building length perpendicular to canyon axis, m
$R_{\|\|}$	Building length parallel to canyon axis, m
ΔH	Building height difference in a canyon, m
D	Characteristic building length, m
D_{avg}	Average characteristic building length of two buildings in a canyon, m

WSD	Wind Simulation Database
$SBWSD$	Single Building Wind Simulation Database
$CWSD$	Canyon Wind Simulation Database
N	North
E	East
Z	Altitude, m
$\vec{W}$	Background wind vector
V	Velocity, m/s
V_{W_∞}	Background wind speed, m/s
$\vec{V}_W$	Local wind velocity, m/s
$\vec{V}_{W,A/C,b}$	Wind velocity at aircraft centre of gravity in the aircraft body coordinate frame, m/s
θ_{BAD}	Building Alignment Deviation angle, degrees
θ_{WO}	Wind orientation angle, degrees
θ_B	Building orientation angle, degrees
θ_W	Wind incidence angle, degrees
$\theta_{W,CFD}$	Wind incidence angle from CFD simulation, degrees
NED	North-East-Down coordinate frame
ENU	East-North-Up coordinate system
x_{ENU}	x coordinate in the East-North-Up coordinate frame
y_{ENU}	y coordinate in the East-North-Up coordinate frame
z_{ENU}	z coordinate in the East-North-Up coordinate frame
x_E	East-aligned coordinate
u	x axis velocity, m/s
v	y axis velocity, m/s
w	z axis velocity, m/s
u_W	x component of local wind velocity, m/s
WCH	Wind-Centroid-Height coordinate frame
Δx_{WCH}	Change in x coordinate of Wind-Centroid-Height coordinate frame
Δy_{WCH}	Change in y coordinate of Wind-Centroid-Height coordinate frame

Δz_{WCH}	Change in z coordinate of Wind-Centroid-Height coordinate frame
$body$	Aircraft Body coordinate frame
$(x, y)_{A/C,ENU}$	Aircraft coordinates in the East-North-Up coordinate system
$(x, y)_{B_i,ENU}$	i'th building centroid coordinates in the East-North-Up coordinate system
$FGGCS$	First Generation Geometry Configuration Set
$SBCS$	Single Building Configuration Space
CCS	Canyon Configuration Space
ν_{W_∞}	Kinematic viscosity at background wind conditions, m^2/s
M	Mach number
DIF	Database Index File
$SBDIF$	Single Building Database Index File
$CDIF$	Canyon Database Index File
SCF	Simulation Characteristics File
P_{ref}	Reference pressure, 1atm
q_w	Heat flux at wall, J/m^2
T_w	Temperature at wall, K
T_{nw}	Near-wall temperature, K
h_c	Heat transfer coefficient, $J/K{\cdot}m^2$
X_C	Distance from the building centroid along the x axis in the CFD coordinate frame, m
Y_C	Distance from the building centroid along the y axis in the CFD coordinate frame, m
U_H	Inflow velocity at building height, m/s
$U_{in}(z)$	Inflow velocity profile
$G1$	Gradient Line 1
$f_L(y_{WC})$	Left wake boundary function
$f_R(y_{WC})$	Right wake boundary function
$h(y_{WC})$	Wake height function
$s1_L$	Slope at control point 1 for left wake boundary function
$s8$	Slope at control point 8

DCM	Direction Cosine Matrix
ϕ	Euler angle for roll, degrees
θ	Euler angle for pitch, degrees
ψ	Euler angle for yaw, degrees
p	Roll rate, rad/s
q	Pitch rate, rad/s
r	Yaw rate, rad/s
p_{eff}	Effective roll rate, rad/s
S_θ	Sine of angle θ
C_θ	Cosine of angle θ
Lat	Latitude, degrees
$Long$	Longitude, degrees
Alt	Altitude, m
L_{Eq}	Earth's equatorial length, km
L_M	Earth's meridian length, km
n_{wake}	Number of wakes which contain aircraft
n_B	Number of buildings in the urban environment
θ_{WA}	Wind Alignment angle, degrees
$R(\theta)$	Rotation matrix for rotating 3D vectors by generic angle θ
$\vec{p}_{A/C,ENU}$	Aircraft position in the East-North-Up coordinate frame
$\vec{p}_{RC,ENU}$	Rooftop centroid position in the East-North-Up coordinate frame
n	Yaw moment, N·m
C_n	Yaw moment coefficient
r	Yaw rate, rad/s
C_{n_r}	Derivative of yaw moment coefficient with respect to yaw rate r
C_L	Lift coefficient
$V_{A/C}$	Airspeed, m/s
ρ_{w_∞}	Air density at background wind conditions, kg/m^3
S_{ref}	Reference area of the aircraft, m^2
α	Angle of attack, degrees

δ_e	Elevator deflection, degrees
m	Pitching moment, N·m
Y	Sideforce, N
δ_a	Aileron deflection, degrees
l	Roll moment, N·m
β	Sideslip angle, degrees
l_t	Length of aircraft tail arm, m
b	Wing span, m
b'	85% of wing span, m
$P_{x\leftrightarrow y,-z}$	Permutation matrix for 3D vectors
S_g	Scaling Factor
$\vec{x1}_{relA/C,b}$	Relative location of point 1 on the aircraft with respect to the centre of gravity in the body frame
$\vec{p}_{onA/C,CFD}$	Location of a point on the aircraft in the CFD coordinate frame
$\vec{V}_{W,WCH}$	Wind velocity at a location in the Wind-Centroid coordinate frame
θ_{relH}	Relative heading angle, degrees
δ_c	Control surface deflection, degrees
$\Delta\delta_c$	Change in control surface deflection over one time step, degrees
PID	Proportional-Integral-Derivative
t_n	Time at time step n, s
Δt	Simulation time step, s
TA	Track Aligned coordinate frame
Δz	Altitude deviation, m
Δx	Track deviation, m
$\theta_{bank,A/C}$	Aircraft bank angle, degrees
K_p	Proportional gain constant
K_i	Integral gain constant
K_d	Derivative gain constant
WNV	Waypoint Navigation Vector
θ_N	Navigation heading angle, degrees

θ_H	Aircraft heading angle, degrees
$x_{WNV,t}$	x-coordinate of the Waypoint Navigation Vector in the track-aligned coordinate frame
GP_1	Gradient Point 1
WP_1	Waypoint 1
B_1	Building 1
subscripts	
A/C	aircraft
W	wind
W_∞	background wind conditions
i	Variable number
min	minimum
$\perp$	perpendicular
$\|\|$	parallel
avg	average
B	building
WO	wind orientation
NED	North-East-Down coordinate frame
ENU	East-North-Up coordinate frame
WCH	Wind-Centroid-Height coordinate frame
CFD	CFD simulation coordinate frame
ww	windward
lw	leeward
sim	simulation scale
$real$	real-world scale
C	centroid
in	inflow
$body$	aircraft body coordinate frame
b	aircraft body coordinate frame
N	North

E	East
D	Down
U	Up
o	origin
RC	Rooftop Centroid
WA	Wind Alignment
$x \leftrightarrow y, -z$	switch x and y coordinates, reverse sign of z coordinate
$relA/C, b$	Relative to the aircraft centre of gravity, in the body frame
n	time step n
t	Track Aligned coordinate frame

Chapter 1

Introduction

1.1 Motivation

There exists significant research interest with regards to the flight of unmanned aerial vehicles (UAV) and micro-aerial vehicles (MAV) in urban environments. Such research has been motivated by numerous potential civil and military applications [1]- [7] such as reconnaissance and surveillance (Hegazy *et al.* [1]), human risk-reduction in hazardous environments (Mullens *et al.* [2]), military operations (Mullens *et al.* [2] and Peot *et al.* [4]) and law enforcement (for example, surveillance and planning of operations) (Murphy and Cycon [3]).

Due to the lightness and relatively low speeds of such aircraft, acceptable flight performance is a major concern because of the turbulent wind which arises in and around urban environments due to due to the presence of buildings and smaller structures such as cars and trees. [10], [12] Especially problematic is stable MAV flight, where the aircraft velocity may be on the same order as the wind velocity. [9]

In order to ensure stability in flight through urban wind environments, it is essential to develop aircraft controls tailored to such environments. The ability to specify the wind environment the aircraft will experience and a method to simulate aircraft flight in such an environment would be of significant aid to the development process and are the primary motivations and goals behind the research contained in this work.

1.1.1 Literature Review

The General Urban Wind Environment

Overviews of the general characteristics of urban wind by Boris [10] and Britter and Hanna [12] reveal the primary factors of influence to be meteorological, aerodynamic, and heat related. On the city scale the dominant effect of the urban area on wind is the transition of the rural boundary layer (RBL) to the urban boundary layer (UBL), as shown in Figure 1.1. The urban boundary layer extends farther into the atmosphere and is much more turbulent.

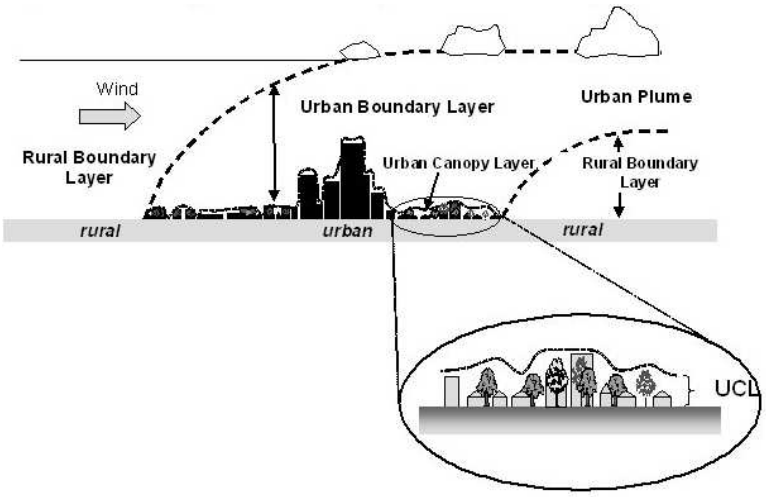

Figure 1.1: Comparison of rural and urban boundary layers [56]

The urban boundary layer is a subject of much research, [19]- [22] but the differences between the RBL and UBL, both meteorological phenomena, are primarily due to aerodynamics and urban heating. The greater thickness of the UBL is due to the presence of buildings which act as flow obstacles that force flow up and over the urban area and the heating effects of buildings which are at a different temperature than the passing air ('urban heat islands') and create vertical air motion through buoyancy effects [10], [12]. Building scale turbulence in the UBL is due primarily to aerodynamic factors. [12] As the RBL enters the urban area it drives air past the complicated urban geometry creating large wakes, dynamically shed vortices, complex recirculation zones and fountain flows up the backs of tall buildings. [10] These flows are complex, unsteady, and three-dimensional. Figure 1.2 is a CFD visualization of the turbulent flow in an urban area.

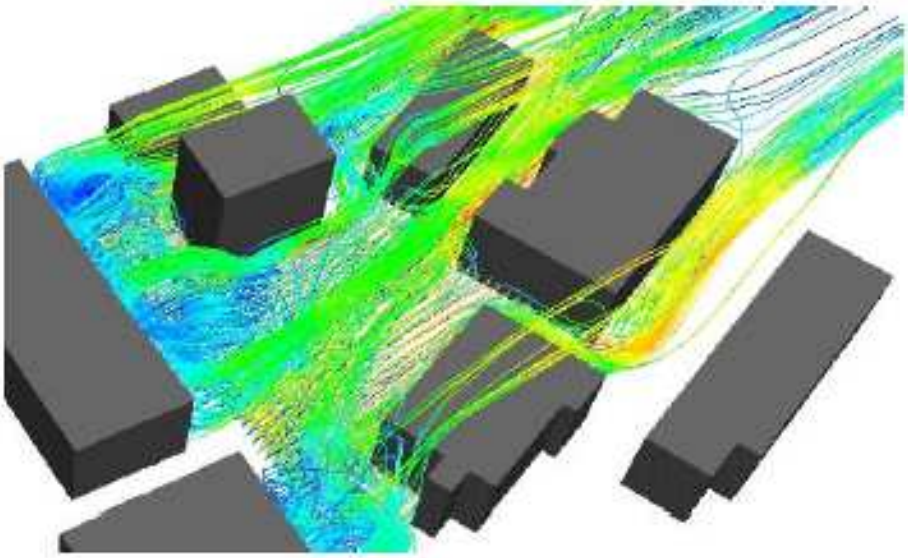

Figure 1.2: Turbulent flow around several buildings in close proximity [40], background wind speed is 4.6 m/s

Flow around Urban Structures

A review of existing literature reveals that the entirety of the flow around all the buildings in an urban environment does not allow for practical classification (i.e. reliable predictions of wind velocity structures at length scales comparable to a UAV) other than a rough turbulence intensity scale based on the wind speed and direction in the surrounding atmosphere and the average building density and height; however, plenty of literature exists on the subject of a finer classification of flow around smaller, individual building structures. [15], [23]- [38] In the urban environment the volume occupied by the buildings, known as the urban canopy, has as its basic geometric unit the urban canyon and its surrounding buildings [47]. Figure 1.3a is an illustration of a generic urban canyon, essentially two or more buildings from which a 'canyon' is formed in between. Figure 1.3b is a basic parameterization of a two-building canyon where S is the canyon street width and H, W, and L are the individual building heights, widths, and lengths.

Baskaran and Kashef [28], Lakehal and Rodi [32], and Meroney *et al.* [34] investigated flow around single rectangular prismatic buildings. These flows experience recirculation zones downstream of the leeward wall which, in spite of the simple geometry, display the complex features of real building flows. [32] Martinuzzi and Tropea [33] undertook flow visualization

(a) Generic urban canyon [49]

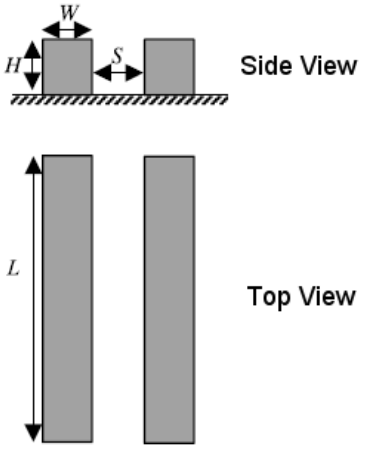

(b) Parameterization of two-building canyons studied by Kastner-Klein *et al.* [15]

Figure 1.3: Urban canyon and its basic parameterization

studies of flow around simple rectangular prismatic buildings at $Re = 40,000$ and found the mean flow pattern to be that as illustrated by Figure 1.4a. Of note is the flow separation on the building roof and sides, the arch vortex just downwind of the building, and the shear layer of smaller vortices caused by vortex shedding off the building sides. Figure 1.4b demonstrates the 'rooster tail' wake as named by Boris [10].

Flows around canyons of varying dimensions have been investigated, particularly to study the influence of geometry on vortex formation, by Kastner-Klein *et al.* [15], Hunter *et al.* [16], Baik and Kim [29], Kovar-Panskus *et al.* [31], and Oke [35]. In the simpler canyon configurations, the two buildings forming the canyon have flat roofs and similar height. The formation of canyon vortices for these configurations is dependent mainly on the aspect ratio S/H [15]. It has been established that on this basis three different flow regimes can be distinguished [35], all of which are described in Figure 1.5.

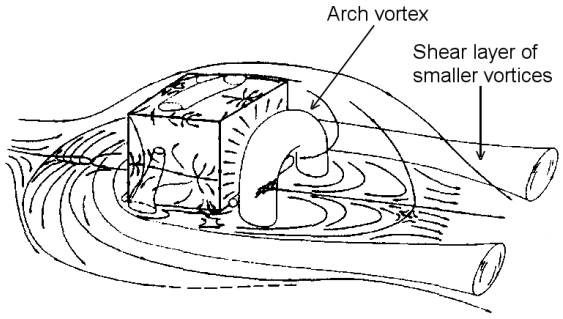

(a) Various flow structures around single building [33]

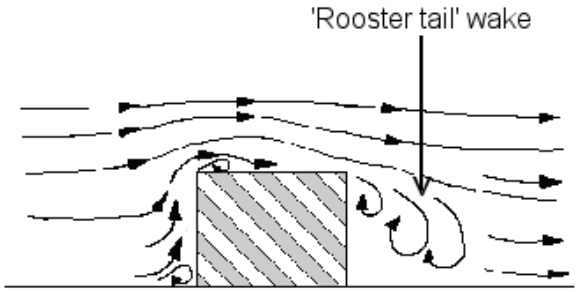

(b) Side view of flow around single building showing 'rooster-tail' wake [48]

Figure 1.4: Flow around single building

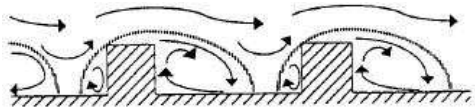

(a) $S/H \geq 3$ widely spaced, similar to flow around isolated buildings

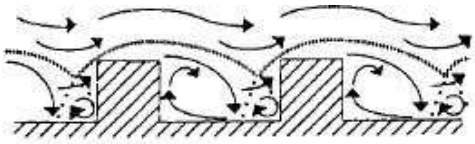

(b) $1.5 \leq S/H \leq 3$ wakes and front recirculation zones interact but do not overlap (wake-interference flow)

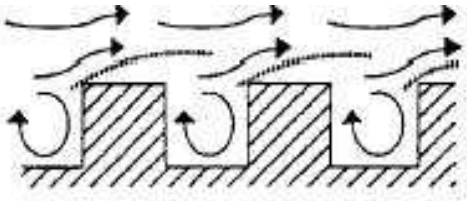

(c) $S/H \leq 1.5$ transition from wake-interference to skimming flow regime. Formation of a canyon vortex

Figure 1.5: Classification of canyon flow [29]

When the upwind building has a flat roof, it has been consistently observed that there exists flow separation at the upwind edge of the upwind building [15]. This establishes a shear zone above roof level with increased turbulence levels that are at a maximum just above the roof of the upwind building. The shear zone is a region with large velocity gradients and shear stresses, which are associated with elevated turbulence levels. As seen in Figure 1.6 the ratio of building length to canyon height L/H influences the extent of this shear zone and the magnitude of the increased turbulence levels. Since velocity fluctuations are associated with turbulence, the turbulence levels are quantitatively described by the normalized variance σ_u/u_o of the streamwise velocity component u where u_o is the freestream value of u. The location of the vortex centre inside the canyon also changes with L/H [15]. As the L/H ratio

decreases, the vortex centre is shifted closer to the downward wall (Figure 1.7) and the shear zone becomes less pronounced since a greater percentage of the flow leaks around the sides of the buildings. It has been observed for $L/H \leq 5$ that the lateral recirculation zones (Figure 1.8) converge in the canyon centre resulting in stronger vertical motions [15].

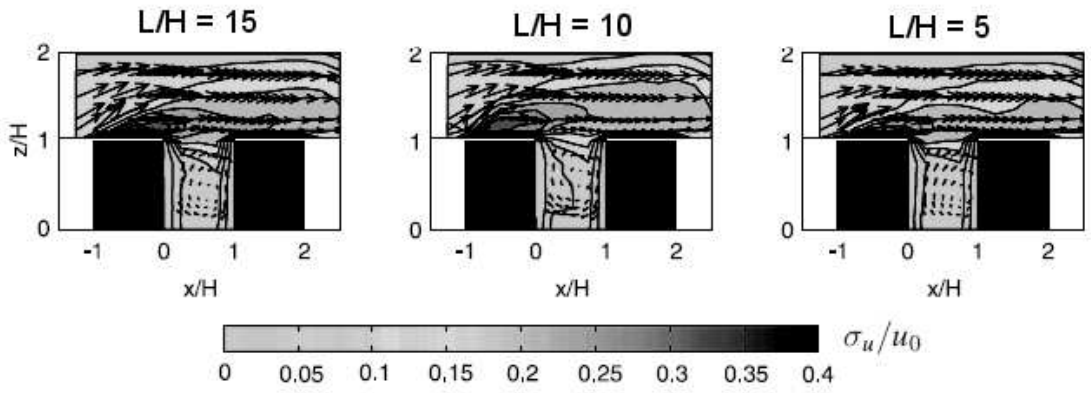

Figure 1.6: Illustration of how the shear zone above rooftop level changes with L/H [15]

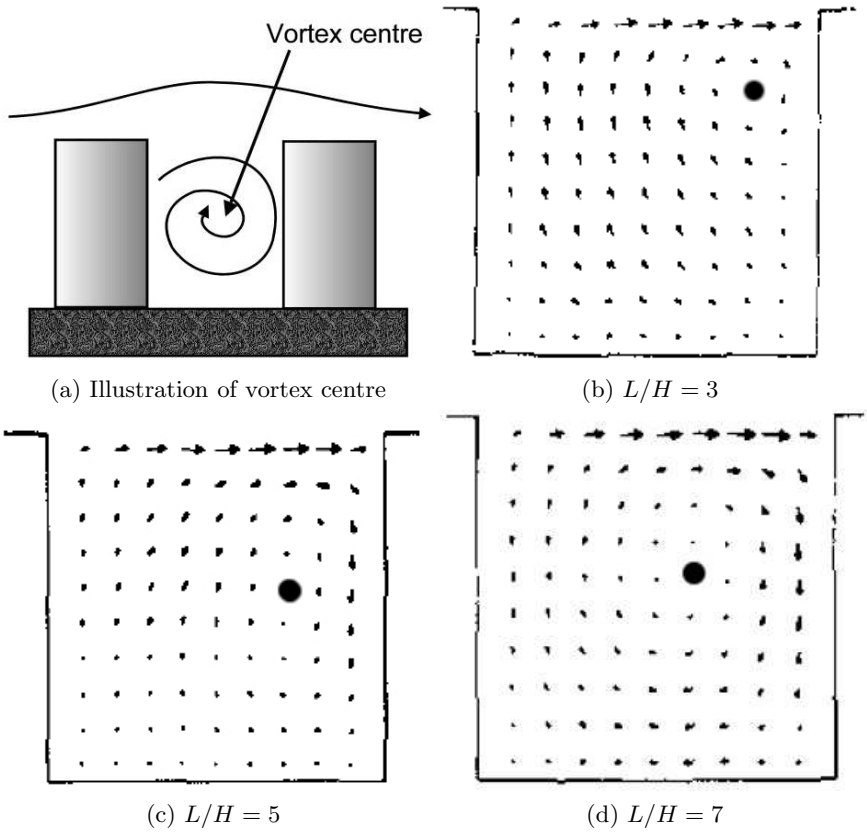

(a) Illustration of vortex centre (b) $L/H = 3$

(c) $L/H = 5$ (d) $L/H = 7$

Figure 1.7: Illustration of vortex centre and how the vortex centre changes with L/H. [16] The black dot indicates the approximate position of the vortex centre.

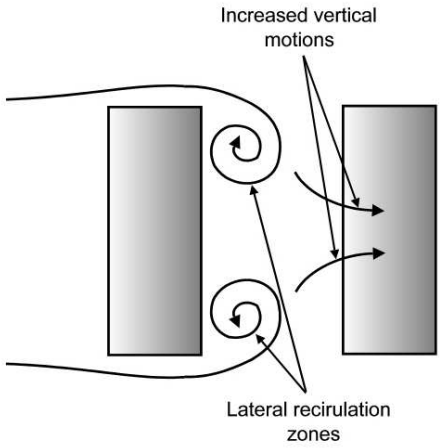

Figure 1.8: Top view of canyon showing lateral recirculation zones resulting in vertical air motion inside canyon

Roof geometry has a significant effect on canyon flow as well. Investigations [15] show a

recirculation zone spanning the canyon top with stagnant air inside the canyon (Figure 1.9), suggesting that roof geometry greatly affects in-canyon vortex formation. Additional frictional effects as a result of irregular roof geometry are another consideration. For a single canyon, any variability in roof heights of the flanking buildings can be classified as either a step-up or a step-down notch. In the former case (Figure 1.10a) a single vortex system is the observed tendency, and in the latter case (Figure 1.10b) a double vortex system with the primary vortex covering the upper part of the cavity and a secondary counter-rotating vortex forming at the corner of the windward building [15].

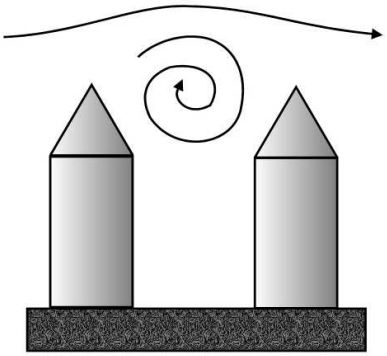

Figure 1.9: Vertical displacement of vortex due to peaked roofs

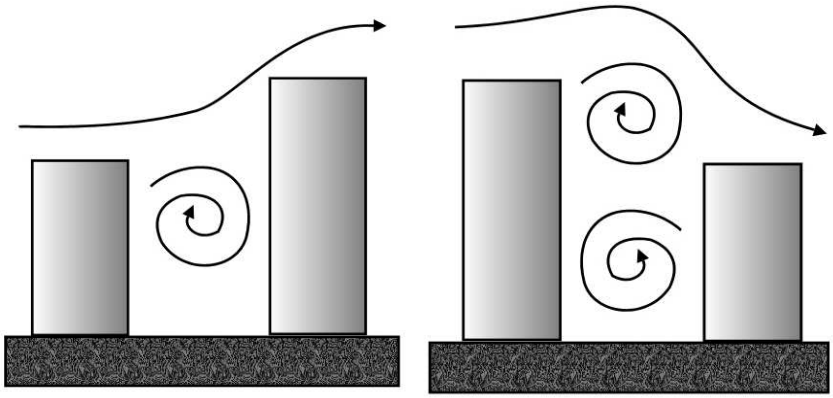

(a) Step-up notch (b) Step-down notch

Figure 1.10: Vortex formation in a step-up and step-down notch

Computational fluid dynamics (CFD) has been widely used for the purpose of obtaining data representing the airflow in an urban environment. Mainly motivated by pollutant dispersion research, CFD simulations of the flow in large urban areas and around complex

building structures have been performed. [10], [17], [23]- [27] Particularly, studies by Patnaik *et al.* [23], [24] acknowledge the costly, time consuming nature of simulating large urban areas. In urban areas the flows around individual buildings are fully separated and interact with one another resulting in highly complex unsteady, turbulent behaviour. Therefore, choice of turbulence model, grid sizing, and other numerical parameters is of great significance. In the studies by Patnaik *et al.* a Large Eddy Simulation (LES) approach is pursued where the domain size of these simulations is very large, on the order of kilometers, but the typical grid resolution is on the order of 5 to 10 metres. Keeping in mind the length scale of a typical UAV/MAV (largest is under 5 metres in length, smallest under a metre), this is a very coarse resolution. A significantly finer resolution required to capture flow features relevant to the flight of a typical UAV/MAV would result in an extremely large node count. Furthermore, if a real urban environment is desired there is the added task of modeling a large number and variety of building geometries, some of which may be a challenge to grid properly.

Many CFD simulations of flows around smaller, less complex building structures, such as single buildings and canyons, have been performed. [17], [28]- [32], [34], [36]- [38] It should be noted that the Reynolds numbers of the flows studied are quite varied but all are considered representative of wind conditions in actual urban environments. The flow physics of such flows are much better understood than flows in large urban areas and require significantly less computational resources. The standard $k-\epsilon$ model (models the turbulent fluctuations with the transport of turbulent kinetic energy k and turbulent dissipation ϵ) and modified $k-\epsilon$ models are used, but better performance is observed by the modified $k-\epsilon$ models such as the Kato-Launder $k-\epsilon$ model (Lakehal and Rodi [32] and Lien and Yee [37]), and two equation models which use the standard $k-\epsilon$ formulation in the low viscosity core of the flow and another one-equation model close to the wall where viscous effects dominate (Lakehal and Rodi [32]). Tests by Lakehal and Rodi [32] and Murakami *et al.* [17] have also shown that Large Eddy Simulation (LES) produces good results, however LES is relatively demanding on computational requirements. With regards to transient behaviour of the flow, studies by Baik and Kim [29] use a simulation time step of $\Delta t = 0.05$ s and find that the simulated physical time to achieve quasi-steady flow in a 2D canyon to be 10 to 30 minutes. Studies by Smith *et al.* [36] require a simulation time step of $\Delta t < 0.5$ s and find that the physical simulated time to

achieve quasi-steady flow around a 3D single cubical building to be about 1 hour. Simulation time steps researched from other literature fall in between $\Delta t = 0.05$ s and $\Delta t = 0.5$ s. Results from Baik and Kim are taken from one instance in time at the 1-hour mark; results from Smith *et al.* are averaged over the last 20 minutes of simulation. Three dimensional computational studies around an array of cubical buildings by Lien and Yee [37] and around a single cubical building by Smith *et al.* [36] and Zhang *et al.* [38] utilize computational domains varying in height from four building heights, 4 H, (Smith *et al.*, Zhang *et al.*) to 8 H (Lien and Yee). Domain widths used by Smith *et al.* and Zhang *et al.* are six building widths, 6 W, and 7 W, respectively. The study by Lien and Yee utilized an entrance length (length from the inlet to the windward face of the windward most building) of 5 W and an exit length (length from the leeward face of the leeward most building to the outlet) of 15 W. The finest grid resolution found was 0.001 W and the coarsest 0.08 W. In all cases the authors found the simulation results to be satisfactory, with the main improvements being required in other areas such as turbulence modeling.

UAV/MAV Flight in an Urban Environment

The simulation of UAV/MAV flight in an urban wind environment involves two main considerations. First, the aircraft needs to avoid the obstacles (buildings, possibly trees) in the environment. Secondly, urban wind data must be coupled with a dynamic model of the aircraft in order to account for urban wind effects. Automated collision avoidance is a topic beyond the scope of this paper, but for those interested references [39], [40], [4], [6], [7], and [41] provide information on this topic. The work done by Orr *et al.* [40] and Stoor *et al.* [41] is of interest since they also take urban winds into consideration. Orr *et al.* uses the Air Vehicles Unstructured Solver (AVUS) to simulate the flow in an urban area and interfaces it with a six-degree-of-freedom aerodynamic aircraft model of their design, allowing for the simulation of aircraft flight in an urban wind environment. At each instant of time the dynamic model takes into account the wind at the aircraft's centre of gravity (CoG), but does not account for the wind variation over the aircraft's physical dimensions, effectively treating the aircraft as a point mass. The aircraft used for the simulations is an MAV with a maximum mass of 0.4 kg and cruising speed of 30 m/s. Figure 1.11 shows the simulated wind field around all the

buildings in the urban environment obtained by Orr *et al.* and used in simulations of MAV flight. A constant background wind speed of 4.6 m/s is specified. Figures 1.12a and 1.12b show the results of two MAV flight simulations where a simple waypoint following routine is implemented in order to pass by all waypoints within one aircraft turn radius for a case ignoring wind (Figure 1.12a) and for one in which wind is accounted for (Figure 1.12b). With the wind taken into account, the aircraft path does not hit all waypoints and deviates significantly from the path flown in a windless environment. This implies that in terms of the ability to adequately control a small aircraft, there is a significant difference between the aircraft experiencing constant wind and turbulent wind generated by buildings. A specific aircraft control routine may work satisfactorily for constant wind, but as seen from these results, the same routine may fail when buildings are introduced.

The method used by Orr *et al.* to simulate aircraft flight is similar to the top-level scheme by Etkin [42], shown in Figure 1.13. For the application by Orr, the information in the 'Atmospheric Motion' block must be continually updated with the wind velocity vector at the aircraft's centre of gravity, obtained by interpolation from the CFD wind data (represented as a wind vector field) which in turn depends on the position of the aircraft in the urban wind environment.

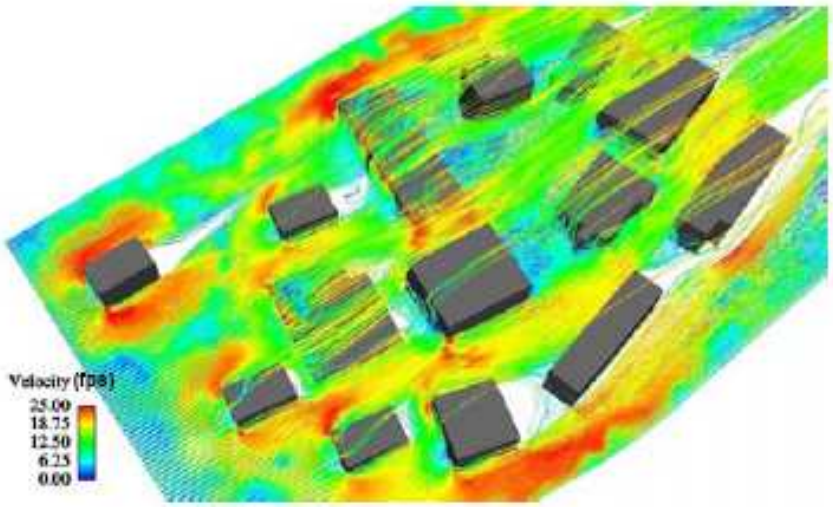

Figure 1.11: Wind data used by Orr *et al.* for flight simulation [40]

Orr's method does not calculate aerodynamic moments due to wind from the instantaneous

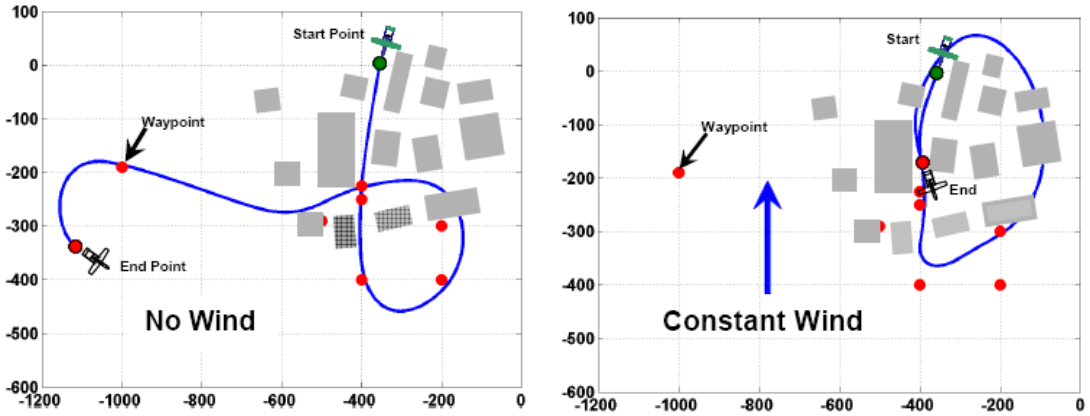

(a) Flight simulation results with wind ignored [40]

(b) Flight simulation results with a Northerly wind of 4.6m/s [40]

Figure 1.12: Results of flight simulation by Orr *et al.*. The MAV cruises at 30 m/s with a turn radius of approximately 30 m [40]

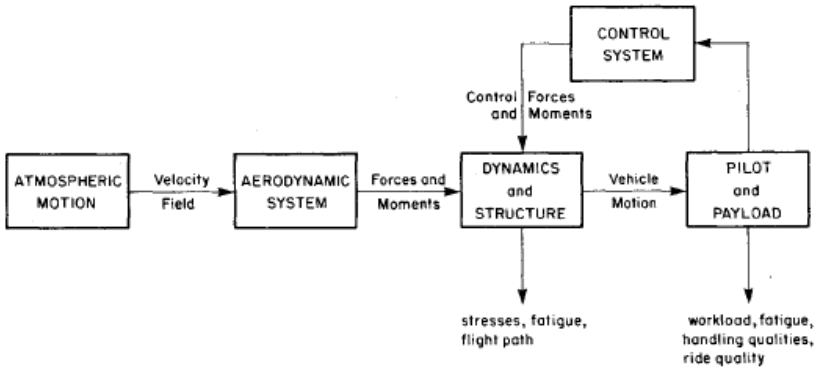

Figure 1.13: Overview of flight simulation in atmospheric wind [42]

wind variation over the aircraft's physical dimensions. These moments can be estimated from the instantaneous spacial variation of the wind field using panel methods or methods such as the 4-point method by Etkin [42] which assumes that the wind field varies linearly along the aircraft's longitudinal and lateral axes. The work presented in this thesis accounts for aerodynamic moments in this manner, treating the aircraft less like a point mass in that its physical size is accounted for with regard to the effects of wind.

1.2 Overview of Method

This thesis proposes a methodology by which aircraft performance can be predicted in a general urban environment. The methodology presented in this paper will first require the definition of the characteristics and parameterization of the first generation urban wind environment such as building locations, allowable building shapes and configurations, background wind, and coordinate frame. Required next is a configuration set of building configurations typical to the North American urban environment. CFD is used to simulate the airflow around these configurations and provide wind data to populate the wind simulation database (WSD). In the simulations performed for this thesis, heat transfer between the building interior and the surrounding wind field is not modeled; turbulence in the urban environment is modeled as being generated solely by the inertial effects of the air flowing around the buildings. The application of the WSD towards the simulation of aircraft flight in an urban wind environment requires a means of identifying which entries in the WSD match flow structures in the urban wind environment, identifying which entry from the WSD is to be applied given the aircraft's position, and a means of applying the wind data to the aircraft. Additionally, the development and implementation of a simple autopilot and waypoint following routine is required to provide a benchmark against which one can measure the significance of the effects urban wind has on aircraft flight.

A central feature of this methodology which differentiates itself from approaches similar to Orr [40] is that it does not require the flow throughout the entire urban area of interest to be simulated. Specification of the wind field local to the aircraft is accomplished using a database of previously completed CFD simulations. Since simulations of large urban areas are very time consuming, such a methodology has a significant advantage over methodologies which require complex CFD simulations applicable only to specific urban environments. The advantage of concentrating on individual building configurations within the greater urban geometry is that the characteristics of flows around simpler structures are better known; several examples of such studies have been given. This generational aspect allows the methodology to be continually improved and used with greater applicability. For example, if a first generation methodology contains only simulations of flows around single buildings and canyons, the database of simulations may only be of use when testing UAV flight in a low building-density

urban environment or at an altitude above the mean building height. Adding simulations with three or four buildings would allow for flight simulation in denser environments since in these environments more buildings tend to influence the flow at a given location.

Chapter 2

Definition of the Urban Environment

2.1 Urban Geometry

The general urban environment under consideration has as its basic geometric units the urban canyon and single building. Figures 2.1a and 2.1b illustrate the shape and parameterization of first generation single building and canyon geometries. All buildings are rectangular prismatic. Single buildings are parameterized by the building width W, length L, and height H. The characteristic length D of a building is defined as $D = \sqrt{L^2 + W^2}$. By convention, $W \leq L$ with a limit on L/W of $1 \leq L/W \leq 3$. The parameterization of canyons requires W, L, and H for each building in addition to building height difference ΔH and street width S. When dealing purely with geometry the sign of ΔH is always positive; it takes on positive/negative values when the canyon is placed in a wind field. A positive ΔH (by convention) corresponds to the situation where the windward building is taller than the leeward building and is called a step-down notch. The reverse situation where the windward building is shorter and ΔH is negative is called a step-up notch. Aside from the condition that $1 \leq L/W \leq 3$, the geometric restrictions on canyons illustrated in Figure 2.1b require both buildings to be 'aligned' with each other. This means that the canyon axis, defined as a line connecting both building centroids, is perpendicular with a side from each building. The length of the side perpendicular with the canyon axis is also labeled $R_\perp$ and the length of the side parallel to the canyon axis is labeled

$R_{||}$. In addition, the length of the building sides perpendicular to the canyon axis are to be equal. The reason for these requirements is that existing studies [15], [16], [29], [30], [31], [35] of canyon flow use similar geometries as Figure 2.1b. All simulations of canyon flow in the WSD use canyon geometries satisfying these restrictions.

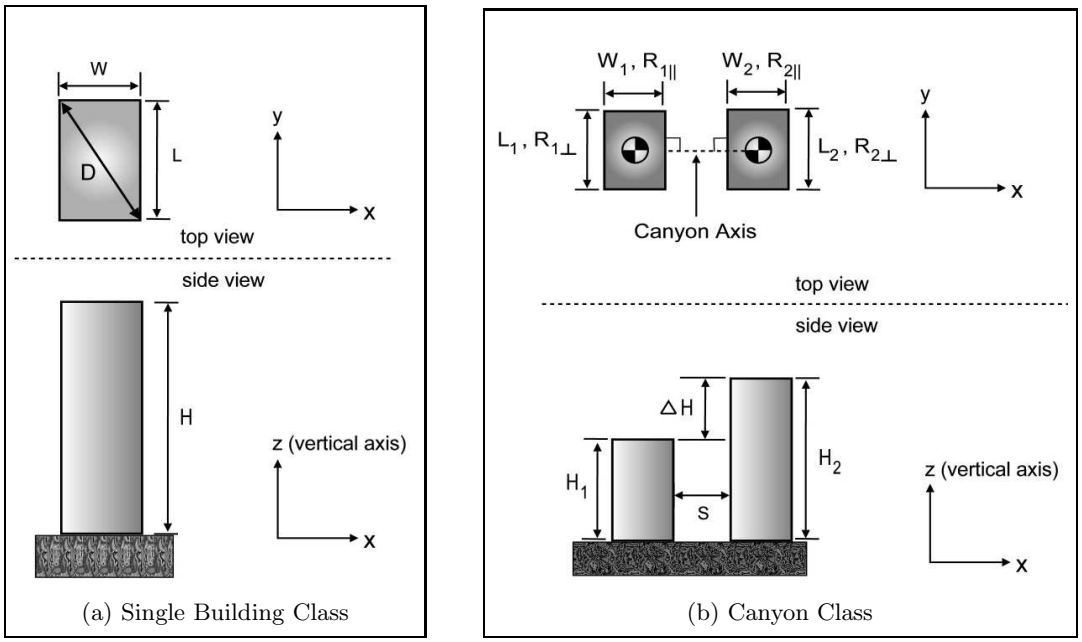

(a) Single Building Class

(b) Canyon Class

Figure 2.1: Isolated single building and canyon

Tolerances are defined so that building pairs with slight deviations from these restrictions still meet the geometric requirements for canyons. Figure 2.2 illustrates these tolerances, the allowable total deviation from alignment ($|\theta_{BAD,1}| + |\theta_{BAD,2}|$ within $\pm 5°$) and perpendicular edge tolerance ($R_{1\perp}/R_{2\perp} = 1 \pm 0.1$).

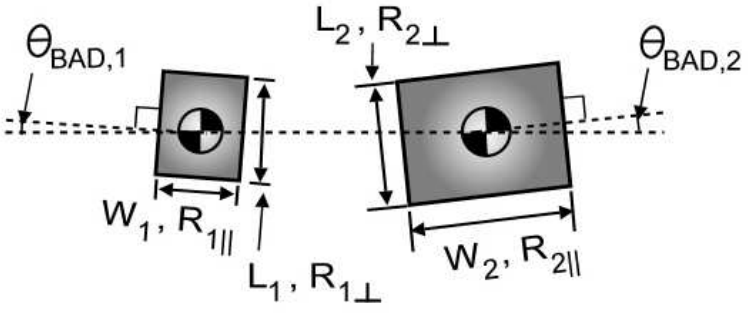

Figure 2.2: Deviations from aligned ($|\theta_{BAD,1}| = |\theta_{BAD,2}| = 0°$) condition and $R_{1\perp}/R_{2\perp}$ = 1 condition. The angle θ_{BAD} is the Building Alignment Deviation angle.

It should be noted that the canyon geometry in Figure 2.1b only represents *potential* canyons. A pair of single buildings in an urban wind environment is considered a canyon if there exists an entry in the wind simulation database (WSD) which represents the flow around the building pair, otherwise it is simply considered a set of two independent single buildings.

Photographs of the downtown areas of major North American cities such as Toronto, Vancouver, Chicago, and Houston (Figures 2.3, 2.4, 2.5 and 2.6, respectively) reveal that buildings in these diverse urban environments are largely rectangular prismatic. Figures 2.3-2.6 are also useful to place an upper limit on the L/W ratio (lower limit is $L/W \geq 1$ by definition), which is essential, since otherwise technically a infinite number of wind simulation database entries would be necessary. Values of $1 \leq L/W \leq 3$ are a reasonable approximation of the L/W range in typical North American urban environments. Figures 2.7 and 2.7 show a few examples of real urban canyons similar to the idealized canyons described by Figure 2.1b.

Figure 2.3: Downtown Toronto [50]

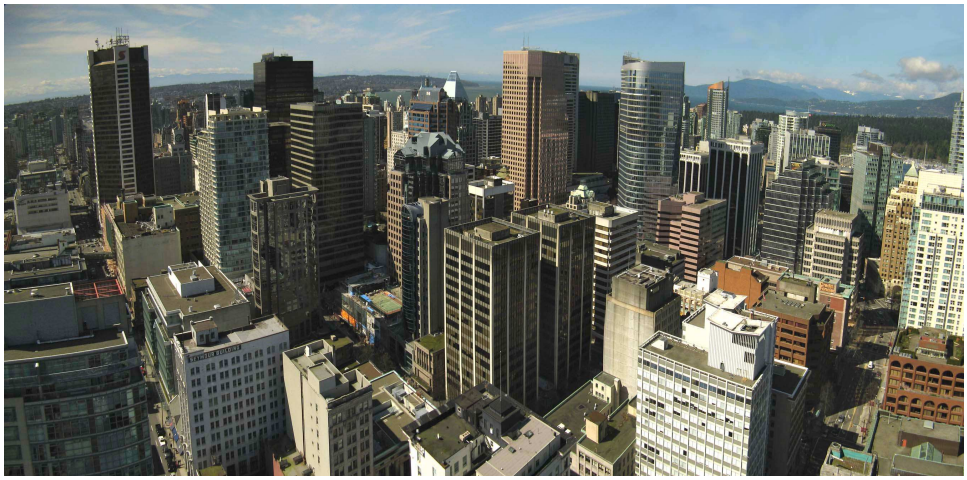

Figure 2.4: Downtown Vancouver [51]

Figure 2.5: Downtown Chicago [52]

Figure 2.6: Downtown Edmonton [54]

(a) Canyon in downtown Toronto [50]

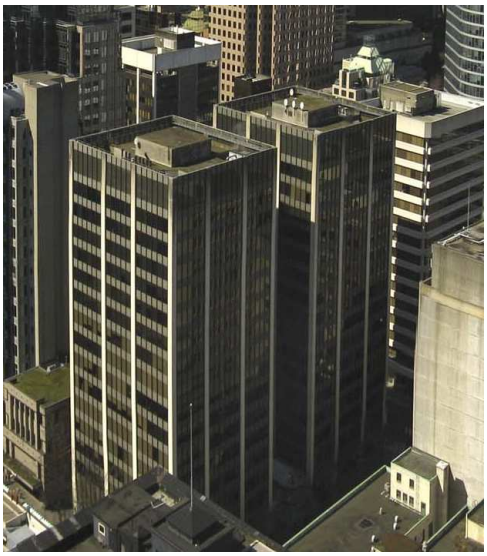

(b) Canyon in downtown Vancouver [51]

Figure 2.7: Examples of urban canyons satisfying geometry restrictions

(a) Canyon in downtown Chicago [52]

(b) Canyon in downtown Edmonton [54]

Figure 2.8: Examples of urban canyons satisfying geometry restrictions (cont'd)

2.2 Urban Background Wind

The volume of air unaffected by the presence of buildings is called the background wind. For the first generation methodology, at all points in time and space inside the background wind volume the wind direction and magnitude is assumed constant. The orientation of the background wind vector (wind vector orientation angle θ_{WO}) together with the orientation of a single building or canyon in the urban environment (building orientation angle θ_B) can be used to calculate the wind incidence angle θ_W, an important parameter when considering the flow around a building structure. As per the convention illustrated in Figure 2.9a, the wind vector orientation angle θ_{WO} is defined as the minimum positive (counter-clockwise) angle the background wind vector $\vec{w}$ makes with the urban environment reference direction where East is chosen as this reference direction. Also shown in this Figure is the building orientation angle θ_B for a single building, defined as the minimum positive (counter-clockwise) angle a line perpendicular to the long building side (single building orientation line) makes with the Eastern direction. Figure 2.9c shows the building orientation angle θ_B for a canyon, defined the same as for a single building except that the line which makes the orientation angle with the Eastern direction is the canyon axis.

The calculation of the wind incidence angle θ_W using θ_{WO} and θ_B must be done in different ways depending on whether θ_W is being calculated for a single building or canyon and on the outcome of the equation

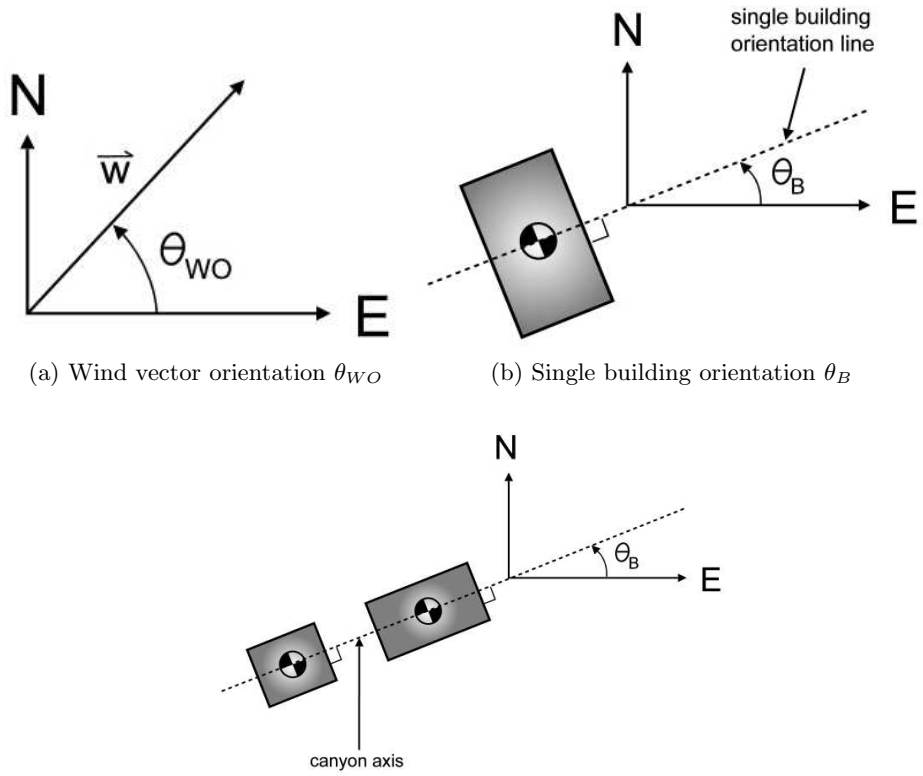

(a) Wind vector orientation θ_{WO}

(b) Single building orientation θ_B

(c) Canyon orientation θ_B

Figure 2.9: Determination of wind and building orientation angles θ_{WO} and θ_B

$$\theta_W = \theta_{WO} - \theta_B \tag{2.1}$$

Equation 2.1 allows θ_W to be in the range $-180° < \theta_W < 360°$. Conditional modifications to the value of θ_W as calculated by Equation 2.1 are necessary to satisfy the convention $\theta_W \geq 0°$ and to reflect certain symmetries with respect to the relative orientation between the single building or canyon and the background wind vector (Figure 2.10). First, if θ_W is negative then the angle is given an equivalent value through the operation $\theta_W \rightarrow \theta_W + 360°$, ensuring that $\theta_W \geq 0°$. The next conditional modification depends on whether θ_W is being calculated for a single building or canyon. For a single building, if $\theta_W > 180°$ then the modification $\theta_W \rightarrow \theta_W mod 180°$ is performed, reflecting the fact that for a single building wind incidence angles 180° apart describe the same wind incidence. (Figure 2.10a). For a canyon, if $R_{||1} = R_{||2}$ then the same modification is performed. These conditional modifications ensure that $0 \leq \theta_W < 180°$ for all single buildings and $0 \leq \theta_W < 360°$ for all canyons. As illustrated by

Figure 2.11a, the single building wind incidence angle ultimately depends only on the relative orientation between the single building orientation line and the background wind vector. The canyon wind incidence angle, as illustrated in Figure 2.11b, depends on the relative orientation between the canyon axis and the background wind vector as well as their orientation with respect to the East-North axes (unless $R_{||1} = R_{||2}$ in which case the calculation of θ_W is the same as for a single building).

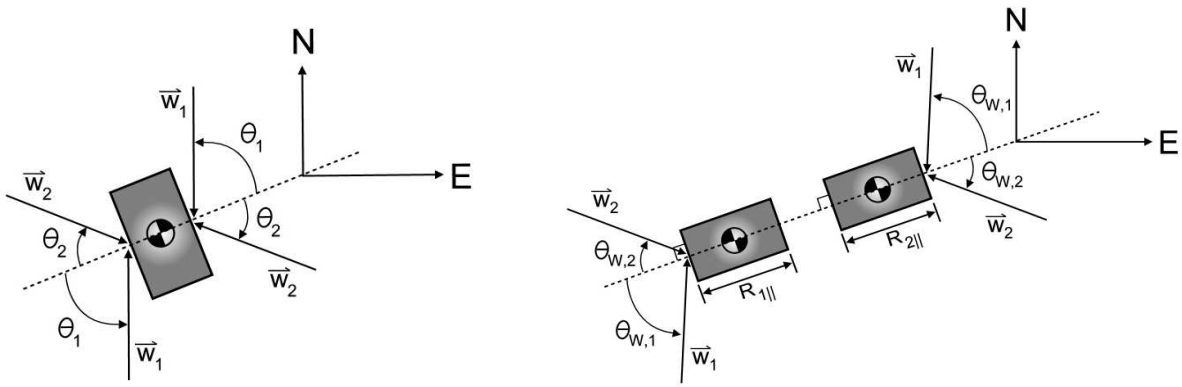

(a) Wind incidence symmetry for a single building

(b) Wind incidence symmetry for a canyon (only when $R_{||1} = R_{||2}$)

Figure 2.10: Wind incidence symmetry for a single building and canyon with $R_{||1} = R_{||2}$. The background wind vectors with matching labels are 180° apart and result in the same wind incidence (i.e. the angles with matching labels are the same magnitude when measured in the same direction from the single building orientation line or canyon axis.)

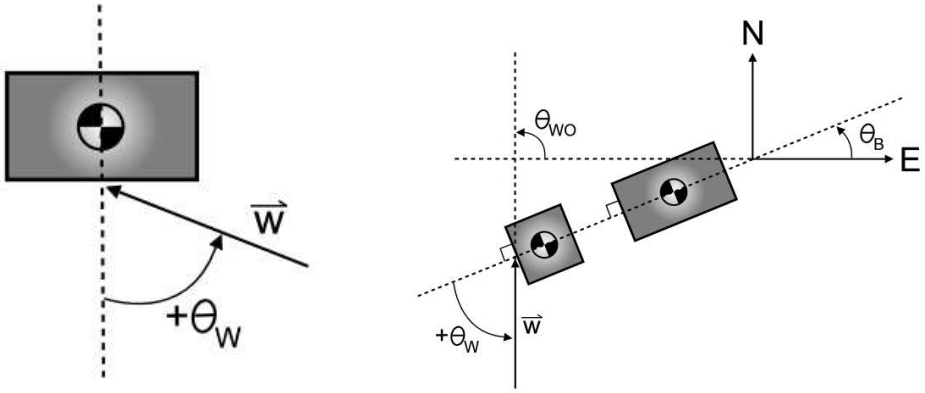

(a) Wind incidence angle θ_W for single building.

(b) Wind incidence angle θ_W for canyon

Figure 2.11: Illustration of wind incidence angle θ_W for single building and canyon

2.3 First Generation Urban Environment

Table 2.1 summarizes a complete description of a generic first generation urban wind environment (i.e. the type of urban wind environment used for this thesis) and the aircraft's position in this environment. Specification of the location of every building centroid $(x, y)_{B,i}$, the background wind vector $\vec{w}$, the height H_i, width W_i, length L_i, and orientation $\theta_{B,i}$ of all buildings together with the aircraft position $(x, y)_{A/C}$ is all the information required for selecting an entry from the WSD to represent the urban wind local to the aircraft. The locations of single buildings as well as aircraft location are defined in an absolute reference frame as shown in Figure 2.12. This reference frame uses East-North-Up (ENU) Cartesian axes, as it is assumed that the distance scale over which an aircraft mission will generally take place is small enough to use a flat-Earth model (negligible divergence/convergence of longitudinal lines).

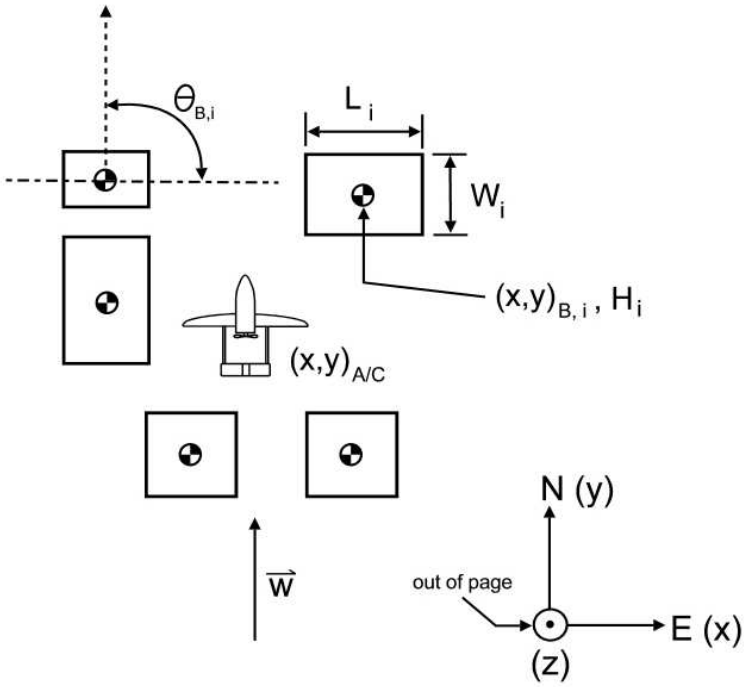

Figure 2.12: Top view illustration of urban environmental data

Table 2.1: Summary of Urban Environmental Data Parameters

Parameter Symbol	**Meaning**
$(x, y)_{A/C}$	Aircraft CoG position coordinates, m
$(x, y)_{B,i}$	Coordinate i'th building centroid, m
$\vec{w}(x, y)$	Background wind vector, m/s
H_i	Height of i'th building, m
W_i	Width of i'th building, m
L_i	Length of i'th building, m
$\theta_{B,i}$	Orientation of i'th building, degrees

Chapter 3

Simulation of the Urban Wind Environment

In this first generation methodology, urban wind data necessary for flight simulation is provided by the wind simulation database (WSD) where each entry in the WSD is a wind velocity field obtained from a CFD simulation of the air flow around a particular single building or canyon configuration. The CFD work is performed using the commercial software package Ansys CFX, developed by Ansys Inc. Aside from providing a CFD solver, its other capabilities include geometry modeling (creation of flow domain), unstructured mesh generation, and post-processing.

The wind data is required for two purposes. First, for each CFD simulation the wind velocity field is used to determine the volume of air significantly affected by the presence of the single building or canyon. These volumes, or wakes, are used during flight simulation to select appropriate entries in the WSD at each time step. Second, the wind data is the information which allows for the determination of the aerodynamic forces and moments on the aircraft for which the wind is responsible. How these forces and moments are calculated will be discussed in Chapter 4.

3.1 Geometry of First Generation Configuration Set

The first generation configuration set (FGCS) is the first group of single building and canyon geometry configurations around which the flow of air is calculated within a CFD simulation. The FGCS can be divided into two classes: single building class and canyon class.

The single building class geometry is parametrized by the ratio of width W to length L. Building height is not included as a parameter since, ignoring ground effects, the wind velocity at a point in proximity to the building is considered to only depend spatially on the horizontal distances measured from the building centroid and the vertical distance measured from roof level as illustrated by Figure 3.1 (i.e. the wind velocity at a point depends on how far the point is from the roof, not the ground). A large H/W ratio reduces the influence of ground effects near rooftop level, so a $H/W \geq 5$ is required for all single buildings since many tall buildings in downtown areas have a H/W of at least this much (see Figures 2.3-2.6).

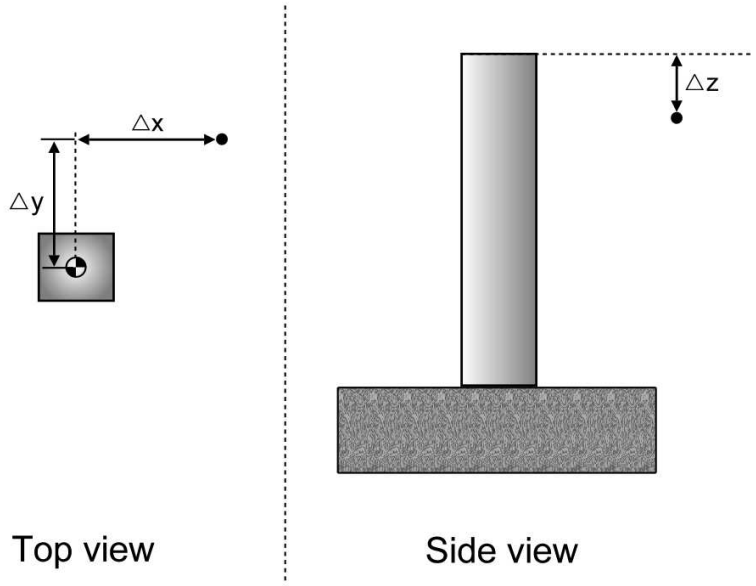

Figure 3.1: Spacial dependence of the wind field surrounding a building. A point is located in space by the two horizontal parameters Δx and Δy and the vertical paramter Δz (measured relative to roof level)

Members of the single building configuration set are defined by L/W values of 1, 1.5, 2, 2.5, or 3. Most building geometries fall within the L/W range 1-2.5 while the last two values of 2.5 and 3 define a range which is quite rare. Examples of buildings in the L/W ranges of

1-2.5 and 2.5-3 are shown in Figure 3.2.

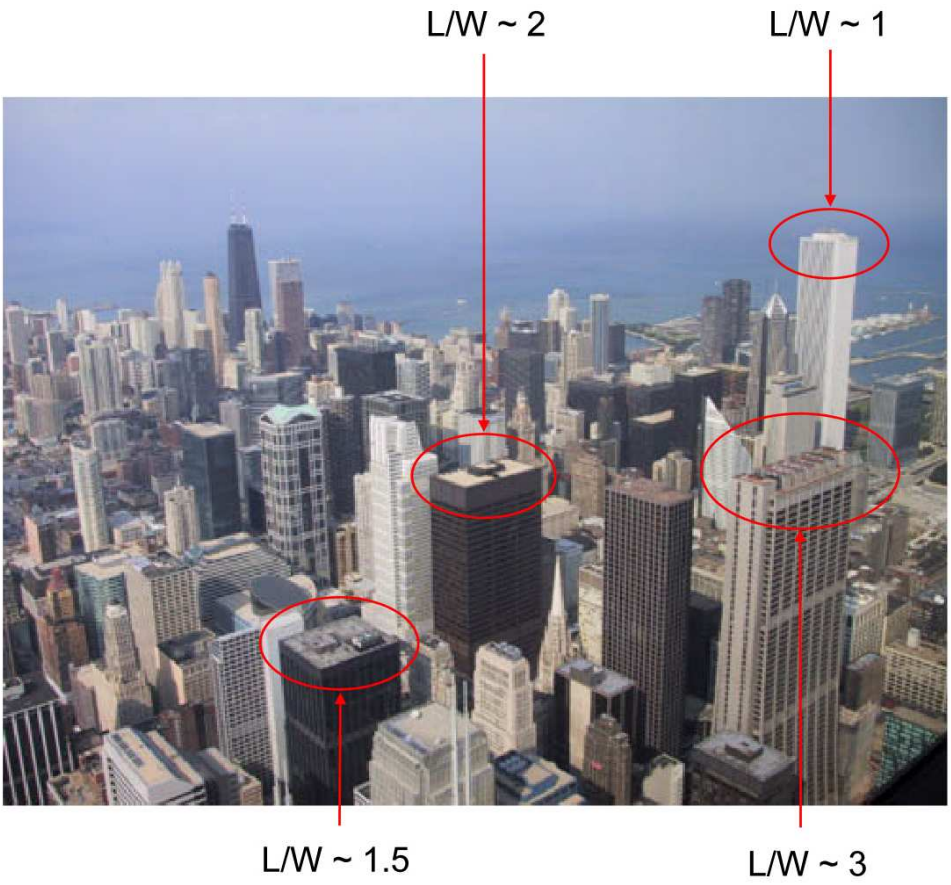

Figure 3.2: Examples of single building L/W ratios [52]

As illustrated previously in Figure 1.5 in Section 1.1.1, the ratio S/H is very important for canyon flow classification. Canyon members of this first generation configuration set will have S/H values of either 2.25 or 1.25 to capture wake-interference and skimming flow respectively. The L/W ratios of the buildings in the canyons can take the values 1, 1.5, or 2, as most buildings in real urban environments fall into the range $1 \leq L/W \leq 2$. The ratio $\Delta H/D_{avg}$ is allowed to take values of 0, 0.5, or 1, where D_{avg} is the average of the characteristic building lengths of both buildings D defined as $D = \sqrt{L^2 + W^2}$. The upper limit on $\Delta H/D_{avg}$ comes from the fact that the studies on urban canyon flows do not investigate canyons with large $\Delta H/D_{avg}$ values, most likely due to the fact that real urban canyons (Figures 2.7a-2.8b) generally do not have a $\Delta H/D_{avg}$ much greater than 1. In addition, the wind near rooftop level of the tallest building in a canyon with a high $\Delta H/D_{avg}$ is outside the influence of the shorter building and

therefore a single building CFD simulation is sufficient for the wind field representation at this location as illustrated in Figure 3.3. If ΔH is non-zero then H (important for the S/H ratio) is taken as the average height of the two buildings in the canyon. It should be noted that, unlike single buildings, the absolute canyon height is important since, for example, changing H without changing S changes the S/H ratio. However it will be seen later that through dynamic matching, a canyon CFD simulation with a given H can represent real canyon flows with a variety of H values as long as (among other things) all the dimensions of the real canyon are scaled equally from the canyon in the CFD simulation. As is the case for single buildings, the condition $H_{min}/W \geq 5$ is imposed where H_{min} is the minimum value of H_1 and H_2. Table 3.1 summarizes the geometric parameter values of the FGCS.

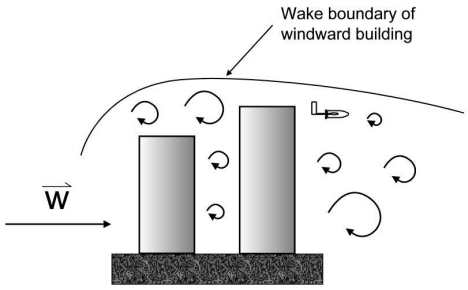

(a) Aircraft inside the wake of the shorter building

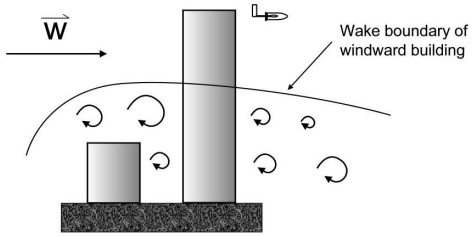

(b) Aircraft outside the wake of the shorter building. In this case, wind data representing the flow around just the taller building is sufficient

Figure 3.3: Illustration of how flight near rooftop height gives priority to canyons with low $\Delta H/D_{avg}$ values

Table 3.1: First Generation Configuration Set

Single Building Class	**Canyon Class**
$L/W = 1$, 1.5, 2, 2.5, or 3. $H/W \geq 5$.	$S/H = 2.25$ (Wake interference flow) or $S/H = 1.25$ (Skimming flow). Both buildings any combination of $L/W = 1$, 1.5, or 2. $\Delta H/D_{avg} = 0$, 0.5, or 1. $H_{min}/W \geq 5$.

3.2 Simulation Configuration Space

Each entry in the Single Building Wind Simulation Database (SBWSD) or the Canyon Wind Simulation Database (CWSD) corresponds to a unique ordered set of 3 or 7 indices, respectively. Each index is an important geometric or dynamic parameter of the CFD simulation (a few of which are listed in Table 3.1). Interpreting each index as a coordinate, the 3 indices cataloging the SBWSD form a 3-dimensional Single Building Configuration space (SBCS). Likewise, the 7 indices cataloging the CWSD form a 7-dimensional Canyon Configuration Space (CCS). Given a sample first generation urban environment (for example see Figure 2.12, Section 2.3) the flow around a particular single building or canyon in the environment, assumed isolated from the surrounding buildings, can also be mapped to a point in the SBCS or the CCS. This means that the real urban flow is geometrically similar (same geometrical ratios, such as S/H) and dynamically similar (same Reynolds number) to a CFD simulation corresponding to that point, and is therefore represented by that CFD simulation. However, there is little chance that CFD simulations of isolated single building or canyon flows defined independently of any particular urban environment would make exact matches with the actual environment within which the aircraft is flying. This makes it necessary to define tolerances around points in SBCS and CCS corresponding with entries in the WSD. Therefore if the flow around an isolated single building or canyon in a first generation urban environment is mapped to a point in the SBCS or CCS within a set tolerance of a point corresponding to a CFD simulation then the isolated single building or canyon flow is considered to be represented by that CFD simulation.

3.2.1 Single Building Configuration Space (SBCS)

The single building simulations undertaken can be classified using three free parameters. The first parameter is the L/W ratio of the building, parameterizing building geometry. The second parameter is the background wind incidence angle θ_W (as illustrated previously in Figure 2.11a from Section 2.2). The third parameter is the freestream Reynolds number defined as $Re = \frac{V_{W_\infty} D}{\nu}$ where V_{W_∞} is the background wind velocity, ν is the kinematic viscosity of the fluid at background wind conditions, and D is the characteristic length defined as $D = \sqrt{L^2 + W^2}$. The Reynolds number can be thought of as representing wind speed and is important for ensuring dynamic similarity between simulation results and real world flows.

No other parameters are considered for matching dynamic similarity since urban winds are bounded flows and can be considered incompressible (M < 0.2). Therefore, any single building simulation is uniquely defined as a point in a three dimensional single building configuration space (SBCS) as illustrated by Figure 3.4.

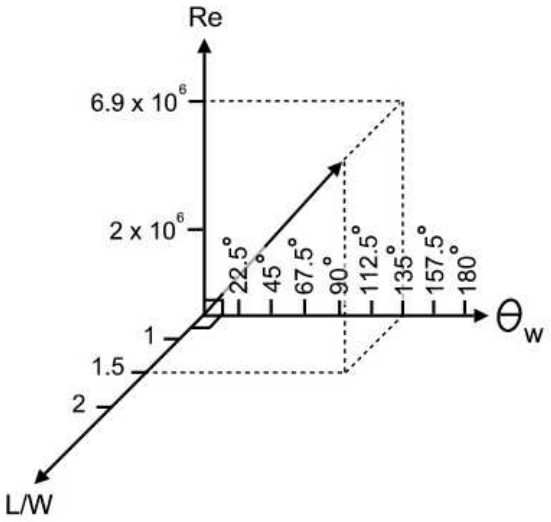

Figure 3.4: Single Building Configuration Space

The tolerances on each axis (used for matching real urban environments to configurations with existing CFD simulations) $\pm 11.25°$ for θ_W, ± 0.25 for L/W, and 5% of Re. For example, if a single building CFD simulation exists for $\theta_W = 45°$, $Re = 2 \times 10^6$, and $L/W = 1$ then a single building within a real urban environment with $\theta_W = 49°$, $Re = 1.92 \times 10^6$, and $L/W = 1.25$ would be considered a match with the CFD simulation and the wind data for that simulation would be used.

As illustrated by Figure 3.5, a single building geometry with $L/W = 1$ is symmetric about the background wind vector $\vec{w}$ for $\theta_W = 0°$ and $90°$. As a minimum, an incidence angle in the middle of the asymmetric region $0° < \theta_W < 90°$ (i.e. $\theta_W = 22.5°$) should be included in the WSD, necessitating a $\pm 11.25°$ tolerance. Adding a building width to L for a single building with $L/W = 1$ gives $L/W = 2$, but it is not desired that a real single building flow with $L/W = 1.49$ be represented by a $L/W = 1$ simulation. Therefore the minumum interval for L/W is 0.5 resulting in a tolerance of ± 0.25. A 5% change in Re with constant fluid properties and building geometry corresponds to a 5% change in background wind velocity. This was

chosen to match the criteria used to define a building wake (as discussed later in this section), defined as the volume of air surrounding a building which has experienced at least a 5% change in the streamwise component with respect to background conditions.

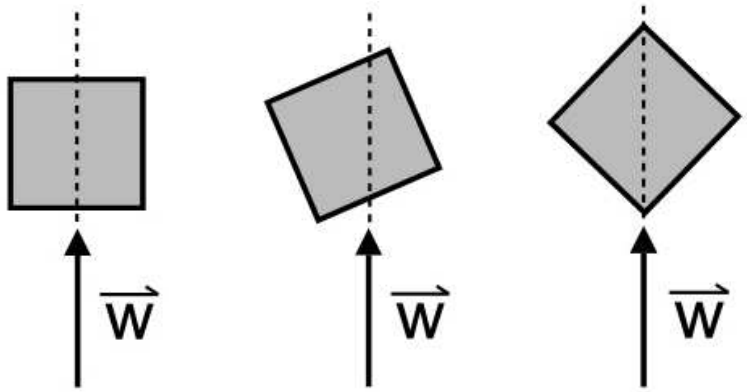

(a) $\theta_W = 0°$ (b) $\theta_W = 22.5°$ (c) $\theta_W = 45°$

Figure 3.5: Illustration of 22.5° wind incidence interval

3.2.2 Canyon Configuration Space (CCS)

Simulations of canyons from the configuration set are parameterized by 7 parameters. Referencing Figures 2.1b and 2.11b, they are the ratios of the building edge length perpendicular ($R_\perp$) and parallel ($R_{||}$) to the canyon axis for both the windward and leeward buildings ($(R_\perp/R_{||})_{ww}$ and $(R_\perp/R_{||})_{lw}$, considered as two parameters), the wind incidence angle θ_W, the freestream Reynolds number Re, the ratio of building separation to building height S/H, the ratio of building height difference to average characteristic length $\Delta H/D_{avg}$, and the ratio of average building height to average characteristic length H_{avg}/D_{avg}. It should be noted that while the windward building is defined as the building in the canyon with the upstream centroid, when the wind incidence angle $\theta_W = 90°$ or $270°$ (i.e. there isn't a clear upstream building centroid) by necessary convention the windward building is the building with the smaller edge length parallel to the canyon axis ($R_{||}$). The tolerances on $(R_\perp/R_{||})_{ww}$, $(R_\perp/R_{||})_{lw}$, θ_W, and Re are the same as for the single building parameters while the tolerances on S/H, $\Delta H/D_{avg}$, and H_{avg}/D_{avg} are $\pm$ 0.25.

3.3 Storage of the WSD

Four file types are used to store all the necessary information about the WSD and are summarized in Table 3.2. The first is the Database Index File (DIF), with a separate DIF existing for the single building class of simulations and the canyon class of simulations. For a given simulation class, the DIF corresponding to that class (for example, the single building DIF) lists all the points in the configuration space corresponding to completed CFD simulations (entries in the WSD) of that class in the order they were completed. Each entry in the WSD is indexed by their class (single building or canyon) and their position in the sequence given in the corresponding DIF (single building or canyon DIF). For example, to find the DIF position of the CFD simulation in the WSD which corresponds to a flow around a single building in an actual urban environment as described by the SBCS indices $\theta_W = 0°$, $Re = 2 \times 10^6$, and $L/W = 1.5$, these indices are compared with all the indices in the single building DIF. Using Figure 3.6 as a sample segment of a single building DIF, these indices correspond to the second entry indicating that the wind data entry appropriate for this flow is the entry indexed by single building DIF position 2.

Table 3.2: File Types Used to Store WSD

File Type	**Description**
Database Index File (DIF)	Lists all entries from the WSD by their corresponding points in single building or canyon configuration space. A separate DIF exists for single buildings and canyons.
Simulation Characteristics File (SCF)	Lists important characteristics of a given CFD simulation from the WSD. A separate SCF exists for each entry in the WSD.
Results File	Contains simulation data for a given CFD simulation as returned by the CFD solver.
Wake Shape File (WSF)	Contains geometric information about the volume of air significantly affected by the presence of a single building or canyon in a given CFD simulation.

The Simulation Characteristics File (SCF) is a file which lists important characteristics of a given CFD simulation. A separate file for each simulation exists, and contains the location of

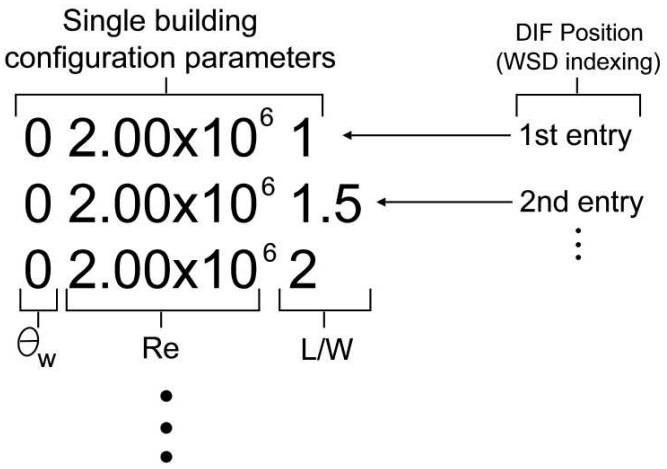

Figure 3.6: Single building Database Index File

the single building or canyon centroid in the CFD coordinate frame, the working fluid used for the simulations, the characteristic length D and the single building or canyon height. These characteristics are important for calculating the forces and moments the aircraft experiences due to urban wind during flight simulation. The name of a SCF corresponding to a single building simulation always starts with the prefix 'sb' and ends with the corresponding position of the CFD simulation in the single building DIF. For example, a single building simulation with single building DIF position 2 has the SCF name `sb2.txt` (or an equivalent extension). Similarly, the name of a canyon SCF starts with the prefix 'canyon' and ends with the CFD simulation's canyon DIF position. For example, a canyon simulation listed first in the DIF has the SCF name `canyon1.txt`.

The actual CFD simulation results file containing the data produced by the CFD solver is the third file type. It is named the CFD simulation's SCF file name as the prefix plus the suffix 'results'. For example, a single building simulation with the corresponding SCF file `sb2.txt` has the results file name `sb2results.res`.

The fourth and final file type is the wake shape file (WSF) which describes the geometry of the volume of air significantly influenced by the single building or canyon for a given CFD simulation. The WSF name for a given single building or canyon flow uses the corresponding SCF file name with the suffix 'wakeshape'. For example, the WSF name corresponding to a canyon flow with a canyon DIF position of 1 (SCF name `canyon1.txt`) is `canyon1wakeshape.txt`.

The contents and format of the WSF is more appropriately discussed in greater detail later in section 3.4.3.

3.4 Single Building Simulations

Table 3.3 describes the single building cases investigated using CFD (i.e. how much of the SBCS has been populated with completed CFD simulations). The geometric parameters and wind speeds used for these simulations are intended to be independent of specific geometric scales (i.e. small towers vs. skyscrapers). As such, small scale base dimensions on the order of one metre are used and the wind speed can be varied to ensure dynamic similarity with real world configurations of interest. For example, equating $Re_{sim} = V_{sim}D_{sim}/\nu_{sim}$ to $Re_{real} = V_{real}D_{real}/\nu_{real}$ and noting that the CFD simulations use air as the working fluid, the kinematic viscosity cancels out and the following relation is obtained:

$$D_{real} = \left(\frac{V_{simulation}}{V_{real}}\right) D_{simulation} \tag{3.1}$$

This shows that depending on the value of V_{real}, each CFD simulation can be made dynamically similar to an urban flow around a real building with size D_{real}. For the simulation values listed in Table 3.3, if a V_{real} of 14 km/h (average wind speed over Vancouver for the 2007 year [57]) is used then the simulations are dynamically similar to flows around buildings with the characteristic length D_{real} (listed in the final column of Table 3.3).

Table 3.3: Single Building Cases Currently Populating the Single Building WSD

Case #	θ_W	**Wind Speed (m/s)**	L/W **value**	**Corresponding** D_{real} **value (m)**
1a	0°	8.46	1	7.7
1b	0°	20	1	18.18
2a	22.5°	8.46	1	7.7
2b	22.5°	20	1	18.18
3	45°	8.46	1	7.7

3.4.1 Simulation Setup and Grid Independence Study

Figures 3.7a - 3.8 illustrate the coordinate system and geometry of the flow domain used for all single building CFD simulations. The coordinate system used for all CFD simulations is the CFD system (Figures 3.7a and 3.7b) with axes x_{CFD}, y_{CFD}, z_{CFD}, where z_{CFD} is the vertical axis positive upwards, y_{CFD} is a horizontal axis aligned with the background wind vector $\vec{w}$ and positive in the direction of the flow, and x_{CFD} is a horizontal axis formed by maintaining the right-handed coordinate system rule. The shape of the domain is rectangular prismatic, with the length and y_{CFD} axis aligned with the wind vector. The location of the building centroid is at a fixed distance from the domain walls. A vertical line going through the building centroid is the building's vertical axis, and it is about this axis that the building is rotated to achieve different wind incidence angles. For all CFD simulations the building height and width are kept constant, so different L/W ratios are achieved by varying the building length L. Two sets of dimensions were used to perform the single building simulations. As summarized in Table 3.4, Dimension Set #1 is used for cases 1a, 2a, 3 and Dimension Set #2 is used for cases 1b and 2b. The larger dimensions of Dimension Set #2 are required for these cases since they use a higher wind speed which causes convergence issues when attempting to solve with Dimension Set #1. These convergence issues are likely caused by the fact that pressure fluctuations of a minimum magnitude observed for the slower wind speed case spread farther out from the building for the higher wind speed case. As illustrated in Figure 3.9, if the higher wind speed case (Domain #2) uses Dimension Set #1 (Domain #1, dashed line in Domain #2) then the constant pressure outlet boundary condition comes into conflict with the pressure fluctuations as evidenced by the white region (pressure fluctuation greater than ± 1 Pa) indicated by the arrow in Domain #2 which lies beyond the outlet position for Domain #1.

Table 3.4: Dimensions of Single Building Flow Domain

Dimension	**Dimension Set #1 (cases 1a, 2a, 3)**	**Dimension Set #2 (cases 1b and 2b)**
Building width	2.5 m	2.5 m
Building height	25 m	25 m
Length from inlet to building centroid	$35W$	$35W$
Length from building centroid to outlet	$85W$	$165W$
Length from building centroid to side walls	$24W$	$50W$
Length from rooftop to top of domain	$36W$	$50W$

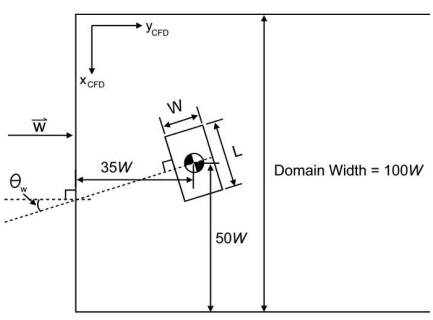

(a) Top view of flow domain (not to scale)

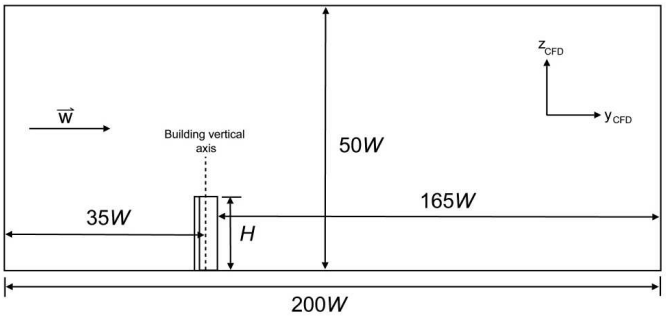

(b) Side view of flow domain (not to scale)

Figure 3.7: Single building flow domain

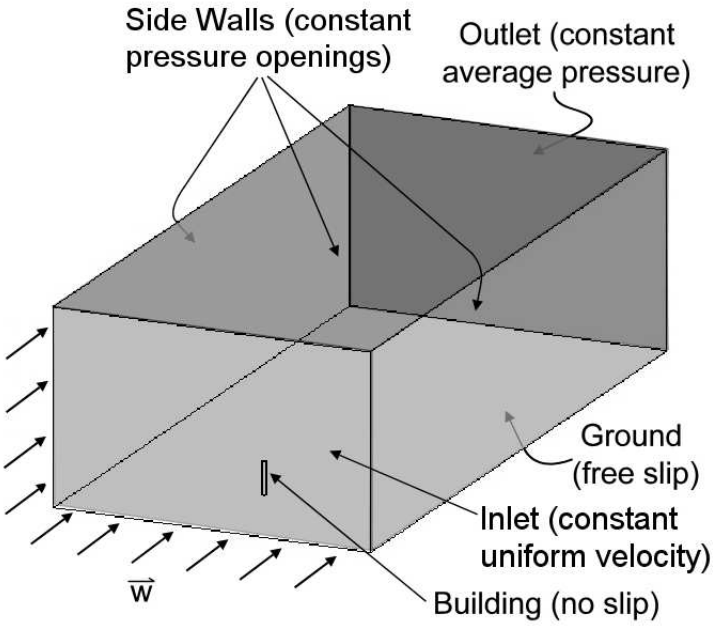

Figure 3.8: 3D view of single building flow domain

The wind incidence angle of all single building CFD simulations is within the range $0° \leq \theta_{W,CFD} \leq 90°$, whereas the 'true' wind incidence angle θ_W as defined previously in Section 2.2 can be in the range $0° \rightarrow 180°$. This is because all flows with $90° < \theta_W \leq 180°$ can be represented by CFD simulations with $0° \leq \theta_{W,CFD} \leq 90°$. As illustrated by Figure 3.10a, a single building flow with $90° < \theta_W \leq 180°$ is represented by a CFD simulation with $\theta_{W,CFD} = 180° - \theta_W$ provided the wind data is flipped about an axis with its origin at the building centroid and aligned with the wind ($+y_{CFD}$ axis). The implementation of this mapping with respect to flight simulation is discussed later in Sections 4.3 and 4.4

A single set of meshing parameters is used to discretize all single building flow domains in order to populate the single building WSD with CFD simulations. The choice of this mesh is a result of studying the grid convergence over three meshes. There is a coarse, medium, and fine mesh where each mesh is obtained by changing four variable meshing parameters. As the meshes progress from coarse to fine the meshing parameters change from larger to smaller length scales, and any meshing parameter that is being refined is done so by the same factor ('refinement factor') for coarse $\rightarrow$ medium and medium $\rightarrow$ fine refinement. The values for the refinement factors are obtained by setting the fine and coarse meshes and calculating the

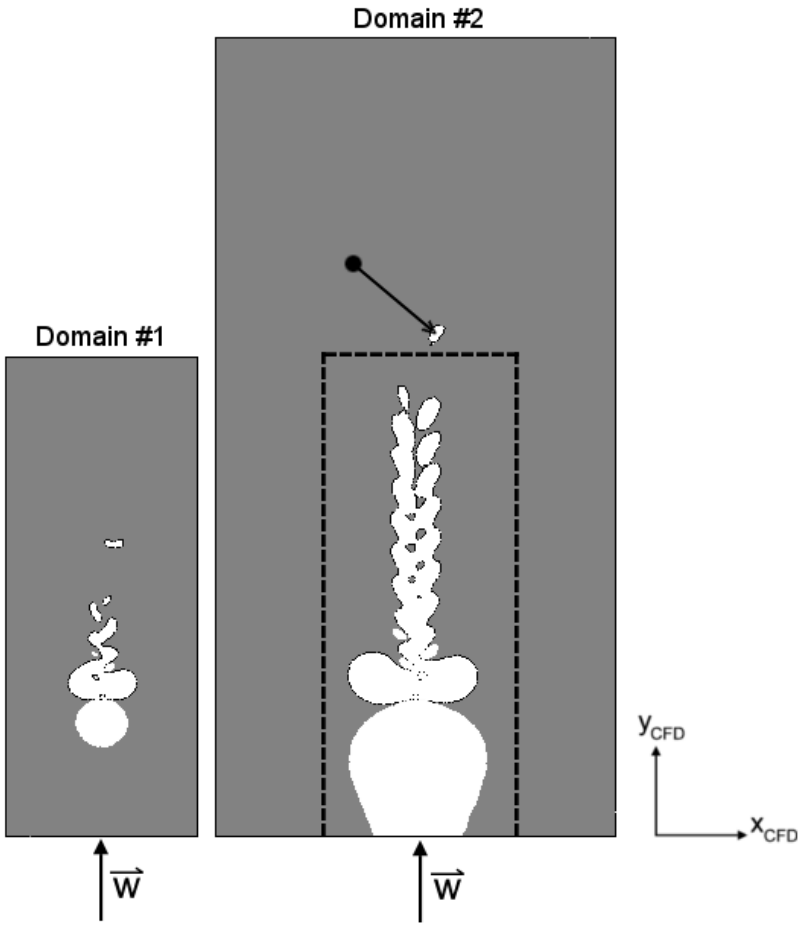

Figure 3.9: Top view (viewing plane at $z_{CFD}/H = 0.5$, H is building height) of the instantaneous single building case 1a ($L/W = 1, \theta_W = 0°, Re = 2.0 \times 10^6$) and 1b ($L/W = 1, \theta_W = 0°, Re = 4.73 \times 10^6$) flow regions at $t = 20$ s with a pressure differing at least ± 1 Pa from the reference pressure of $P_{ref} = 1$ atm (represented by the white area). Domain #1 and domain #2 correspond to cases 1a and 1b, respectively. The dashed line in the Domain #2 plot represents the size of Domain #1.

values of the four variable mesh parameters for the medium mesh such that they are larger than the coarse mesh and smaller than the fine mesh by the same factor. The fine mesh values are chosen to be as small as possible without the resulting mesh node count being much larger than 1×10^6, above which the required CPU simulation time was judged to exceed a practical limit (> 3 days) for the purposes of completing the thesis work. The coarse mesh values are chosen such that the node count is in between 4-9$\times$ less than the fine mesh count; a coarse mesh count in this range results in the medium mesh node count being larger than the coarse mesh and smaller than the fine mesh by a factor of $\sim$2-3$\times$.

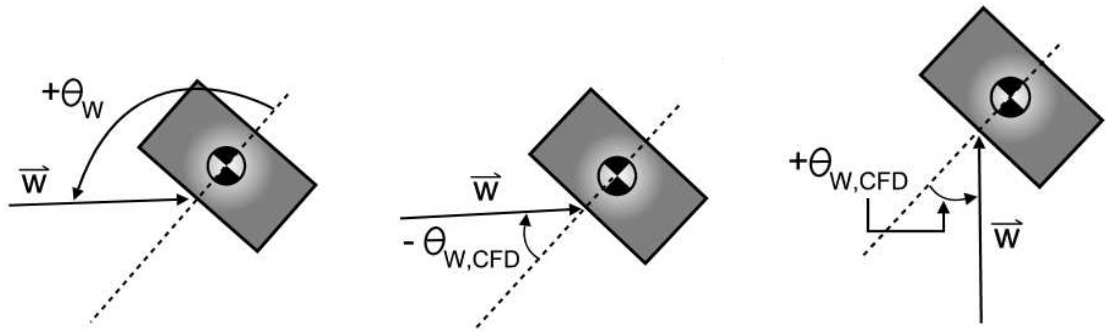

(a) Single building with $90° < \theta_W \leq 180°$

(b) Single building with $-\theta_{W,CFD}$, equivalent to θ_W

(c) Single building with wind data flipped and $+\theta_{W,CFD}$

Figure 3.10: Illustration of the relationship between $+\theta_{W,CFD}$ and θ_W where $90° < \theta_W \leq 180°$

For the purposes of this thesis, grid convergence is not claimed using a specific numerical criteria. Due to restrictions on computational resources and time the grid convergence study adopts a less formal approach and concentrates on the relative change of flow variables between subsequent mesh refinements. For example, if a flow variable differs by an amount between coarse and medium mesh solutions and the same flow variable differs by a lesser amount between medium and fine mesh solutions then this is considered to suggest grid convergence; it may indicate grid convergence is achieved for the medium or fine mesh or it may suggest that grid convergence can be achieved with a further refinment of the fine mesh.

With respect to the meshing parameters which are varied to obtain coarse, medium, and fine grids, inflation layers are important for the prediction of boundary layer separation so therefore the size of the inflation layers on the building surface are changed. To help capture flow effects due to the building's presence, the mesh length scale on the building edges, in the flow field immediately surrounding the building, and downstream of the building (in the approximate wake region) are also changed. Tables 3.5 and 3.6 summarize the meshing parameters of all three meshes investigated. Figure 3.11 shows a close-up of the inflation layers and the mesh in the flowfield immediately surrounding the building for all three meshes at $z_{CFD}/H = 0.5$. Figure 3.12 shows the wake refinement downwind of the building at $z_{CFD}/H = 0.5$ on a larger scale than Figure 3.11. Airflow around a single building with $L/W = 1$, $\theta_W = 0°$, and a wind velocity of 8.46 m/s is used for the grid independence study.

Table 3.5: Single Building Mesh Parameters

Mesh	**Base Mesh Length Scale (m)**	**Building Mesh Length Scale (m)**	**Inflation**	**Mesh Refinement Around Building**
1 (Coarse)	12.5	**1.03**	First Layer Thickness = **0.2m**, 5 prismatic layers, 1.1 expansion factor	Spherical volume, centred on building's vertical axis at 17.5 m ($7W$) vertical, mesh length scale = **1.03m**, 15 m ($6W$) radius, expansion factor = 1.2
2 (Medium)	12.5	**0.6** (0.58× Mesh 1 value)	First Layer Thickness = **0.1m** (0.5× Mesh 1 value), 5 prismatic layers, 1.1 expansion factor	Spherical volume, centred on building's vertical axis at 17.5 m ($7W$) vertical, mesh length scale = **0.6m** (0.58× Mesh 1 value), 15 m ($6W$) radius, expansion factor = 1.2
3 (Fine)	12.5	**0.35** (0.58× Mesh 2 value)	First Layer Thickness = **0.05m** (0.5× Mesh 2 value), 5 prismatic layers, 1.1 expansion factor	Spherical volume, centred on building's vertical axis at 17.5 m vertical ($7W$), mesh length scale = **0.35m** (0.58× Mesh 2 value), 15 m radius ($6W$), expansion factor = 1.2

Table 3.6: Single Building Mesh Parameters (cont'd.)

Mesh	**Mesh Refinement Downstream of Building**	**Node Count**
1 (Coarse)	Building vertical axis to 200 m from outlet, mesh length scale = **1.64m**, radius of influence = 7.5 m ($3W$), 19.5 m ($7.8W$) above ground	161021
2 (Medium)	Building vertical axis to 200 m from outlet, mesh length scale = **1.15m** (0.7× Mesh 1 value), radius of influence = 7.5 m ($3W$), 19.5 m ($7.8W$) above ground	371332 (2.9× Mesh 1 value)
3 (Fine)	Building vertical axis to 200 m from outlet, mesh length scale = **0.8m** (0.7× Mesh 2 value), radius of influence = 7.5 m ($3W$), 19.5 m ($7.8W$) above ground	1086762 (2.3× Mesh 2 value)

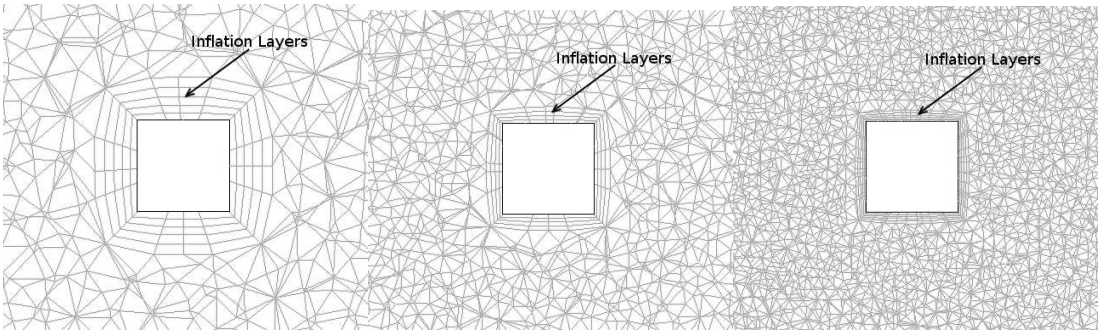

(a) Coarse mesh (b) Medium mesh (c) Fine mesh

Figure 3.11: Close up of mesh around building at $z_{CFD}/H = 0.5$

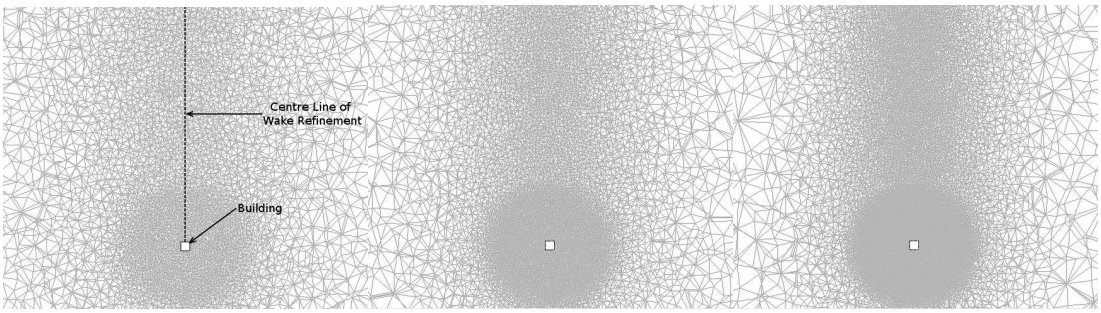

(a) Coarse mesh (b) Medium mesh (c) Fine mesh

Figure 3.12: Close up of mesh in approximate wake region at $z_{CFD}/H = 0.5$

The flow field for the grid independence study is solved using transient simulation setup 3 from Table 3.7. Turbulence is modeled using the standard $k - \epsilon$ formulation with scalable wall functions. No-slip boundary conditions are defined on the building surfaces and a free-slip boundary condition is specified on the ground surface (the surface boundary layer is not being modeled). The sides and outlet of the domain are assumed to be placed at a suitable distance from the building so that a constant freestream pressure could be specified as a boundary condition. Heat transfer is modeled using the Thermal Energy option which models the transport of enthalpy through the fluid domain, and is recommended for flows with a maximum Mach number less than 0.2 [60]. The transfer of heat across the domain boundaries (Inlet, Outlet, Side Walls, Building, and Ground from Figure 3.8) is governed by the specification of static temperature (T_w) or heat flux (q_w) at the boundaries. The Side Walls, Building, and Ground boundaries are specified as adiabatic ($q_w = 0$, recall that no heat transfer is assumed between the interior of the building and the surrounding flow) boundaries and the Inlet and Outlet

boundaries have a constant temperature specification of 25°C (same as the initial temperature from Table 3.7). The heat flux q_w across the inlet and outlet boundaries is calculated using the formula [60]

$$q_w = h_c \left(T_w - T_{nw} \right) \tag{3.2}$$

where T_{nw} is the near wall temperature and h_c is a heat transfer constant dependent on the turbulence model.

The convergence criteria refers to the convergence of flow field variables (momentum, pressure, mass, etc.) at each simulation time step, and the Maximum Number of Coefficient Loops parameter specifies the maximum number of iterations allowed at each simulation time step in order to achieve convergence. A convergence of 5.0×10^{-5} is considered tight convergence [60] and the convergence criteria of 5.5×10^{-5} (Table 3.7) is satisfied for all simulation times in all simulations (both single building and canyon) except for the first 0.1-0.3 s in a few cases. Of all single building simulations, setup 1 and 2 from Table 3.7 are only used for single building simulation cases 1b and 2b (Table 3.3) in order to overcome convergence issues (recall these cases have higher wind velocities). Setup 1 is a transient isothermal (same temperature everywhere in the flow) simulation running from 0-10 s, and setup 2 is a transient simulation with heat transfer (same heat transfer model as setup 3) running from 10-20 s using the setup 1 t =10 s results as initial values. No simualations are performed past $t = 20$ s, due to time considerations and the observation that the flow pattern from the last few seconds ($\sim 15 - 20$ s) becomes fairly regular with respect to the large scale structures.

The method of flight simulation in this first generation methodology does not allow for time-varying wind fields, so each entry in the Wind Simulation Database (WSD) is a static wind field taken from a specific simulation time. A discussion of how the simulation time for each entry in the WSD is chosen is left until the beginning of section 3.4.3.

The grid independence study results are taken from t =20 s, the last simulation time step. Figure 3.13 illustrates the locations where flow field data for the grid independence study is taken. The streamwise wall shear stress component is measured along a line on the rooftop which intersects the building centroid and is aligned with the background wind vector ('Wall shear measurement line'). This is an important physical variable since it indicates where flow

Table 3.7: Single Building Simulation Parameters

Parameter	**Value**
Simulation Type	Transient
Time Step	0.1 s
Time Duration	0 s - 10 s (Setup 1), 10 s - 20 s (Setup 2), 0 s - 20 s (Setup 3)
Fluid Model	Air as Ideal Gas
Reference Pressure	1atm
Initial Temperature	25°C (Setup 1 and 3), none specified (Setup 2)
Initial Flow Velocity	8.46 m/s (Setup 1 and 3), none specified (Setup 2)
Turbulence Model	k-ϵ
Heat Transfer Model	Isothermal (Setup 1), Thermal Energy with viscous dissipation (Setup 2 and 3)
Advection Scheme	High Resolution
Transient Scheme	2nd order backward Euler
Convergence Criteria	5.5×10^{-5}
Maximum Number of Coefficient Loops	15
Inlet Boundary Condition	Flow velocity normal to inlet = 20 m/s (Setup 1 and 2), 8.46 m/s (Setup 3)
Outlet Boundary Condition	Constant 0 Pa relative pressure (all setups), static temperature = 25°C (specified for Setup 1 only)
Boundary Condition on Domain Walls	Constant 0 Pa relative pressure openings (all setups), opening temperature = 25°C (specified for Setup 1 only)
Boundary Condition on Building Walls	No-slip, smooth wall (all setups), adiabatic (Setup 2 and 3)
Boundary Condition on Ground	Free-slip (all setups), adiabatic (Setup 2 and 3)

separation/attachment occurs. The streamwise wind velocity component is measured along vertical axes placed 0.25 building widths upwind and 1.25, 2 building widths downwind of the building centroid along a line lying in the plane of symmetry of the building about the y_{CFD} axis. In flows around buildings the wind aligned velocity component downstream of the building

varies significantly so it is an important physical quantity to investigate. The measurement lines are placed relatively close to the building since the wind gradients and turbulence diminish rapidly with increasing distance from the building. The exact values for the locations along the y_{CFD} axis are chosen to match the measurement locations of the validation case (to be discussed after the grid convergence study). The streamwise wind velocity component is also measured along horizontal axes aligned with the x_{CFD} axis placed at 1.25 and 2 building widths downwind of the building centroid at an altitude of $Z/H = 0.8$.

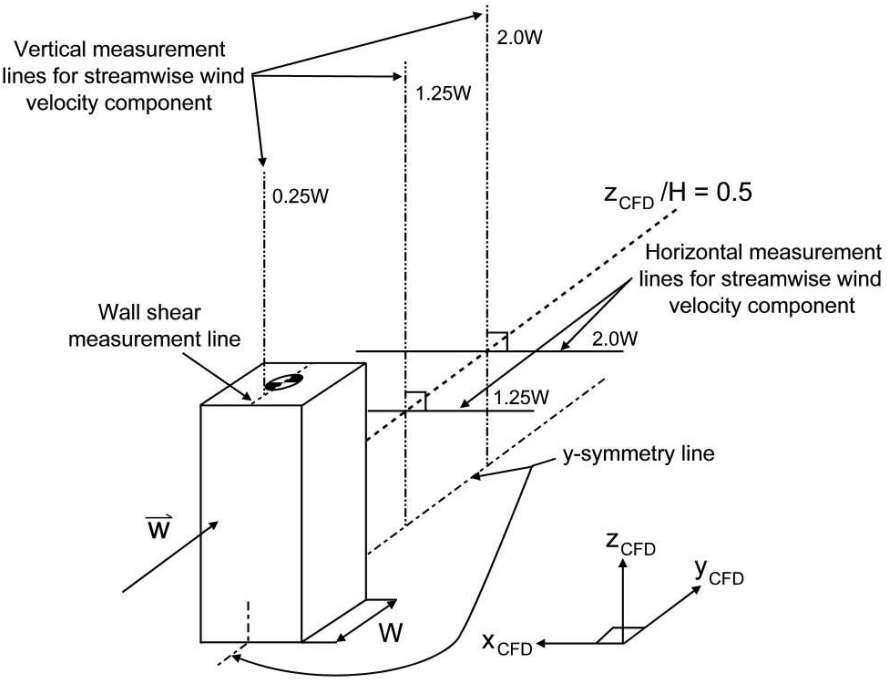

Figure 3.13: Locations used for grid independence study results (not to scale)

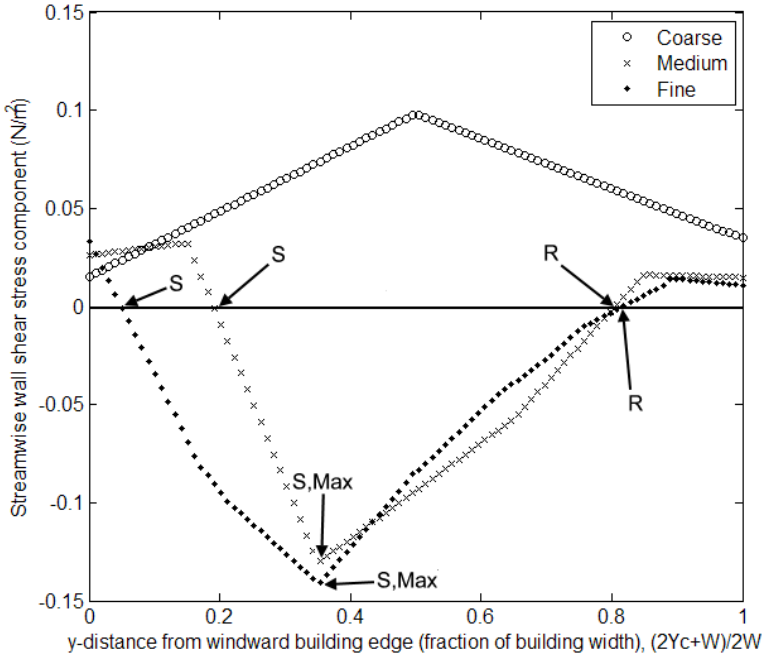

Figure 3.14: Comparison of wall shear on building roof

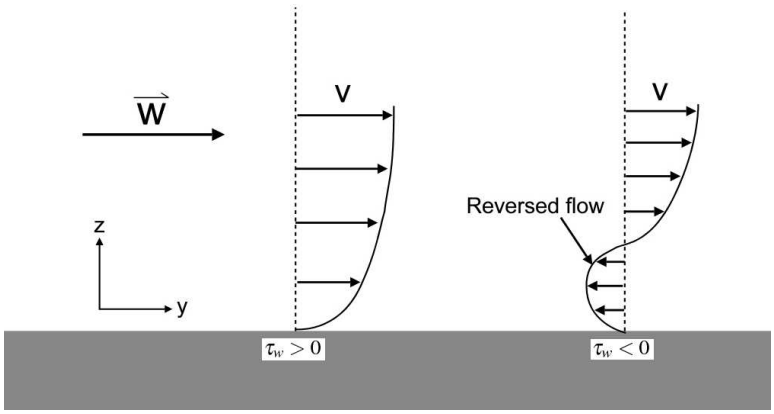

Figure 3.15: Illustration of boundary layer transition

Figure 3.14 compares the streamwise (background wind aligned) wall shear stress component profiles obtained from the three meshes. The x-axis plot variable is the distance from the windward building edge divided by the building width (W). With reference to the y_{CFD}-distance from the building centroid (Y_C), the x-axis plot variable is $\frac{W/2+Y_C}{W} = \frac{2Y_C+W}{2W}$. The results from the coarse mesh do not show any boundary layer separation, a phenomenon which occurs when the shear stress transitions from a positive to a negative value. As illustrated

in Figure 3.15 a transition from positive to negative shear is associated with reversed flow at the wall (negative $(dv/dz)_w$) since $\tau_w = \mu(dv/dz)_w$, where τ_w is the wall shear stress and μ is the dynamic viscosity of the air. Figure 3.16a is a vector plot of the flow velocity above the rooftop from the coarse mesh simulation showing an absence of reversed flow. Since boundary layer separation is expected to occur close to the windward edge, the coarse mesh is clearly not adequate. The medium and fine meshes both show boundary layer separation as evidenced from the shear stress plot (Figure 3.14, the 'S' labels indicate where seperation first occurs) and the vector plots of the flow velocity above the rooftop which show recirculation (Figures 3.16b and 3.16c). Although the separation point from the medium and fine meshes as shown in Figure 3.14 differs, one can see that the point of greatest flow reversal (most negative shear stress value) as indicated by the 'S,Max' labels matches quite well and past this point the medium and fine grids produce similar results. In particular, the point where the flow reattaches (transition from negative to positive shear) indicated by the 'R' labels for the medium and fine meshes is practically identical.

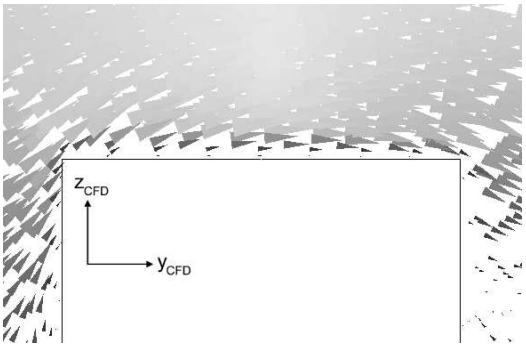

(a) Coarse mesh

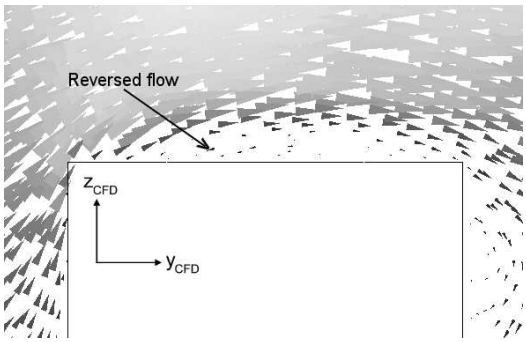

(b) Medium mesh

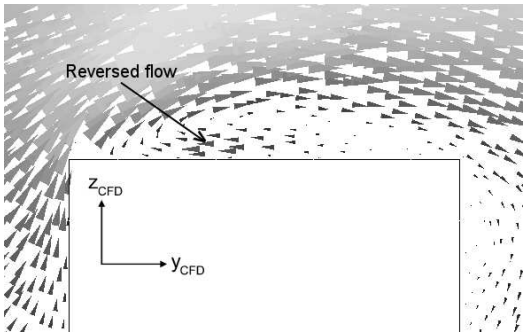

(c) Fine mesh

Figure 3.16: Vector plot of flow velocity above the rooftop for all three meshes showing the extent of flow reversal. The plots are taken from a plane aligned with the background wind and containing the building vertical axis.

Figures 3.17 - 3.18b compare the streamwise wind velocity component profiles measured along the vertical axes (Figure 3.13). The peak velocities above the roof as shown in Figure 3.17 (it should be noted that the Figure doesn't resolve the boundary layer) indicated by the 'P' labels suggest grid convergence when it is considered that the peak velocities increase as the mesh is refined and the difference between the coarse and medium mesh peak velocities (0.82 m/s) is larger than the difference between the medium and fine mesh peak velocities (0.69 m/s). Additionally, the peak velocities for the medium and fine meshes occur at practically the same z_{CFD}/H whereas the peak velocity for the coarse mesh occurs at $\Delta z_{CFD}/H \approx 0.042$ above that of the medium and fine meshes.

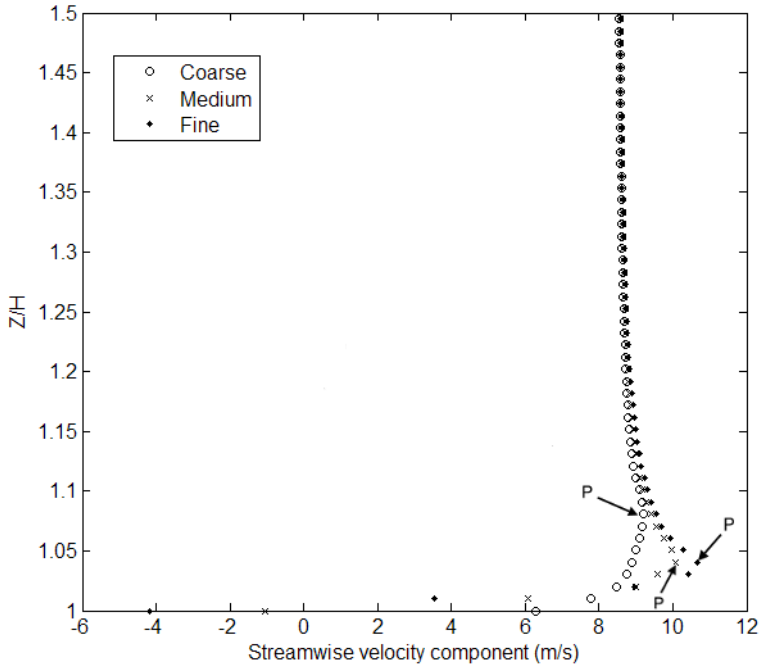

Figure 3.17: Comparison of wind-aligned velocity profiles at 0.25 building lengths upwind of building centroid

Figures 3.18a and 3.18b show good agreement between all meshes above $z_{CFD}/H \approx 0.85$, notably capturing the expected shear layer region between $z_{CFD}/H \approx 0.9$ and $z_{CFD}/H \approx 1.1$. Below $z_{CFD}/H \approx 0.65$ the medium and fine meshes agree with each other much better than with the coarse mesh. The region between $z_{CFD}/H \approx 0.9$ and $z_{CFD}/H \approx 0.65$ gives inconclusive results, with the coarse mesh results being generally closer to the fine mesh results in Figure 3.18a and the medium mesh results being generally closer to the fine mesh results in Figure

3.18b. In this region the flow is transitioning from the reversed and unsteady flow leeward of the building to a shear layer region where the flow accelerates to the background wind velocity. This implies that the solution in this region is more grid sensitive and a smaller simulation time step may be required for grid convergence due to the complexity of the transitioning flow and unsteady effects.

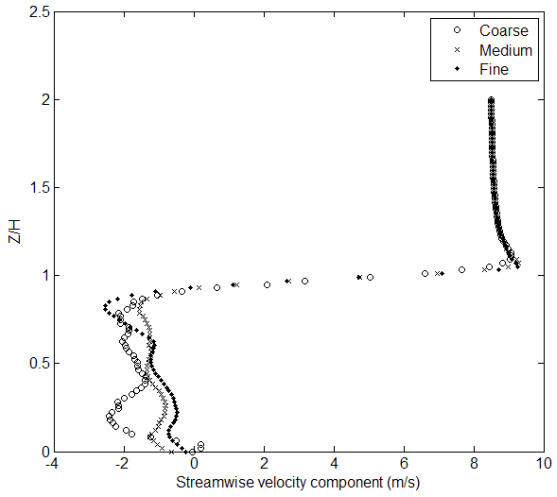

(a) Comparison of vertical wind aligned velocity profiles at 1.25 building lengths downwind of building centroid

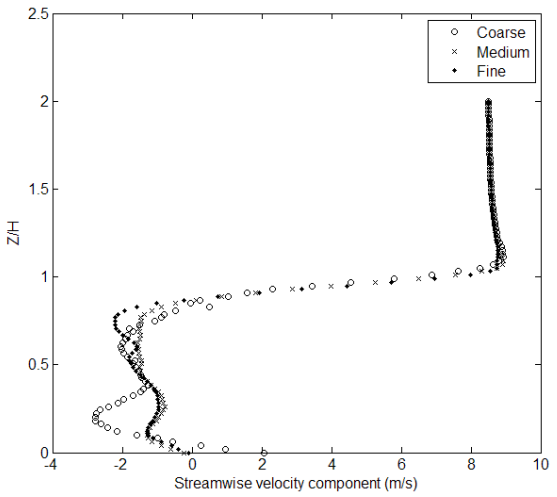

(b) Comparison of vertical wind aligned velocity profiles at 2 building lengths downwind of building centroid

Figure 3.18: Results of grid independence study (cont'd)

Figures 3.19a and 3.19b compare the streamwise wind velocity component profiles measured along the horizontal axes (Figure 3.13). The y-axis for Figures 3.19a and 3.19b uses the non-dimensional variable X_C/W, where X_C the distance from the building centroid along the x_{CFD} axis and W is the building width. Suggestion of grid convergence exists at the ends of the horizontal sampling axis ($-2 < X_C/W < 1.5$ and $1.5 < X_C/W < 2$) and in the shear layer regions ($-1 < X_C/W < -0.3$ and $0.3 < X_C/W < 1$). The results from the region above $X_C/W \approx -0.3$ and below $X_C/W \approx 0.3$ are inconclusive, but this is the transition region as previously discussed regarding Figures 3.18a and 3.18b since the results for Figures 3.19a and 3.19b are taken along horizontal axes at the same downstream locations as the vertical measurement axes (Figure 3.13) at a height of $z_{CFD}/H = 0.8$ (which is in the z_{CFD}/H range of the transition region). Therefore the same arguments with regards to the transition region in Figures 3.18a and 3.18b apply here. The results from the regions between the shear layer and the ends of the horizontal measuring axis ($-1.5 < X_C/W < -0.3$

and $0.3 < X_C/W < 1.5$) show a steady progression towards higher velocities as the grid is refined. However the progression from coarse to medium and the progression from medium to fine are roughly equal, so grid convergence in this region is not suggested. However this is a region where the shear magnitude significantly changes and the flow experiences a significant acceleration and therefore, as previously argued, should be expected to be sensitive to grid size and simulation time step (unsteady effects).

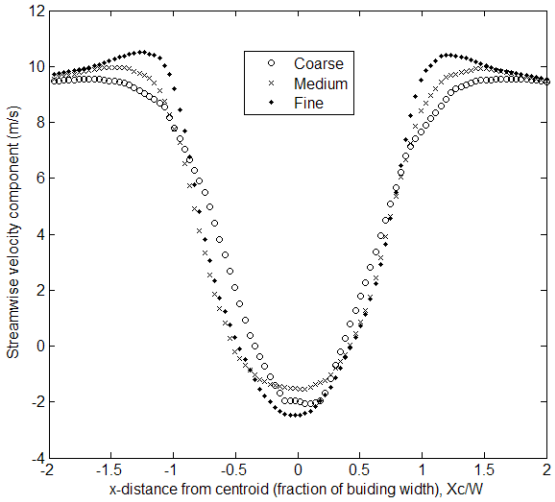

(a) Comparison of horizontal wind aligned velocity profiles at 1.25 building lengths downwind of building centroid

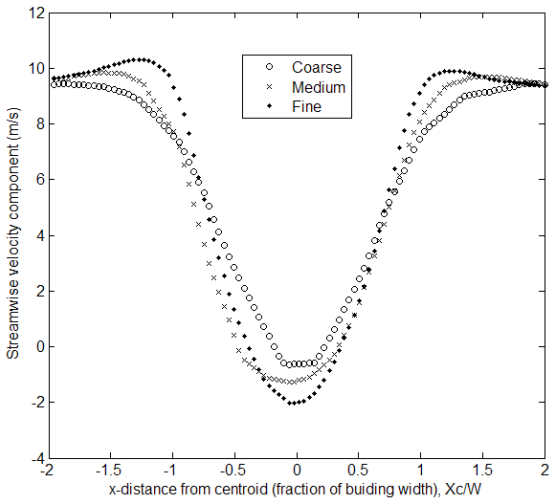

(b) Comparison of horizontal wind aligned velocity profiles at 2 building lengths downwind of building centroid

Figure 3.19: Results of grid independence study (cont'd)

Overall Figures 3.17 - 3.19b show suggestion of grid convergence in a significant portion of the flow, but it cannot be claimed that the solution is formally grid converged. In a few regions the coarse mesh actually agrees with the fine mesh better than the medium mesh agrees with the fine mesh, however there are too many regions where the coarse mesh gives significantly different results (especially with respect to boundary layer seperation) for it to be used to populate the WSD. The strongest evidence against grid convergence is found within highly unsteady flow regions and might be due to unsteady effects. However for the purposes of providing wind data for flight simulation the main flow features as predicted by the medium and fine meshes do not differ in an unacceptable manner (i.e. they agree on the basic large scale features of the flow). Since the medium mesh incurs much less computational cost than the fine mesh it is used for all other CFD simulations.

3.4.2 Single Building Flow Validation

Before single building CFD simulations are performed, an investigation into how well real single building flows are captured by the CFD software (Ansys CFX) is performed. In a paper by Tominaga *et al.* [58], various $k-\epsilon$ models are applied to the flow around a high-rise building model with the results being compared to experimental data gathered by Meng and Hibi [59]. The experimental setup illustrated by Figure 3.20a is a high-rise building model with $\theta_w = 0°$, $L/W = 1$, $Re = 2.40 \times 10^4$, and $H/W = 2$ placed within a surface boundary layer. The Reynolds number is calculated based on the building height H and the velocity at building height (U_H) taken from the experimental inflow velocity profile (Figure 3.20b), given as $U_H \approx 4.25$ m/s. This fixes the building height to be $H = 0.088$ m. The medium mesh from the grid independence study is used, but since the width of the building used for the grid independence study is different than that of the validation case (the building widths from grid independence study and validation case are 2.5 m and 0.044 m, respectively) all mesh length scale parameters are multiplied by factor of $0.044/2.5 = 0.0176$ to scale the mesh down to the appropriate size for the validation case. A modified version of CFD simulation setup 3 (Table 3.7) is used to match the experimental setup. The surface boundary layer for the CFD simulation is obtained by specifying inflation layers (with the same inflation parameters as summarized in Table 3.5, but scaled down to suit the validation case), a no-slip condition on the ground surface, and an inlet velocity profile which matches the inlet profile from experiment (Figure 3.20b). [59], [58] In addition, the boundary conditions at the side walls of the domain are symmetry planes (zero velocity component and zero scalar variable gradients normal to the wall) instead of being specified as constant pressure openings.

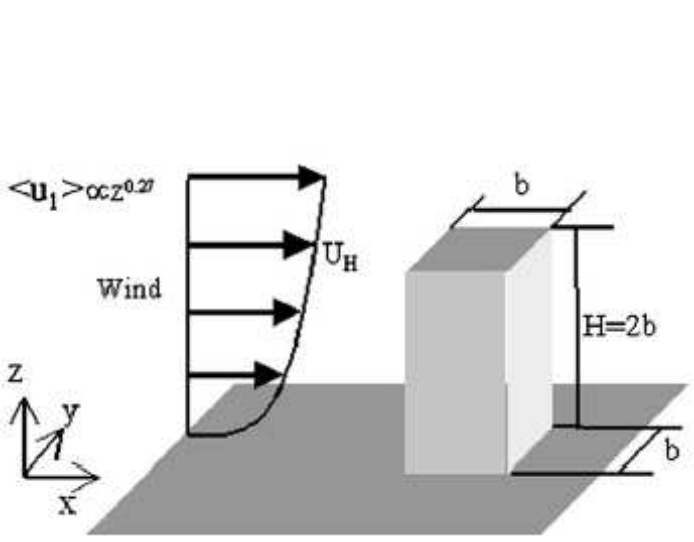

(a) Experimental setup [58], [59]

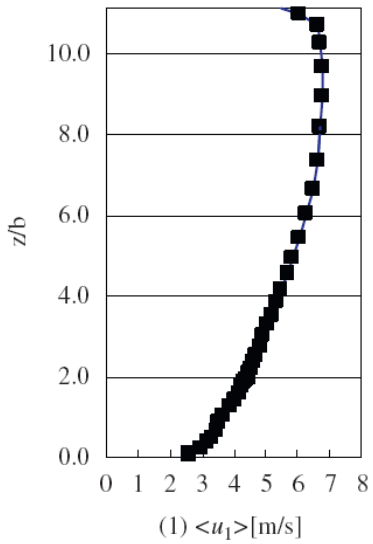

(b) Experimental inlet velocity profile. [58], [59] The variable u_1 is the streamwise velocity component.

Figure 3.20: Single building validation case

Figure 3.21 compares vertical streamwise velocity component profiles obtained from experiment and CFD simulation at the vertical measurement locations illustrated in Figure 3.13 ($0.25W$ upstream and $1.25W$, $2W$ downstream of the building centroid). The CFD data is the instantaneous data at $t = 20$ s (same time step used for the grid convergence study) and the data points represent the experimental data. Figure 3.22 shows the computational results of Tominaga *et al.* [58] where various revised k-ϵ turbulence models were used to compare with the same experimental data. Figure 3.21a compares velocities above rooftop-level ($Z/W = 2$) and decent agreement is observed between the shape of the velocity profile from the CFD solution and experiment. There is a failure of the CFD results to reproduce the peak velocity from experiment, an error of $\sim 0.25U_H$. This phenomenon was also observed by Tominaga *et al.* (Figure 3.22) for most turbulence models including the standard k-ϵ, supporting the confidence that CFX is solving the equations appropriately, even if the equations are not capturing some aspects of real flows.

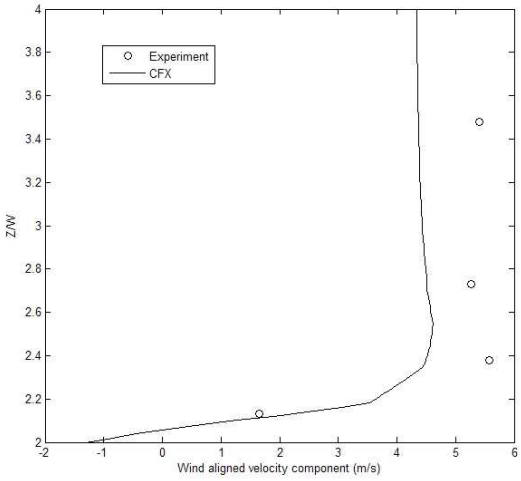

(a) Vertical profile of streamwise velocity component at $y = -0.25W$ from building centroid

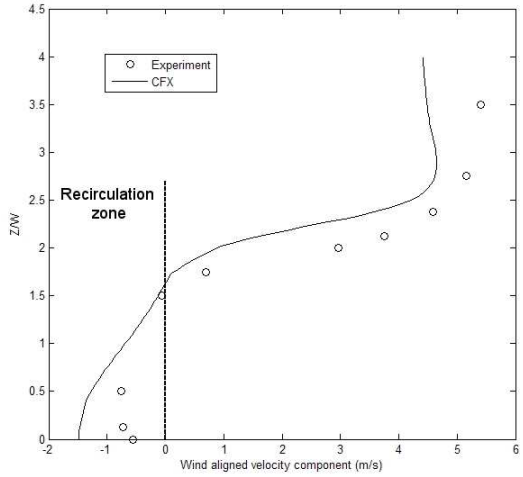

(b) Vertical profile of streamwise velocity component at $y = 1.25W$ from building centroid

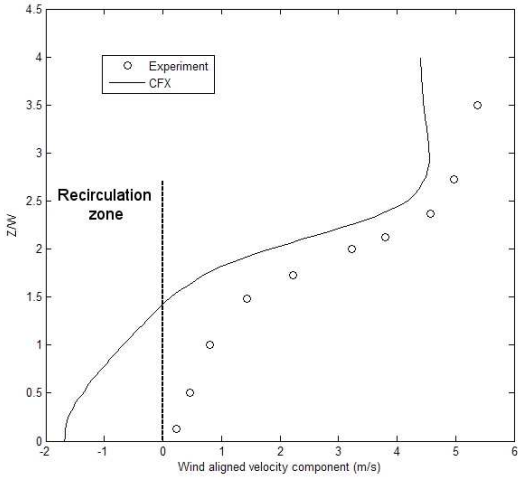

(c) Vertical profile of streamwise velocity component at $y = 2W$ from building centroid

Figure 3.21: Comparison of the vertical distribution of the streamwise velocity component

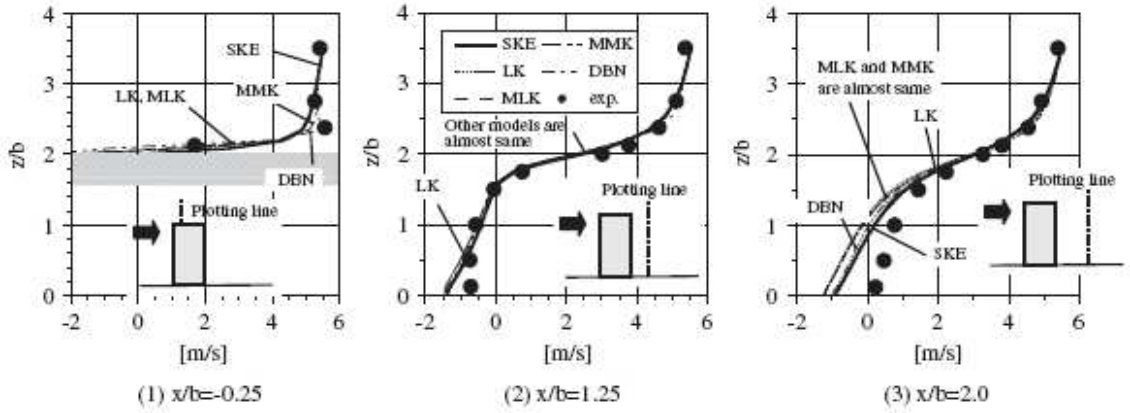

Figure 3.22: Comparison of the vertical distribution of the streamwise velocity component from Tominaga *et al.* [58]. 'SKE' stands for Standard k-ϵ.

Figure 3.21b shows good agreement with respect to the velocity gradient in the shear layer ($2 < Z/W < 2.5$) and both CFD and experiment show the flow reversing (going from positive to negative velocity, crossing the dashed line into the 'Recirculation zone' as labeled in Figure 3.21b) at similar Z/W values. The stronger flow reversal observed in the CFD results as opposed to experiment at low Z/W values is also seen to an extent in the results of Tominaga *et al.* (Figure 3.22). In addition, the results of Tominaga *et al.* show the experimental data points lying below the CFD curve in the shear layer region, a trend also seen in Figure 3.21b. The difference seen between CFD and experiment above $Z/W \approx 2.5$ is not echoed in the results of Tominaga *et al.*, but this region is not a recirculation zone or a shear layer and as such is of little practical interest. Figure 3.21c shows agreement similar to that of Figure 3.21b except for a complete absence of flow reversal in the experimental results while it is still present in the CFD results, indicating that the CFD recirculation zone extends further downwind of the building than the experimental recirculation zone. This was also observed by Tominaga *et al.* (Figure 3.22) and is confirmed by Figures 3.23a and 3.23b, which are a vector plots of the air velocity (from experiment [59] and CFD simulation, respectively) over the building taken from a plane cutting through building's mid-section. Overall the CFD results are in decent agreement with the experimental results, in particular with respect to the velocity gradients in the shear layers. The CFD results overpredict the extent and strength of the recirculation zone behind the building (Figures 3.23a and 3.23b), which suggests that the flow predicted by CFD is not overly optimistic, since an increase in the size and strength of the recirculation

zone is expected to have a worsening effect on aircraft flight. Since the two flow features of main interest are the shear layers and recirculation zones, this validation case suggests that the CFD results are a reasonably accurate and a conservative representation of reality.

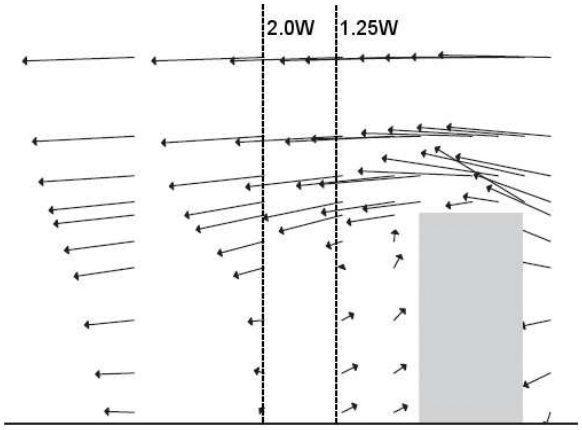

(a) Vector plot of wind velocity over building from experiment [59]

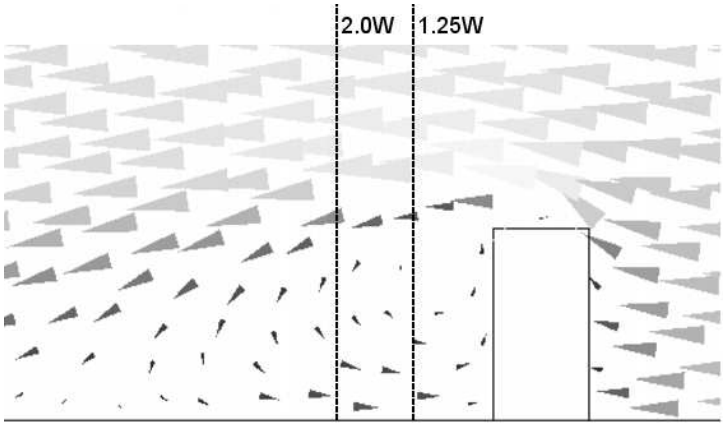

(b) Vector plot of wind velocity over building (CFD)

Figure 3.23: Comparison of flow over building. The recirculation zone from the CFD simulation extends significantly farther downwind of the building than from experiment. [59]

3.4.3 Results of Single Building Simulations

Figures 3.24 - 3.25c are a series of vector plots representing the instantaneous velocity field taken at $t = 20$ s from the case 1a simulation ($\theta_W = 0°, L/W = 1, Re = 2.0 \times 10^6$) in Table 3.3, obtained using CFD setup 3 from Table 3.7, and are intended to illustrate the major wind velocity gradients and different types of flow regions. The length of the arrowheads in the vector plots are directly proportional to wind speed. The selection of the simulation time from

which wind data is taken (forming an entry in the WSD) depends on an investigation of the flow field at different simulation times. The main flow features of interest around the case 1a simulation will first be discussed and then these features will be used to explain how specific simulation times are selected for all single building cases in the current WSD.

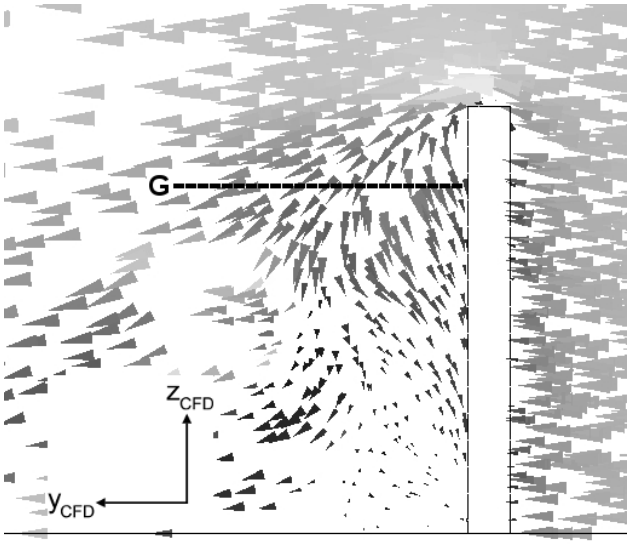

Figure 3.24: Side view of flow leeward of building, viewing plane passes through building centroid and is aligned with the background wind, $t = 20$ **s**

The flow over the building as illustrated in Figure 3.24 reveals that leeward of the building there is a recirculation zone in which the flow is partially reversed. If one imagines a horizontal line in this region (for example, the gradient line 'G' in Figure 3.24), the z_{CFD}-component of the wind velocity (w_W) noticeably varies along this line creating a dw_W/dy gradient. As an example of the importance of this gradient, if the aircraft is flying across the building wake in the $+x_{CFD}$ direction through the recirculation zone and the wings are level with the gradient line G then this gradient would exert a rolling moment on the aircraft. One may also expect a similar gradient located near the windward edge of the building as the air tries to rush over the building top. However the gradients in this region as seen in Figure 3.24 are much smaller than along gradient line G.

Figures 3.25a - 3.25b provide a top view of the wind field at various altitudes. Figure 3.25a is taken at an altitude half that of the building height, where the strongest velocity gradients were found to occur. Notice the asymmetry of the flow about the y_{CFD} axis, this is due to the transient nature of the flow. The main gradients of interest are encountered as the

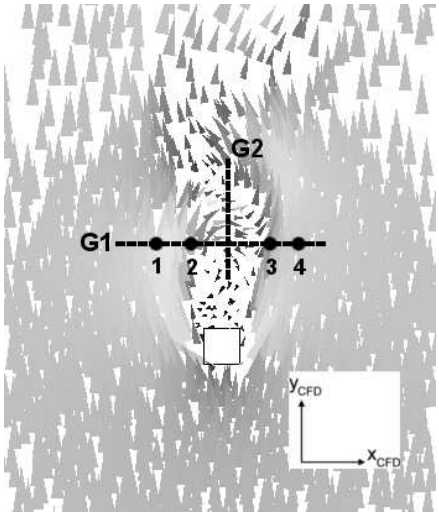

(a) Top view of flow around building, $z = 0.5H$

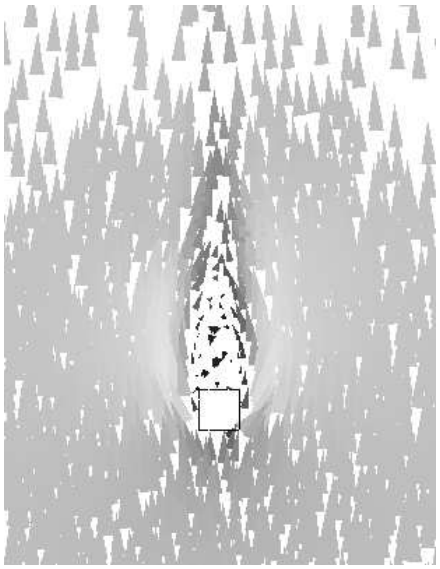

(b) Top view of flow around building, $z = 0.78H$

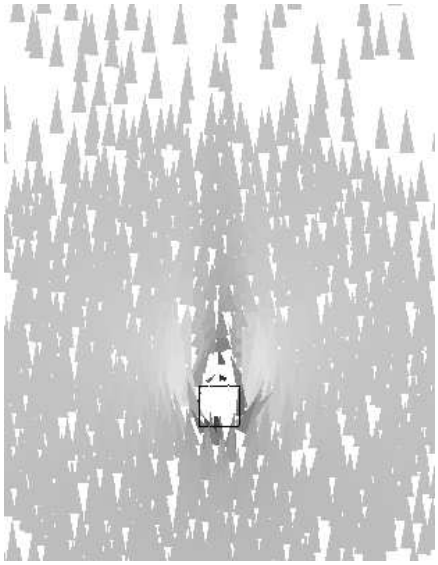

(c) Top view of flow around building, $z = 0.98H$

Figure 3.25: Vector plots of flow around case 1a single building, $t = 20$ s

gradient line G_1 (Figure 3.25a) is traversed from left to right ($+x_{CFD}$ direction). These are all gradients of the streamwise component with respect to $+x_{CFD}$ (dv_W/dx). The first of these gradients that are encountered are located at the positions labeled 1 and 2. At position 1 the streamwise velocity component (v_W) is increasing due to the acceleration of flow around the building before decreasing much more rapidly at position 2. This negative gradient dv_W/dx at 2 is due to the low velocity strip of air caused by the flow stagnation just leeward of the

building. The reverse situation is encountered as positions 3 and 4 are passed; there is a large positive gradient at 3 as the low velocity wake region is exited and a smaller negative gradient as the flow velocity decreases from the accelerated flow traveling around the building down to background conditions. Note that these flow conditions become much smoother and practically non-existent around 5 building widths downstream. If the aircraft is flying across the building wake along the G_1 gradient line from left to right, these gradients would cause yawing moments due to the variation of wind speed (and therefore aerodynamic force) along the fuselage. In addition, a x_{CFD} wind component gradient along G2 (du_W/dy) is setup due to recirculation behind the building causing a yawing and rolling moment on an aircraft crossing the wake along line G_1, since in this case the flow speed across the left and right wing platforms is different causing an imbalance in the lift produced. Figures 3.25b and 3.25c show a top view of the wind field at $z_{CFD} = 0.78H$ and $z_{CFD} = 0.98H$, respectively. It is observed that the gradients from the $z_{CFD} = 0.5H$ plane are significantly reduced as altitude increases.

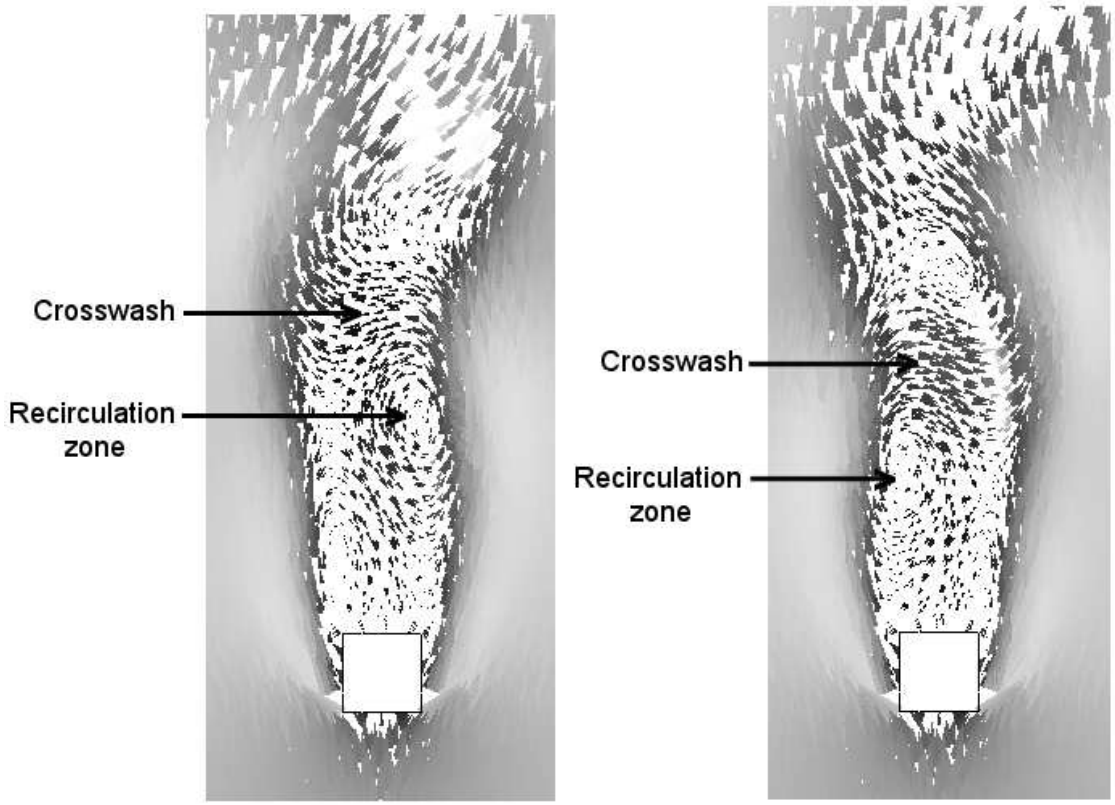

(a) $t = 19$ s (b) $t = 20$ s

Figure 3.26: Comparison of flow around case 1a building at $t = 19$ s and $t = 20$ s

Figure 3.26 demonstrates how the top view of the flow field around the case 1a building simulation at z_{CFD}/H changes from $t = 19s$ to $t = 20s$ (no significant differences are observed for the side view). The essential differences are the curvature of the low velocity strip of air, the direction, strength, and location of the 'crosswash' as labeled in Figure 3.26, and the strength of the large-scale eddies ('recirculation zones'). The investigation of these differences for various simulation times is used to judge which simulation time is most appropriate for inclusion in the WSD (that is which simulation is expected to produce a worst-case scenario with respect to flight past the building). As previously discussed with reference to Figure 3.25a, the biggest concern is with the velocity gradients caused by the strip of low velocity air (as G_1 is traversed). Although the curvature of the low velocity strip changes with simulation time, these velocity gradients within a few building widths downstream of the building (where they are the strongest) do not significantly change with simulation time. The deciding factors are the crosswash and large-scale eddies. From Figure 3.26 one can see that the crosswash from $t = 20$ s is stronger than from $t = 19$ s, and the large-scale eddies from $t = 19$ s are stronger than from $t = 20$ s. It is judged that the difference in crosswash strength creates more adverse conditions for aircraft flight (in terms of yawing moments) than the difference in the strength of the large-scale eddies and so $t = 20$ s is preferred for entry into the WSD. Comparison of the $t = 20$ s results with other simulation times is done in a similar way, and it is found that $t = 20$ s gives a reasonable estimation of the worst-case flow around the building. The simulation times for all other single building entries in the WSD are similarly chosen.

Figure 3.27 is a vector plot of the instantaneous velocity field at $t = 18$ s for case 1b ($\theta_W = 0°, L/W = 1, Re = 4.73 \times 10^6$). The main difference between case 1a and 1b is that the velocity gradients are stronger for case 1b since the flow stagnates behind the building for both cases but the case 1b simulation has a higher background wind velocity.

Figures 3.28 and 3.29 demonstrate how the flow field changes with wind incidence θ_W. As θ_W goes from $0° \rightarrow 22.5°$ the basic structure of the flow over the building (Figure 3.28a, along the midplane leeward of the building, $t = 19$ s) doesn't vary much, but the strip of low velocity air behind the building (Figure 3.28b) is slightly twisted to the right with a stronger recirculation zone about one and a half building widths downstream of the building. As θ_W goes from $22.5° \rightarrow 45°$, the flow over and around the building significantly changes. Compared

to the other cases, Figure 3.29a (t = 20 s) shows the air taking longer to accelerate back towards the background wind velocity after flowing over the building. Figure 3.29b supports this observation as the large, low velocity region is clearly visible even at $\sim 5W$ downstream of the building. There is also a noted lack of recirculation behind the building in the form of crosswash or large-scale eddies, which is likely due to the fact that for the given building geometry the 45° wind incidence results in the best aerodynamic configuration. To further illustrate this point, Figures 3.30a and 3.30b are vector plots of the flow velocity for the case 1a ($\theta_W = 0°, L/W = 1, Re = 2.0 \times 10^6$) and case 3 ($\theta_W = 45°, L/W = 1, Re = 2.0 \times 10^6$) building simulations taken from a horizontal plane at $z_{CFD}/H = 0.5$. The case 1a plot shows significant flow separation and recirculation along the building sides joining corners 1, 2 and 3, 4. On the other hand, the case 3 plot shows no discernible flow separation along the building sides joining corners 1,2 and 1,3. This lack of flow separation along the building sides qualifies θ_W as an aerodynamic configuration and accounts for the absence of large-scale recirculation zones in Figure 3.29b. This may also explain the fact that the strip of low velocity air is straighter and extends longer than for the other cases; if there is less large-scale downstream of the building, it is expected that there is less mixing of the high velocity air with the low velocity air.

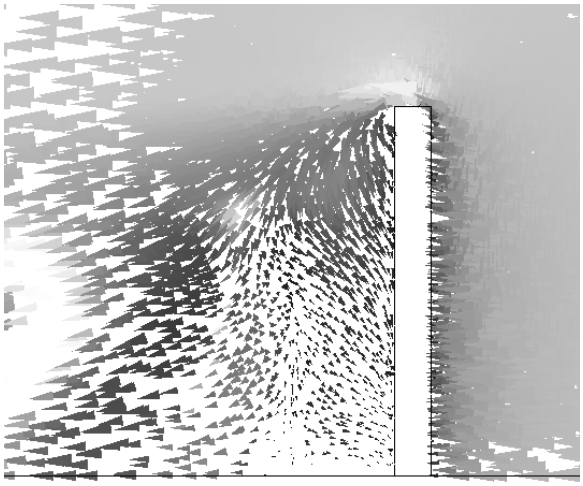

(a) Side view of flow leeward of building, viewing plane passes through building centroid and is aligned with the background wind

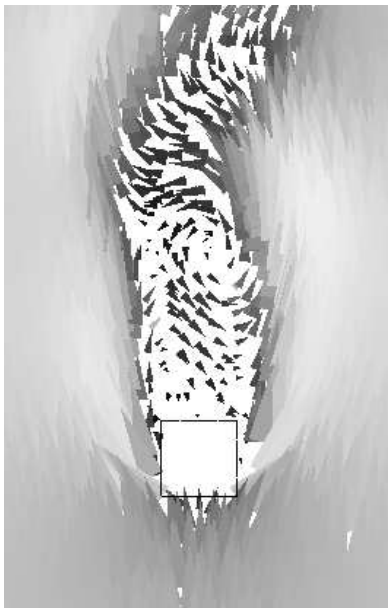

(b) Top view of flow around building, $z = 0.5H$

Figure 3.27: Vector plots of flow around case 1b single building, $t = 18$ s

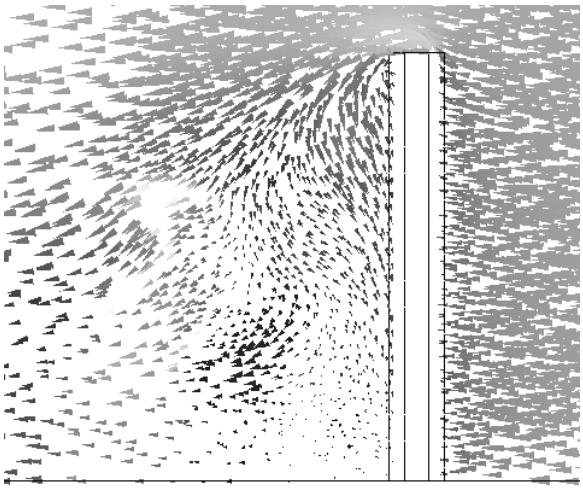

(a) Side view of flow leeward of building, viewing plane passes through building centroid and is aligned with the wind

(b) Top view of flow around building, $z = 0.5H$

Figure 3.28: Vector plots of flow around case 2a ($\theta_W = 22.5°, L/W = 1, Re = 2.0 \times 10^6$) single building, $t = 19$ s

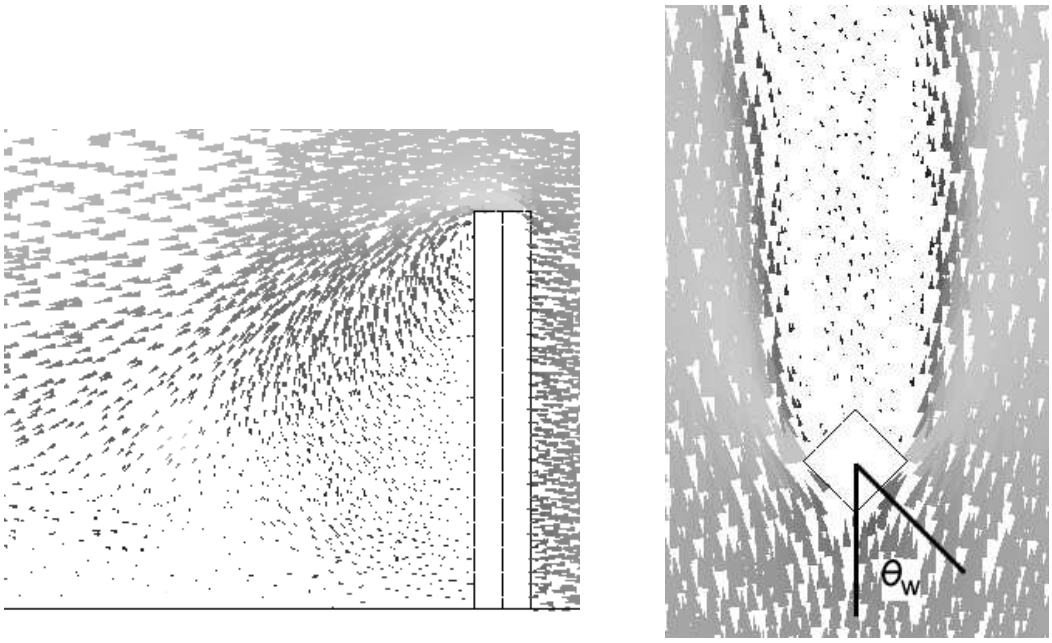

(a) Side view of flow leeward of building, viewing plane passes through building centroid and is aligned with the wind

(b) Top view of flow around building, $z = 0.5H$

Figure 3.29: Vector plots of flow around case 3 ($\theta_W = 45°, L/W = 1, Re = 2.0 \times 10^6$) single building, $t = 20$ s

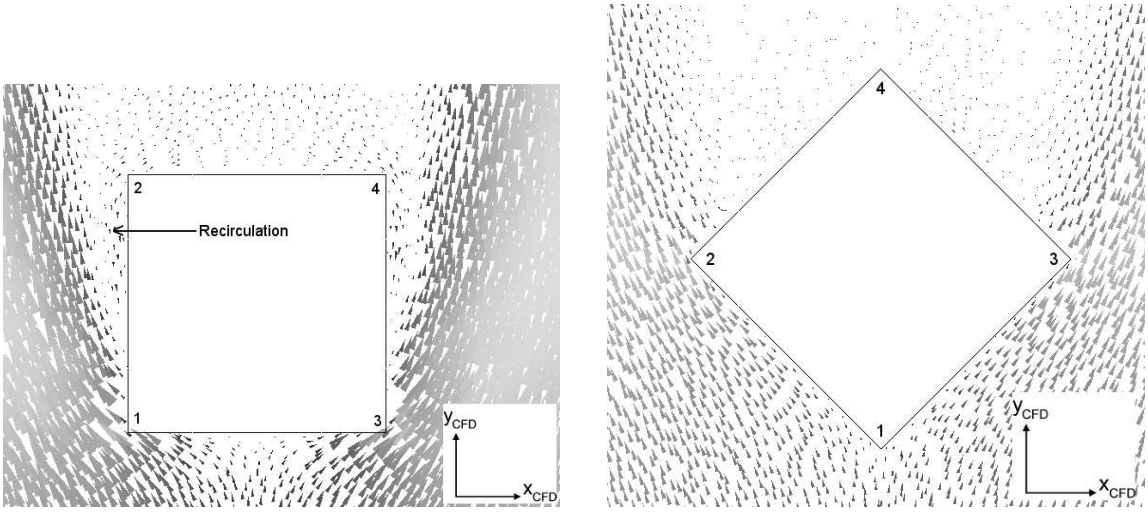

(a) $\theta_W = 0°$

(b) $\theta_W = 45°$

Figure 3.30: Vector plots of flow along the building sides of the case 1a ($\theta_W = 0°, L/W = 1, Re = 2.0 \times 10^6$) and case 3 ($\theta_W = 45°, L/W = 1, Re = 2.0 \times 10^6$) single building simulations

In addition to providing the information necessary to determine the aerodynamic forces and moments on the aircraft due to urban wind, the wind velocity field solutions are also used to determine the volume of air in each CFD simulation that is significantly affected by the presence of the building. This volume is called the building wake and it is essential for flight simulation in an urban wind environment. Figure 3.31 shows two cross-sections of the wake from the case 1a simulation ($\theta_W = 0°, L/W = 1, Re = 2.0 \times 10^6$) from Table 3.3. The wake is represented by the white area, defined as the region of the flow whose streamwise velocity components differ by more than $\pm$ 5% from the background wind velocity.

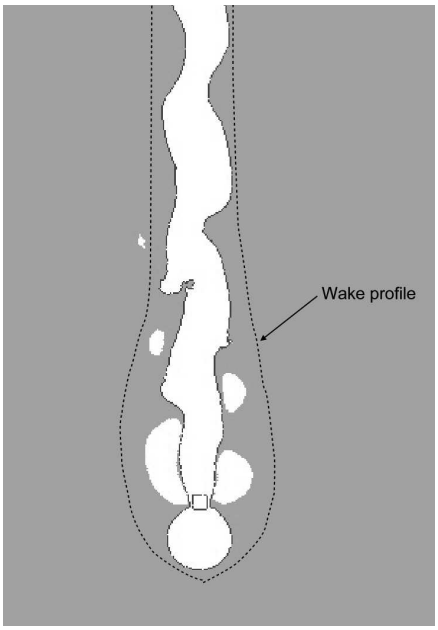

(a) Top view of wake shape profile, wind speed = 8.46 m/s

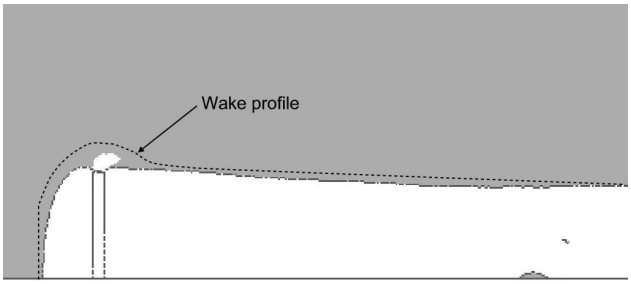

(b) Side view of wake shape profile, wind speed = 8.46 m/s

Figure 3.31: Top and side views of $(L/W, \theta_W, Re) = \left(1, 0°, 1.9 \times 10^6\right)$ wake shape (case 1a)

The shape of the wake volume for each entry in the WSD must be stored in order to use it for flight simulation. The dashed lines in Figure 3.31 represent the two cross-sections that are used to define an analytical wake boundary. This definition is based on only two wake sections but is a useful conservative approximation since simulations have shown that cross-sections taken through the vertical and horizontal centres of the building tend to generate the largest wake profiles. It can be viewed as an extrusion of the profile in Figure 3.31a from the ground up with a variable height defined by Figure 3.31b. Together these profiles

create a volume similar to that illustrated by Figure 3.32. A spline fit is used to represent the wake boundaries in Figures 3.31a and 3.31b as piecewise analytical functions $f_L(y_{WCH})$, $f_R(y_{WCH})$, and $h(y_{WCH})$ as shown in Figures 3.33a and 3.33b. The dependent variable y_{WCH} is the coordinate along a streamwise horizontal axis placed at the building centroid at rooftop height. Defining z_{WCH} as a vertical axis positive upwards and x_{WCH} as a horizontal axis completing the right-handed coordinate system convention, the axes x_{WCH}, y_{WCH}, and z_{WCH} form a basis for the Wind-Centroid-Height (WCH) coordinate frame.

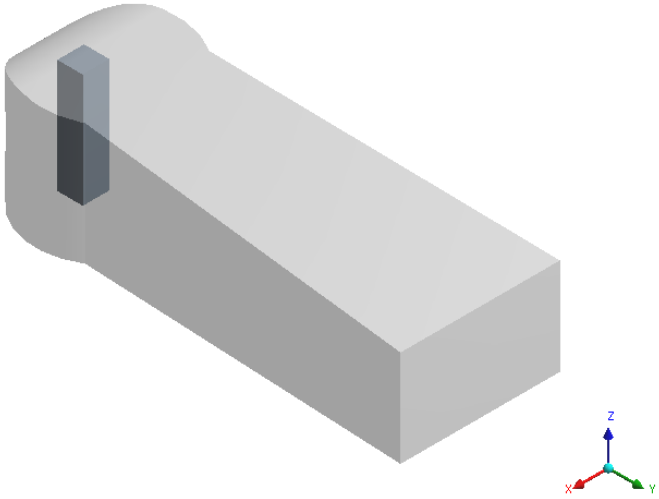

Figure 3.32: 3D wake shape

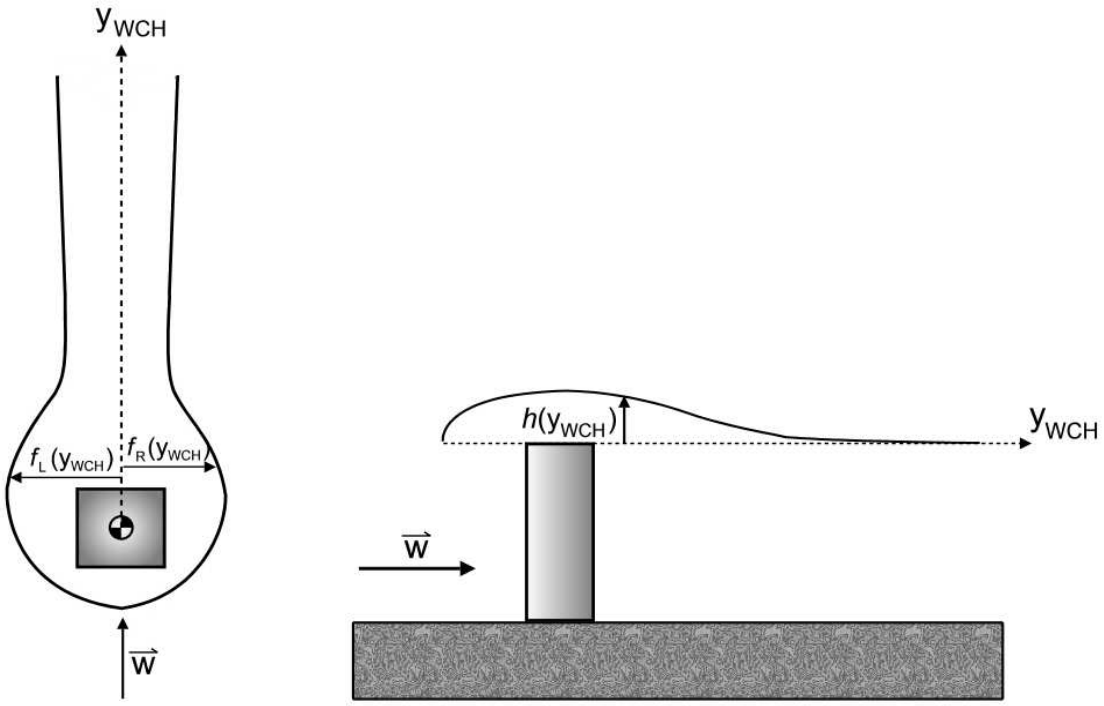

(a) Top view of wake

(b) Side view of wake

Figure 3.33: Specification of wake boundaries

As illustrated by Figure 3.34, the splines used to create the wake boundary functions are fully defined by specifying the location of control points and end slopes for each function. The location of each indexed control point in the top view (Figure 3.34a) is defined by the non-dimensional distances $\frac{x_{WCH}}{D}$ and $\frac{y_{WCH}}{D}$ (where D is the characteristic length of the building). The end slopes of the top view boundary functions are $s1_L$, $s8$, $s9$, and $s1_R$, defined at control points 1, 8, 9, and 1, respectively. The slopes are calculated with the change in x_{WCH} as the 'rise' and the change in y_{WCH} as the 'run' (i.e. slope = $\frac{\Delta x_{WCH}}{\Delta y_{WCH}}$). There are two slopes defined at control point 1 ($s1_L$ for the left boundary function and $s1_R$ for the right boundary function) because of the discontinuity. Each control point in the side view of the wake profile as illustrated in Figure 3.34b is defined by the non-dimensional distances $\frac{y_{WCH}}{D}$ and $\frac{z_{WCH}}{D}$. The end slopes of the side view (slope = $\frac{\Delta z_{WCH}}{\Delta y_{WCH}}$) boundary functions are $s1$ and $s7$, defined at control points 1 and 7, respectively.

For a given entry in the WSD, the wake shape information corresponding to that entry is stored in a unique `.txt` file, called the Wake Shape File (WSF), for reference during flight simulation. The file is named as per the conventions laid out in Section 3.3, and each WSF must

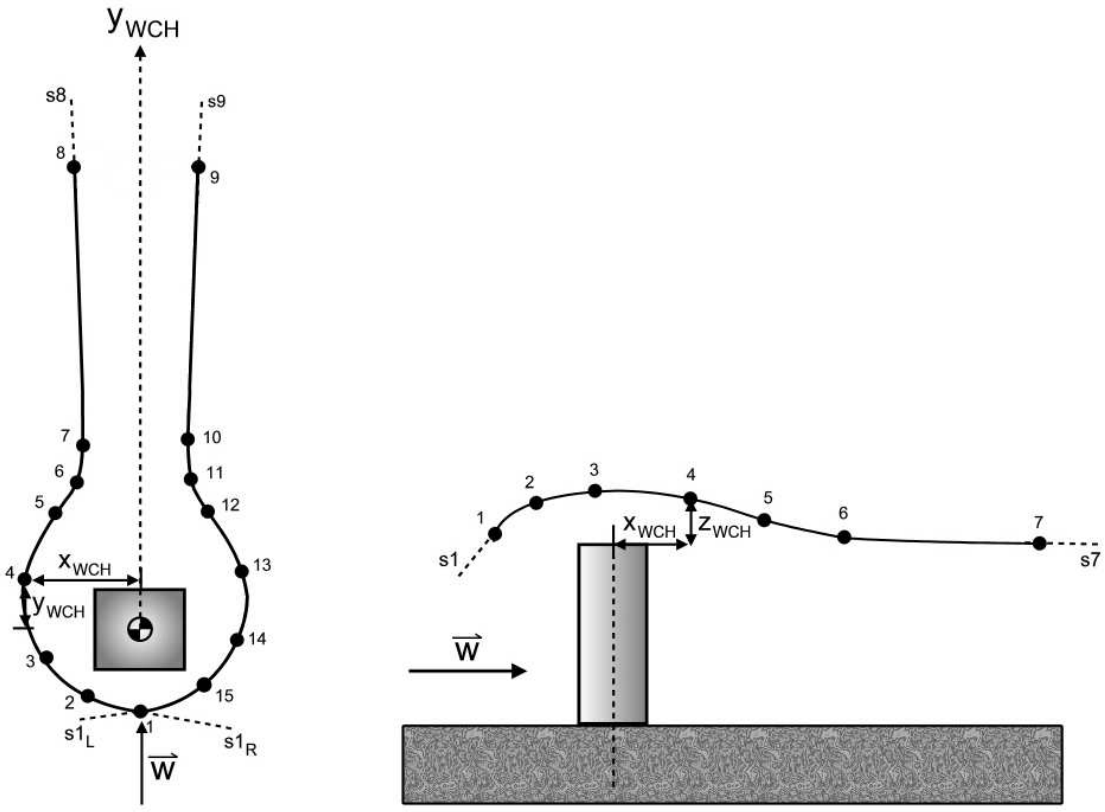

(a) Top view of wake boundary spline control points

(b) Side view of wake boundary spline control points

Figure 3.34: Illustration of control points and slopes used to define wake boundary splines

include the non-dimensionalized locations of the control points and the function end slopes. As illustrated in Figure 3.35 all the wake shape data for a given wake is contained in a single string of numbers, starting (left to right) with the $\frac{y_{WCH}}{D}$, $\frac{x_{WCH}}{D}$, and slope values for the first control point of the left wake shape function $f_L(y_{WCH})$. The next data entries are the $\frac{y_{WCH}}{D}$ and $\frac{x_{WCH}}{D}$ values of the second control point of $f_L(y_{WCH})$, followed by the $\frac{y_{WCH}}{D}$ and $\frac{x_{WCH}}{D}$ values of all the other control points of $f_L(y_{WCH})$ and then the slope of the final control point of $f_L(y_{WCH})$. The right wake shape function $f_R(y_{WCH})$ and wake height function $h(y_{WCH})$ are defined in the same manner, with $\frac{y_{WCH}}{D}$ and $\frac{z_{WCH}}{D}$ specified for the control point locations of $h(y_{WCH})$.

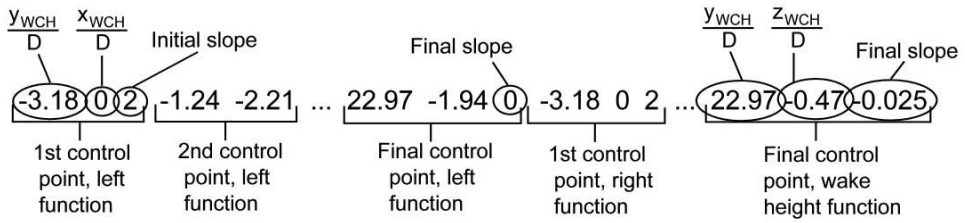

Figure 3.35: Storage of wake shape

3.5 Canyon Simulations

Tables 3.8 and 3.9 describe the canyon cases investigated using CFD. Recall from Section 3.2.2 that each point in the Canyon Configuration Space (CCS) corresponding to an entry in the CWSD is located by 7 parameters (as opposed to 3 for single buildings) describing wind speed, wind direction, and canyon geometry. The canyon cases investigate the effect these parameters have on the flow, in particular wind speed, wind direction, and the S/H ratio which governs the flow type (skimming flow, wake-interference flow, or isolated roughness flow). Figures 3.36a and 3.36b illustrate the geometry of the flow domain used for all canyon simulations, the 3D shape of which is the same as for the single building simulations (Figure 3.8, Section 3.4.1). The location of the canyon centroid is at fixed distance from the domain walls. A vertical line going through the canyon centroid is the axis about which the two buildings are rotated to achieve different wind incidence angles. For all CFD simulations the average building height and minimum building edge length (W_{-}) are kept constant. The dimensions for the flow domain are summarized in Table 3.10.

Table 3.8: Canyon Cases Currently Populating the CCS

Case #	**Wind Incidence Angle**	**Wind Speed (m/s)**	$(R_\perp/R_{\|\|})_{ww}$ **value**	$(R_\perp/R_{\|\|})_{lw}$ **value**	S/H **value**	**Flow Type**
1a	0°	8.46	2	2	1	Skimming flow
1b	0°	20	2	2	1	Skimming flow
2	90°	8.46	2.5	2.5	0.1	Skimming flow
2b	90°	20	2.5	2.5	0.1	Skimming flow
3a	22.5°	8.46	1	2	2.25	Wake-interference flow
3b	22.5°	20	1	2	2.25	Wake-interference flow

Table 3.9: Canyon Cases Currently Populating the CCS (cont'd.)

Case #	$\Delta H/D_{avg}$	H_{avg}/D_{avg}	**Corresponding** D_{real} **value (m)**
1a	0	2	12.16
1b	0	2	28.74
2a	0	3.79	14.64
2a	0	3.79	34.6
3a	-1	4.03	13.77
3b	-1	4.03	32.55

A form of Mesh 2 (Tables 3.5 and 3.6), adapted for use with canyons, is used. The building edge mesh length scale is applied to both buildings, the mesh refinement previously defined as centred on the single building centroid at a height of $7W$ is centred on the canyon centroid at a height of $8W_-$ (since the average canyon simulation height is slightly larger than the single building simulation height, and if there is a non-zero ΔH the taller building is even greater than the average height), and the wake refinement previously defined as starting from

Table 3.10: Dimensions of Canyon Flow Domain

Dimension	Value
Smallest building width (W_{-})	2.5 m
Average building height	$10.2W_{-}$
Domain length	$200W_{-}$
Domain width	$100W_{-}$
Domain height	$50W_{-}$
Length from inlet to windward building centroid	$35W_{-}$
Length from canyon centroid to to side wall	$50W_{-}$

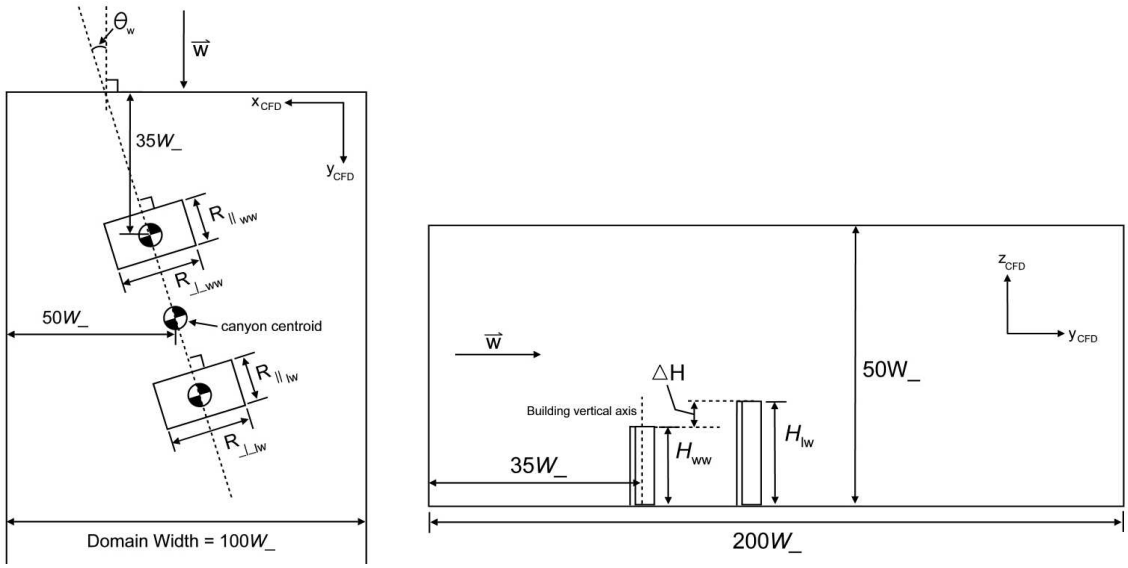

(a) Top view of flow domain (not to scale)

(b) Side view of flow domain (not to scale)

Figure 3.36: Canyon flow domain

the single building centroid at a height of $7.8W$ with a radius of influence of $3W$ starts from the canyon centroid at a height of $6W_{-}$ with a radius of influence of $4W_{-}$ (since canyons are generally wider than single buildings). The CFD simulation settings for all canyon cases use setup 3 from Table 3.7.

The wind incidence angle of all canyon flows in an urban environment is within the range $0° \leq \theta_W < 360°$, as defined previously in Section 2.2, but are represented by CFD simulations with $0° \leq \theta_{W,CFD} \leq 90°$. In some cases this representation requires the wind data to be flipped about an axis with the canyon centroid as the origin and aligned with y_{CFD} similar to the

process used for single buildings as illustrated in Figure 3.10. Furthermore, it is a necessary convention that all CFD simulations with $\theta_{W,CFD} = 90°$ place the building with the larger $R_{||}$ farther along the $+x_{CFD}$ axis than the other building, as illustrated by Figure 3.37. Figure 3.38 and Table 3.11 show how different ranges of θ_W are represented by CFD simulations all within the range $0° \leq \theta_{W,CFD} \leq 90°$. Recall that when $\theta_{W,CFD} = 90°$, the windward building is the building with the smaller edge length parallel to the canyon axis ($R_{||}$).

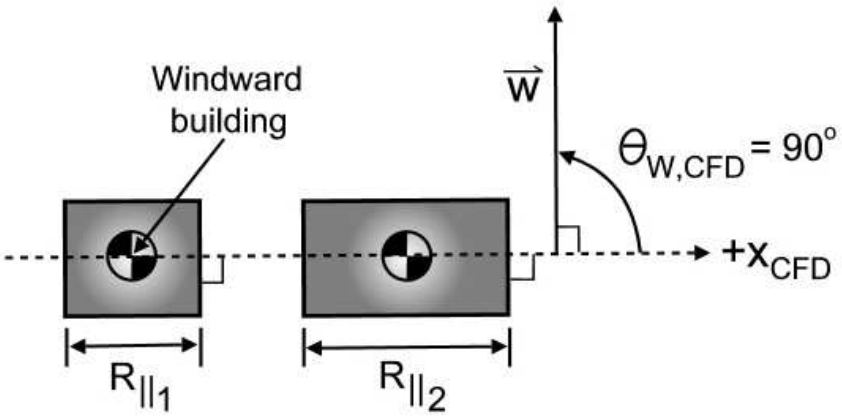

Figure 3.37: Illustration of canyon building placement for CFD simulation when $\theta_{CFD} = 90°$. The windward building is the one with the larger $R_{||}$ (in this case, building 2 since $R_{2||} > R_{1||}$)

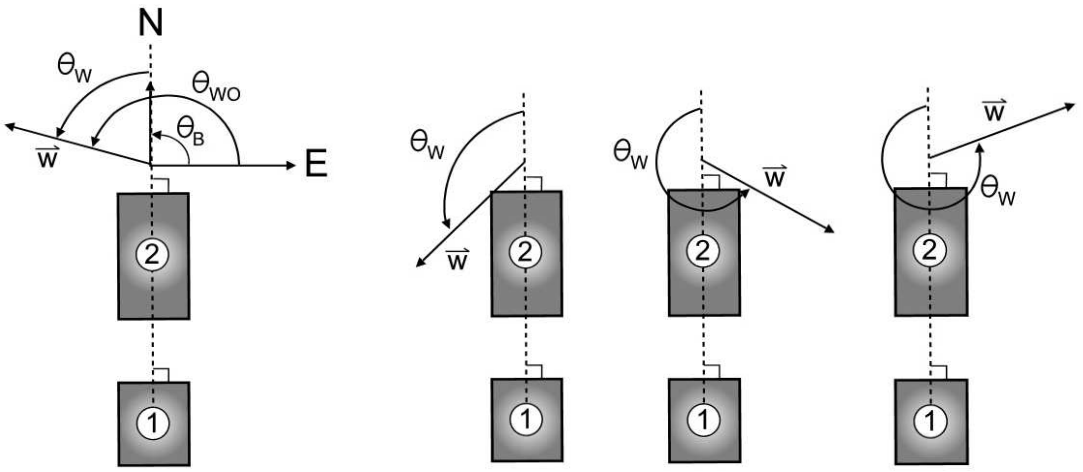

(a) $0° \leq \theta_W \leq 90°$ (b) $90° < \theta_W < 180°$ (c) $180° \leq \theta_W < 270°$ (d) $270° \leq \theta_W < 360°$

Figure 3.38: Illustration of the different ranges of θ_W for a canyon

Table 3.11: Matching Canyon CFD Simulations to Canyon Flows with Different Ranges of θ_W

θ_W **Range**	**Corresponding** $\theta_{W,CFD}$	**Flip Wind Data**	**Windward Building #**
$0° \leq \theta_W \leq 90°$	$\theta_{W,CFD} = \theta_W$	No	1
$90° < \theta_W < 180°$	$\theta_{W,CFD} = 180° - \theta_W$	Yes	2
$180° \leq \theta_W < 270°$	$\theta_{W,CFD} = \theta_W - 180°$	No	2
$270° \leq \theta_W < 360°$	$\theta_{W,CFD} = 360° - \theta_W$	Yes	1

3.5.1 Results of Canyon Simulations

Figure 3.40 is a vector plot representing the side view of the instantaneous velocity field of the flow inside the canyon for case 1a (described in Tables 3.8 and 3.9) taken at $t = 20$ s. There are two gradients of interest revealed in Figure 3.39. The first is encountered along the G_1 gradient line (aligned in the $+y_{CFD}$ axis direction) along which the wind velocity z-component (w_W) of the air rushing over the building top is changing (dw_W/dy). In the single building cases only a very weak gradient in this location was observed, however, for this canyon case the formation of a vortex inside the canyon helps to accentuate the gradient. The formation of a vortex in this particular flow is expected, since this canyon has $S/H = 1$ putting it in the skimming flow regime (Section 1.1.1). This vortex also sets up another w_W gradient along gradient line G_2 (dw_W/dy). If the aircraft is flying between the two buildings in the $+x_{CFD}$ direction through the recirculation zone and the wings are level with the gradient line G_2 then this gradient would exert a rolling moment on the aircraft.

Figures 3.40a - 3.40c provide a top view of the wind field for canyon case 1a at various altitudes. Figure 3.40a is taken at an altitude half that of the average building height. The most severe gradients occur as the gradient line G_1 (Figure 3.40a) is traversed along the $+x_{CFD}$ direction. At position 1 the streamwise wind velocity component v_W increases due to the acceleration of flow around the windward building before decreasing much more rapidly at position 2. A pair of vortices in the wake of the windward building cause reversed flow at position 3 creating another v_W velocity gradient (dv_W/dx). As positions 4 and 5 are passed, the gradients encountered are the opposite of the gradients encountered as positions 1 and 2 were passed; there is a large positive gradient at 4 as the low velocity region is exited and a

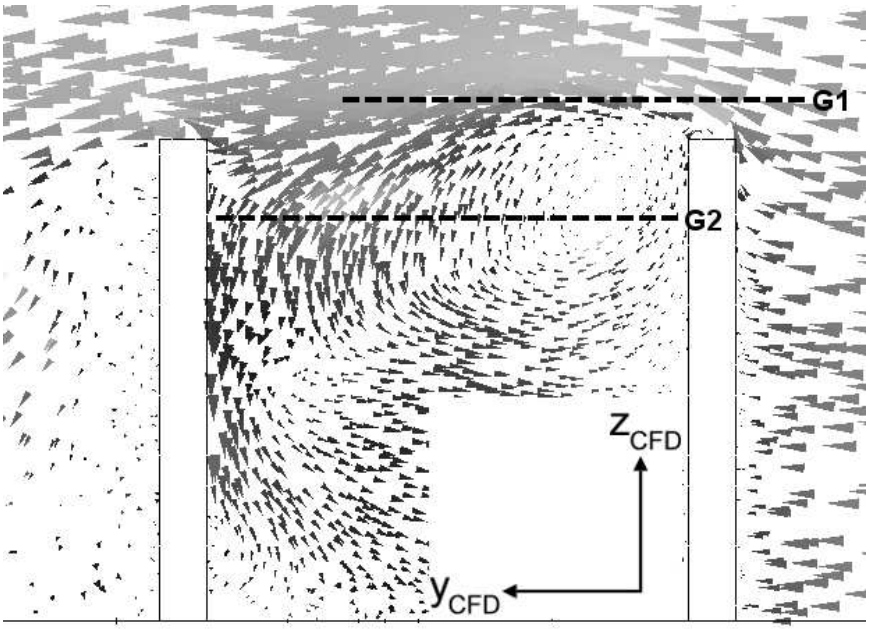

Figure 3.39: Side view of flow inside canyon, viewing plane passes through canyon centroid and is aligned with the wind (skimming flow, $S/H = 1$), $t = 20$ s

smaller negative gradient at 5 as the flow velocity decreases from the accelerated flow down to background conditions.

The observation of asymmetric flow in the region located just windward of the leeward building where the air flows across windward face in the $+x_{CFD}$ direction is specific to the simulation time at which the results are viewed ($t = 20$ s). When comparing the flow in and around the canyon between other simulation times, the strength and direction of this asymmetric flow pattern is found to be the main difference. It is more pronounced at $t = 20$ s than at other simulation times and, as such, provides the justification for using $t = 20$ s as the entry in the CWSD for this canyon case (since it would be worst-case for aircraft flight). This asymmetric flow region sets up a gradient of the x-component of the wind velocity (u_W) along G_2 (du_W/dy) and the asymmetry results in the flow curling around the leeward building and setting up a u_W gradient along the gradient line G_3 (du_W/dy). Finally, the strip of low velocity air behind the leeward building sets up v_W gradients along G_4, similar to the gradients at positions 2 and 4 along G_1. Figures 3.40b and 3.40c show a top view of the wind field at $z = 0.78H$ and $z = 0.98H$, respectively showing that the gradients from the $z = 0.5H$ example are significantly reduced and in some cases practically eliminated as the altitude increases,

indicating flow leakage over the building rooftops (analogous to wing-tip lift loss for aircraft).

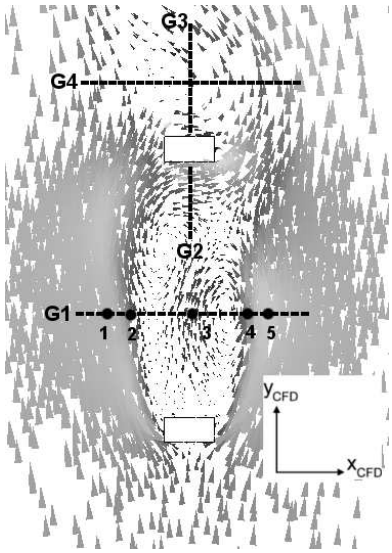

(a) Top view of flow around canyon, $z = 0.5H$

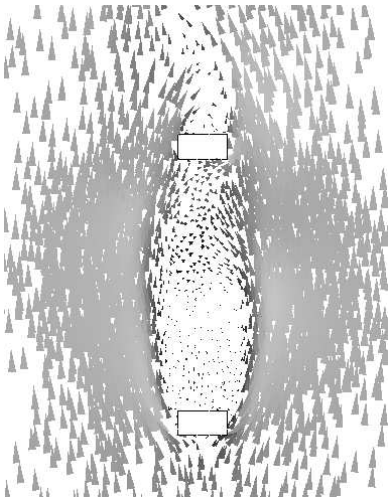

(b) Top view of flow around building, $z = 0.78H$

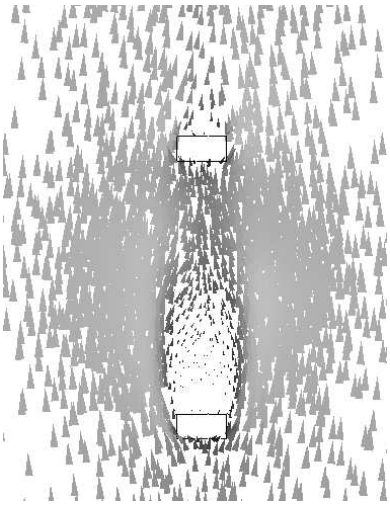

(c) Top view of flow around building, $z = 0.98H$

Figure 3.40: Vector plots of flow around case 1a canyon

Figures 3.41a and 3.41b are vector plots of the instantaneous velocity field at $t = 17$ s from case 1b (all CCS parameters are the same as for case 1a except for a larger background wind speed). The simulation time selected for this case is chosen in the manner as for case 1a (i.e. the strongest asymmetric flow just windward of the leeward building is observed for $t = 17$ s). Compared with case 1a, the velocity gradients for case 1b are stronger due to the higher background wind velocity. Figure 3.42a (case 2a) shows the resultant flow field ($t = 20$ s) when $\theta_W = 90°$ and S/H is very low (~ 0.1). This configuration creates two wakes which are both similar to single building wakes except that the flow between the buildings is significantly accelerated from the background wind velocity due to the venturi-like effect of the flow squeezing between the buildings. The flow results at other simulation times are very similar, however, the results at $t = 20$ s show slightly stronger recirculation zones. Figure 3.42b (case 3a) shows the resultant flow field ($t = 19$ s) when $\theta_W = 22.5°$ and $S/H = 2.25$ (wake-interference flow). It appears from the plot that there is negligible interference between the two single building wakes, partially due to the fact that the leeward building location is offset to the right of the windward building's wake since $\theta_W > 0°$. Similarly, for case 3b (same as case 3a but with a higher background wind velocity, the vector plot is very similar) negligible wake interference is observed. This suggests S/H ratios less than 2.25 are more relevant given the velocities and building scales used for these simulations and that cases such as 3a and 3b may be represented by two single building simulations.

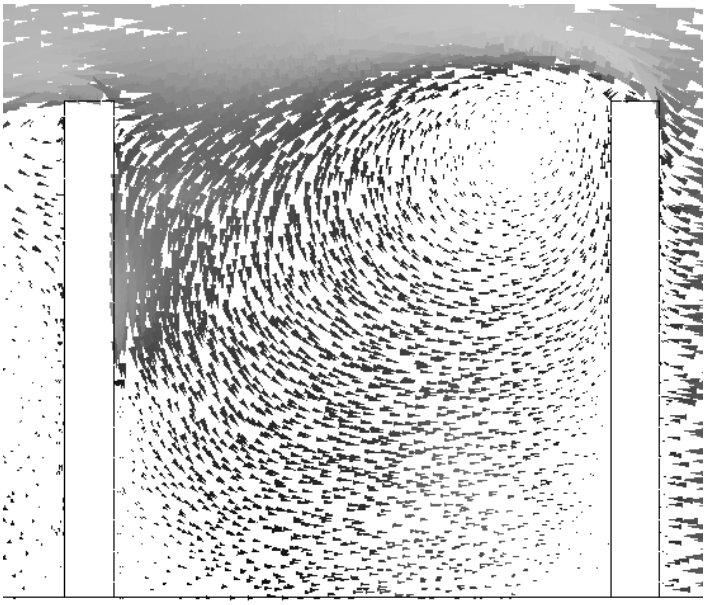

(a) Side view of flow inside canyon, viewing plane passes through canyon centroid and is aligned with the wind

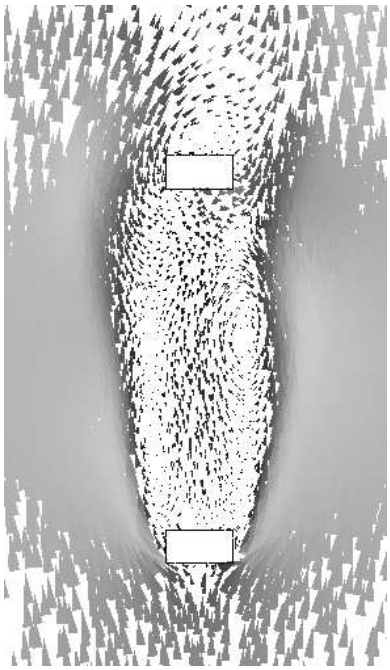

(b) Top view of flow around canyon, $z = 0.5H$

Figure 3.41: Vector plots of flow around case 1b canyon

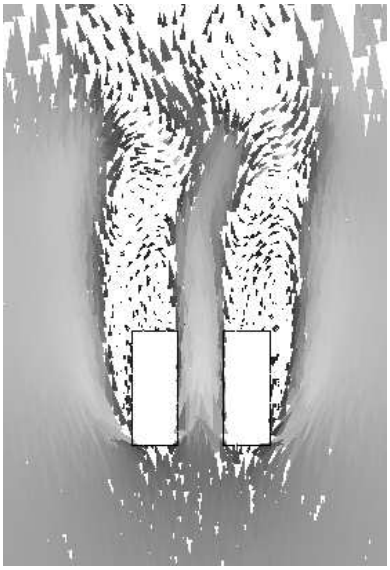

(a) Top view of flow around case 2a canyon, $z = 0.5H$

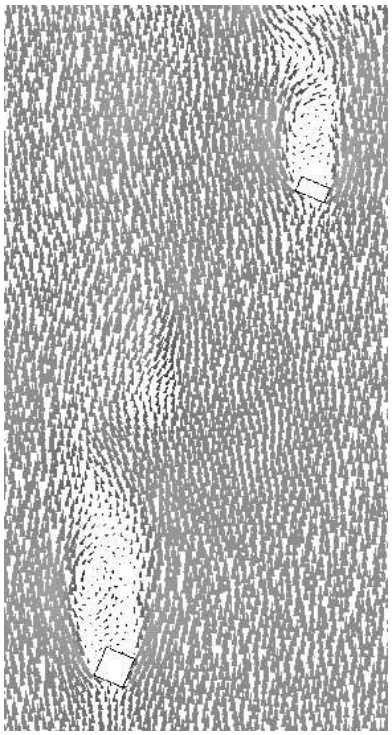

(b) Top view of flow around case 3a canyon, $z = 0.5H_{avg}$

Figure 3.42: Vector plots of flow around case 2a and case 3a canyons

Chapter 4

Simulation of the Aerosonde UAV in an Urban Environment

The simulation of aircraft flight in an urban wind environment is accomplished by modifying a pre-existing aircraft flight simulation model in such a way that it can use the aircraft position in a user-defined urban environment to determine aerodynamic forces and moments due to urban winds. A pre-existing model is obtained from Unmanned Dynamics Ltd. [62], who developed the AeroSim blockset for Matlab Simulink and have used this blockset to create the model shown in Figure 4.1. This is the base model that is modified in order to simulate flight in an urban wind environment. At the core of the Simulink model in Figure 4.1 is a dynamic model of the Aerosonde UAV (labeled 'Aerosonde UAV'). It is a non-linear six degree-of-freedom model which numerically integrates the rigid-body equations of motion in the body-frame and uses Euler-Rodrigues quaternions for attitude (aircraft orientation) determination. The aircraft parameters which define the Aerosonde flight characteristics (i.e. aerodynamics) are provided in a configuration file which is accessed by the dynamic model. From the dynamic model the outputs of various aircraft states (i.e. groundspeed and bank angle) are connected to view ports (to the right of the dynamic model in Figure 4.1) and the bank angle output is connected to a PI wing-leveler, the sole aircraft control that comes standard with the model. The output of the wing-leveler is input to the dynamic model as a control command together with other control commands and a constant wind vector (to the left of the dynamic model in Figure 4.1). To run the model, the numerical integration information (time step, integration

scheme) must be specified in addition to the aircraft's initial state (position, velocity, angular rates, etc.). Refer to the AeroSim Blockset User's Guide [62] for more specific details.

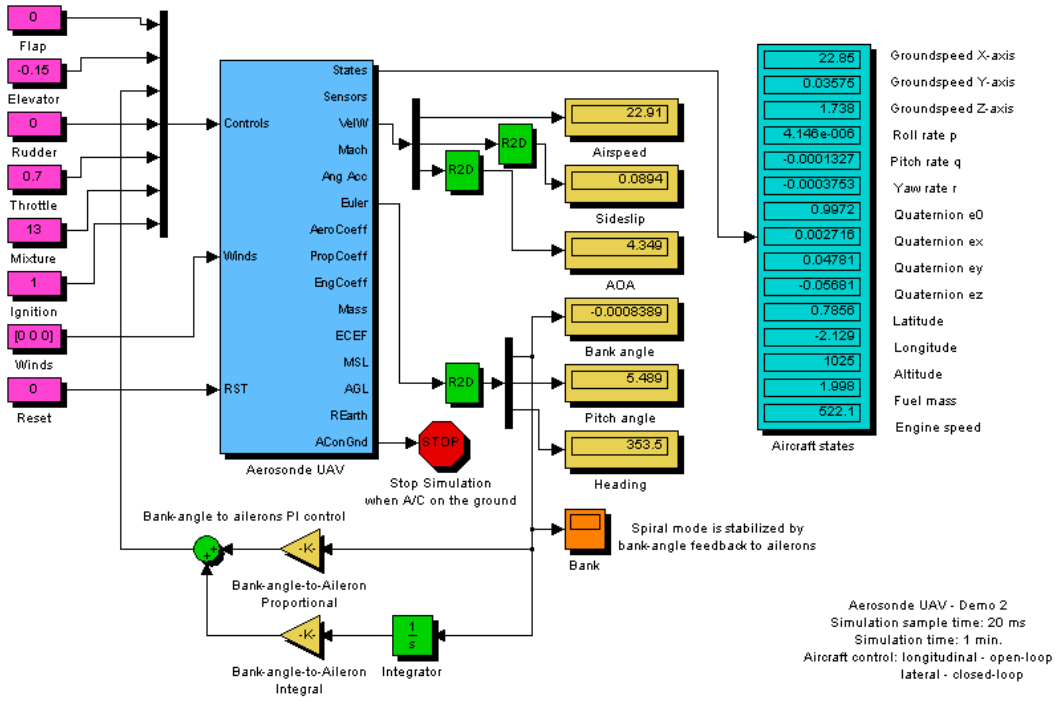

Figure 4.1: Overview of unmodified flight simulation model

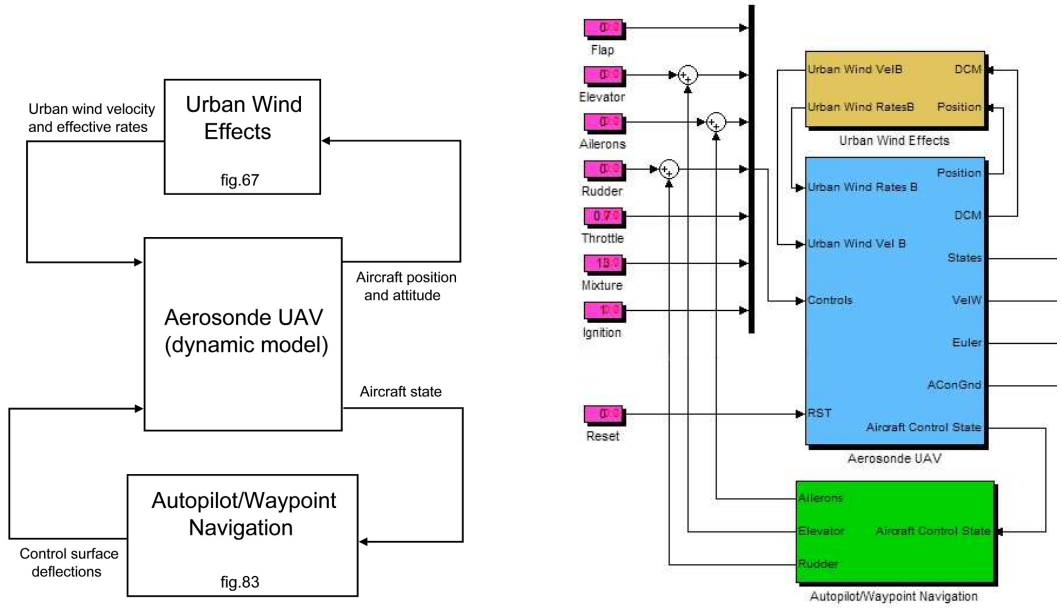

(a) Schematic view of modified flight simulation model

(b) Detailed view of modified flight simulation model

Figure 4.2: Top-level modifications necessary for including urban wind effects

Figures 4.2a and 4.2b illustrate the top-level modifications made to the model shown in Figure 4.1. Two subsystems are added: the Urban Wind Effects and Autopilot/Waypoint Navigation subsystems. The Urban Wind Effects subsystem accepts the current position and attitude of the aircraft, which are extracted from the dynamic model, and returns the wind velocity at the aircraft's CoG in the body frame ('Urban Wind VelB') and the 'effective rates' ('Urban Wind RatesB') due to urban wind in the body frame. These effective rates are used by the dynamic model to calculate the aerodynamic moments on the aircraft due to urban wind and are discussed in further detail in Section 4.4. The urban wind velocity at the aircraft's CoG is used by the dynamic model to calculate aerodynamic forces. The Autopilot/Waypoint navigation subsystem accepts the aircraft state vector (aircraft position and attitude) and implements a control routine which calculates control surface deflections in an effort to follow a list of waypoints while maintaining a constant altitude and track between each waypoint. The constant wind input originally provided with the model is not used since wind in an urban environment is dynamic.

Figures 4.3a and 4.3b provide a schematic and detailed overview, respectively, of the Urban Wind Effects subsystem. First, the aircraft position and the urban environment data (wind vector, building placement, etc. stored as constant values in the Urban Environment block) are passed to the Selection Algorithm function block which uses the aircraft's position in the urban environment together with the urban environment data and single building and canyon wake shape files (WSF) to select an entry in the WSD which represents the urban wind local to the aircraft. The position of the selected WSD entry in the single building or canyon DIF, the solution class (single building or canyon), urban environment data, aircraft position and attitude are then passed to the Wind Field Analysis function block. This block uses the provided inputs to access the SCF and CFD results file corresponding to the selected WSD entry and analyze the wind field local to the aircraft to obtain the wind velocity at the aircraft's CoG and effective rates (which requires the wind gradients along the aircraft wing and fuselage). This analysis is passed back to the dynamic model which makes use of this information to calculate the aerodynamic forces and moments on the aircraft and the new aircraft position and attitude at the next time step.

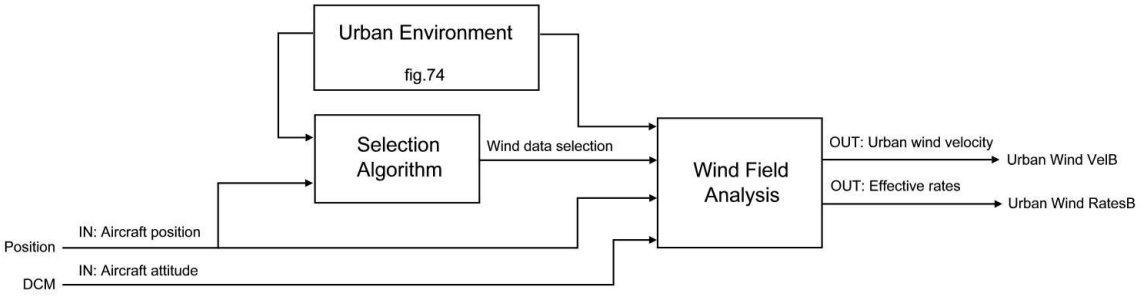

(a) Schematic overview of Urban Wind Effects subsystem

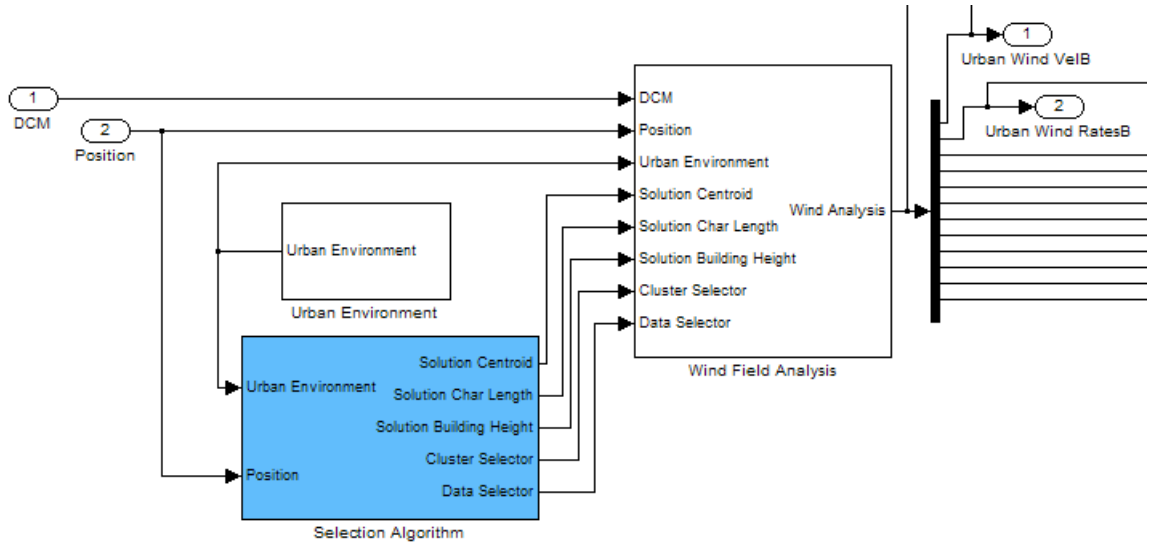

(b) Detailed overview of Urban Wind Effects subsystem

Figure 4.3: Schematic and detailed overview of Urban Wind Effects subsystem

Figures 4.4a and 4.4b illustrate the extraction of aircraft position ('Position') and attitude ('DCM'), respectively, from the Aerosonde UAV dynamic model (Figure 4.2). Position and attitude are outputs from the Equations of Motion subsystem, which is in turn a subsystem of the dynamic model, and highlighted lines show the extraction pathways of the aircraft position and attitude which eventually connect to the Position and DCM outputs of the dynamic model, respectively. Aircraft attitude is represented by the Direction Cosine Matrix (DCM), described by the AeroSim Blockset User's Guide [62] as the matrix by which a vector in the AeroSim inertial frame is transformed to the aircraft body frame. The AeroSim inertial frame is defined as the North-East-Down (NED) frame, defined by the coordinates $(x_N, x_E, x_D)^T$. Euler angles are an intuitive way to describe aircraft attitude and the user's guide defines the DCM as

$$DCM = \begin{pmatrix} C_\theta C_\psi & C_\theta S_\psi & -S_\theta \\ S_\phi S_\theta C_\psi - C_\phi S_\psi & S_\phi S_\theta S_\psi + C_\phi C_\psi & S_\phi C_\theta \\ C_\phi S_\theta C_\psi + S_\phi S_\psi & C_\phi S_\theta S_\psi - S_\phi C_\psi & C_\phi C_\theta \end{pmatrix} \tag{4.1}$$

where ϕ, θ, and ψ are the roll, pitch and yaw Euler angles, respectively.

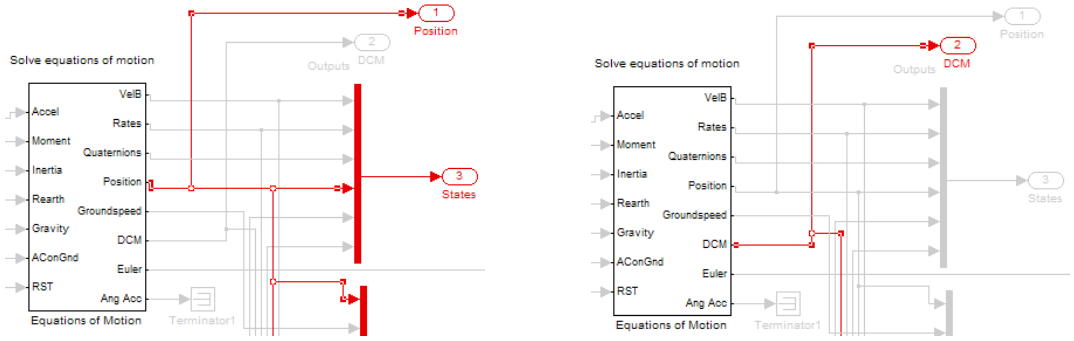

(a) Extraction of aircraft position ('Position')

(b) Extraction of aircraft attitude ('DCM')

Figure 4.4: Extraction of aircraft position ('Position') and attitude ('DCM') from the 'Equations of Motion' block in the Aerosonde UAV dynamic model (Figure 4.2)

Recall that effective wind rates ('Urban Wind Rates B') and wind velocity ('Urban Wind Vel B') are outputs from the Urban Wind Effects subsystem and inputs to the Aerosonde UAV dynamic model (Figure 4.2). Figures 4.5 and 4.6 illustrate the insertion of effective wind rates and wind velocity to their appropriate locations inside the dynamic model. The first insertion point for the effective wind rates and wind velocity is to the Aerodynamics subsystem inside the dynamic model, as illustrated by Figures 4.5a and 4.6a respectively. The second and final insertion points for the rates and velocity are the summation blocks inside the Aerodynamics block as shown in Figures 4.5b and 4.6b, respectively.

In the Aerodynamics block the effective rates 'Urban Wind Rates B' are added to the aircraft's angular rates 'Rates' (in body frame coordinates). The 'WindRates' input, which is part of the original model, is neglected by using a zero-gain for two reasons. First, in the unmodified dynamic model this input represents the effective rates due to the background

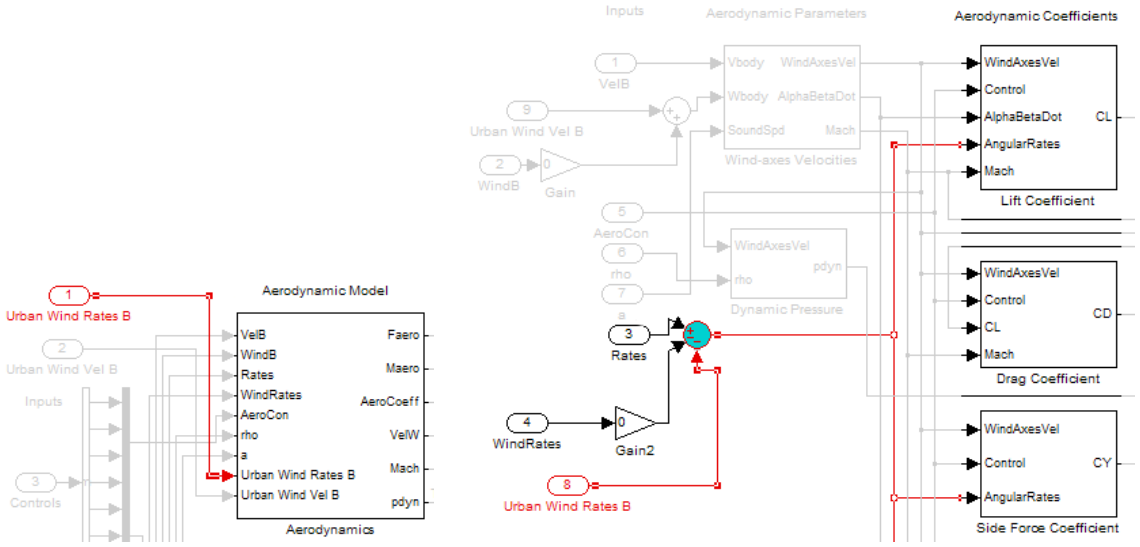

(a) First insertion point of effective wind rates

(b) Second insertion point of effective wind rates

Figure 4.5: Insertion of effective wind rates ('Urban Wind Rates B') into the Aerodynamics block inside the Aerosonde UAV dynamic model (Figure 4.2)

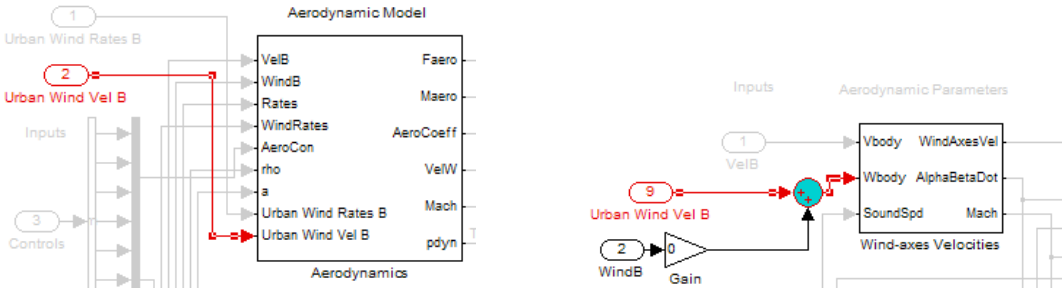

(a) First insertion point of wind velocity

(b) Second insertion point of wind velocity

Figure 4.6: Insertion of wind velocity ('Urban Wind Vel B') into the Aerodynamics block inside the Aerosonde UAV dynamic model (Figure 4.2)

atmospheric turbulence generated by von Karman shaping filters (independent of the effects of buildings on atmospheric wind). However, the only turbulence considered in this work is that due to the presence of buildings. Secondly, the method by which these rates are calculated is not the method chosen for this research (the method used is the four point model from Etkin [66], the implementation of which is discussed later in Section 4.4). The 'WindRates' rates are calculated by the dynamic model in way which only requires the relative wind velocity at the aircraft CoG at each time step, and there are a few problems with this. Instead of considering the spacial variation of relative wind over the aircraft dimensions at each time step (as is the case for the four point model), the method used by the unmodified dynamic

model approximates the spacial variation of relative wind by using a numerical time derivative (involving the current and previous simulation times) of the relative velocities at the aircraft CoG and the aircraft forward speed (the component of inertial aircraft speed aligned with the fuselage). As such, only an effective pitch and yaw rate can be calculated (i.e. effective roll is ignored), as stated specifically in the AeroSim Blockset User's Guide [62]. Additionally, this method becomes less accurate as the aircraft angular rates increase (for example when the aircraft is pitching rapidly) and the numerical derivative utilized by this method is sensitive to sharp fluctuations in the flow field (which may arise due to numerical effects). The wind velocity at the aircraft's CoG ('Urban Wind Vel B') is added to the 'WindB' input (standard with the original model), which is neglected with a zero-gain since it also represents wind due to the background atmospheric turbulence generated by the von Karman shaping filters.

Before running a simulation of aircraft flight, the initial aircraft state must be specified as directed in the AeroSim Blockset User's Guide [62]. The specification of the initial aircraft state variables are fairly straightforward except for initial aircraft velocity and attitude. Initial velocity is specified in terms of the aircraft's body-fixed coordinate system but the guide does not explicitly specify what attitude and velocity would correspond to, for example, an initial Northerly velocity. Since the urban wind environment uses a East-North-Up (ENU) frame, this information is important to ensure the aircraft has the desired initial heading. Recalling the DCM takes a vector in the NED frame to the body frame,

$$\begin{pmatrix} x_b \\ y_b \\ w_b \end{pmatrix}_{body} = DCM \cdot \begin{pmatrix} x_N \\ x_E \\ x_D \end{pmatrix}_{NED} \tag{4.2}$$

this provides a way to calculate the body-frame velocities knowing the desired initial NED-frame velocities (provided that the DCM is known). In addition, it is a property of the DCM that $DCM^{-1} = DCM^T$ giving

$$\begin{pmatrix} x_N \\ x_E \\ x_D \end{pmatrix}_{NED} = DCM^T \cdot \begin{pmatrix} x_b \\ y_b \\ w_b \end{pmatrix}_{body} \tag{4.3}$$

and thus providing a way to calculate NED frame vectors given the initial body frame vectors (an operation required during execution of the Wind Field Analysis function). The definition of the DCM in Equation 4.1 is in terms of Euler angles so choosing a set of initial Euler angles is sufficient for calculating initial attitude, however, the dynamic model requires the definition of initial attitude in terms of quaternions. Attitude definition in terms of quaternions is not as intuitive as Euler angles, but the user's guide provides the following conversion from Euler angles to quaternions:

$$\begin{pmatrix} e_0 \\ e_x \\ e_y \\ e_z \end{pmatrix} = \begin{pmatrix} C_{\phi/2}C_{\theta/2}C_{\psi/2} + S_{\phi/2}S_{\theta/2}S_{\psi/2} \\ S_{\phi/2}C_{\theta/2}C_{\psi/2} + C_{\phi/2}S_{\theta/2}S_{\psi/2} \\ C_{\phi/2}S_{\theta/2}C_{\psi/2} + S_{\phi/2}C_{\theta/2}S_{\psi/2} \\ C_{\phi/2}C_{\theta/2}S_{\psi/2} + S_{\phi/2}S_{\theta/2}C_{\psi/2} \end{pmatrix} \tag{4.4}$$

For example, the simplest aircraft attitude $(\phi, \theta, \psi) = (0, 0, 0)$ corresponds to the quaternion $(e_0, e_x, e_y, e_z) = (1, 0, 0, 0)$ which also co-incides with a $DCM = I$, the identity matrix (i.e., the body axes and NED axes coincide). At this attitude the North-axis represents the x_b axis and the East and Down axes represent the y_b and z_b axes, respectively. This determines the relative orientation of the body axes with respect to the inertial NED frame, so all that needs to be done is to fix these body axes to an aircraft as shown in Figure 4.7. These body axes are used to define the aerodynamic force and moment conventions.

The following sections describe the Selection Algorithm, Wind Field Analysis (both in the Urban Wind Effects subsystem, Figures 4.2 and 4.3), and Autopilot/Waypoint Navigation (Figure 4.2) subsystems in greater detail. These descriptions will require the use of various reference frames as summarized in Figure 4.8. The Autopilot/Waypoint Navigation subsystem

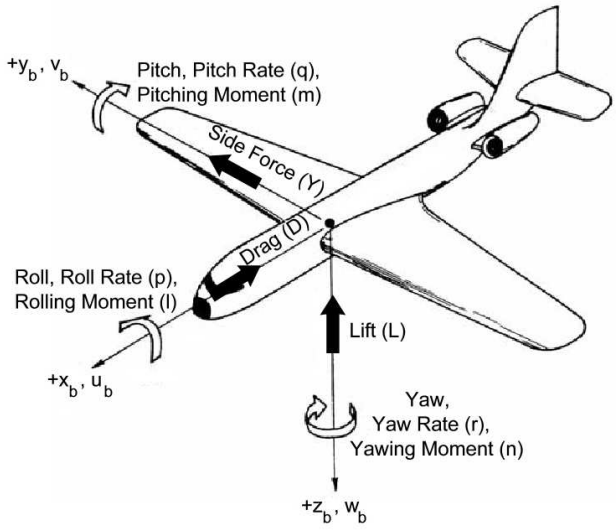

Figure 4.7: Aircraft axes, forces and moments convention [63]

is separate from the Selection Algorithm and Wind Field Analysis subsystems, so further discussion of the reference frame specific to this subsystem (Track Aligned frame) will be deferred to Section 4.5. The NED frame (Figure 4.8a) is the inertial frame used internally by the dynamic model and is the frame in which a vector must be placed before it can be taken to the body frame using Equation 4.2. The ENU frame (Figure 4.8b) is the inertial frame in which the urban environment is specified. Both the NED and ENU frames are used within all three Selection Algorithm, Wind Field Analysis, and Autopilot/Waypoint Navigation subsystems. The NED and ENU frames (Figures 4.8a and 4.8b) are the same except that the x and y axes are switched and the z axis is of opposite sign. The Wind-Centroid-Height (WCH) frame (Figure 4.8c) has its y axis aligned with the background wind vector and the origin placed at the single building or canyon centroid at rooftop height, and is therefore used to determine the position of the aircraft relative to the rooftop height and centroid of a given single building or canyon (recall rooftop height for a canyon is the average height of the two buildings). As such it is used by the Selection Algorithm subsystem to determine whether the aircraft is in the wake of a given single building or canyon, and by the Wind Field Analysis subsystem as an intermediate step in determining the locations in a CFD simulation which correspond to desired locations on the aircraft (e.g. aircraft CoG) at which wind data is extracted in the form of wind velocity vectors. For a given single building or canyon, the WCH frame

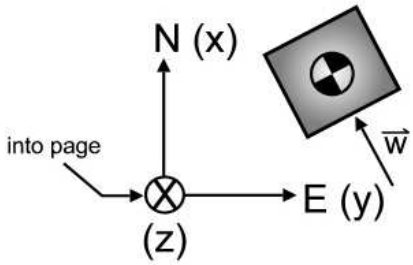

(a) North-East-Down (NED) frame, inertial frame used by dynamic model

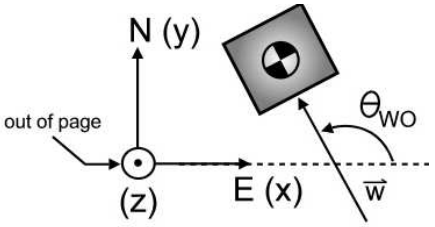

(b) East-North-Up (ENU) frame, inertial frame used to describe the urban environment

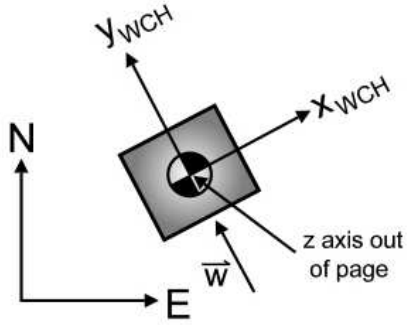

(c) Wind-Centroid-Height (WCH) frame, used to determine if the aircraft is contained in the single building or canyon wake and as an intermediate step in calculating a location in the CFD frame from an inertial frame (NED or ENU). Origin of frame is on the centroid and at rooftop height.

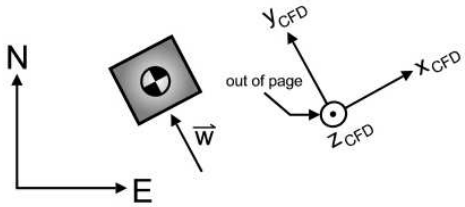

(d) CFD frame, frame in which the flow field results in the wind database are stored

Figure 4.8: Various reference frames

is obtained from the ENU frame by first subtracting the single building or canyon rooftop height from the ENU altitude and then translating and rotating (by $\theta_{WO} - 90°$) the ENU frame so as to align the y axis with the wind and to match the x-y origin coordinates with the centroid x-y coordinates. The CFD frame (Figure 4.8d) is the coordinate frame used by CFD simulations, and it differs from the WCH frame in that the z axis origin is at ground level and the unit-scale and x-y origin of the coordinates are not necessarily the same. The CFD frame coordinate scale and x-y origin for a given CFD simulation are obtained from the Simulation Configuration File (SCF). The body frame (not included in Figure 4.8, but shown in Figure 4.7) is the frame in which initial aircraft velocity is specified and in which the dynamic model calculates aerodynamic forces and moments due to urban wind. This requires that, inside the Wind Field Analysis subsystem, the wind velocities (wind data) extracted from the CFD

simulation are to be represented in the body frame so that the wind velocity at the CoG ('Urban Wind VelB', Figure 4.2a) and effective rates ('Urban Wind RatesB', Figure 4.2a) are in the body frame.

4.1 Geodetic Spherical to Cartesian Coordinate Transformation

The dynamic model tracks aircraft position using latitude, longitude, and altitude coordinates (geodetic spherical). However, the Urban Wind Effects and Autopilot/Waypoint Navigation subsystems (Figure 4.2) are designed to use Cartesian coordinates in the NED, ENU, WCH and CFD frames. To resolve this, the geodetic spherical coordinates are converted to a locally level coordinate system, where the z axis is outward normal to the Earth's surface and the x and y axes are tangent to the Earth's surface at the origin (Figure 4.9). To simplify this conversion it is first assumed that the dimensions of a typical urban area are small enough compared to the Earth's equatorial length that the local radius of curvature of the Earth's surface can be neglected. Therefore the altitude and z coordinates can be equated. To relate the x and y coordinates to longitude and latitude, it is important to note that as the equator is approached, the closer the local latitude and longitude lines approximate a Cartesian x-y system. For this reason, the origin of the urban environment of interest is always defined to be $[Lat_o\ Long_o]$ = $[0^\circ\ 10^\circ]$ (since there is no divergence of longitudinal lines at $Lat = 0^\circ$). It is assumed that the atmospheric effects specific to flying at such a latitude and longitude are negligible for the purposes of this research. The choice for $Long_o$ is somewhat arbitrary, as long as it is at a distance from the 0° and 180° longitude lines greater than the longitudinal distance traveled by the aircraft during a mission ($10^\circ > 1000km$). This is required since it seems to appear that the AeroSim dynamic model treats constant latitude movement Westwardly or Easterly from 0° or 180° longitude as the same numerical change in longitude (i.e. either Westerly or Easterly motion is represented by, for example, a 30° change in longitude). Similarly, it seems that no numerical distinction is made between constant longitudinal Northerly or Southerly motion from the equator. To resolve this, the simulations of flight in an urban wind environment are setup such that the aircraft is always flying North of the urban environment's origin.

These assumptions and conventions allow for a conversion between the geodetic spherical ($[Lat\ Long\ Alt]$) and ENU ($[x_E\ x_N\ x_U]$) systems. Letting the length of Earth's equator (L_{Eq}) and Earth's meridian (L_M) be $L_{Eq} = 40075$ km and $L_M = 40008$ km, respectively [64], the conversion is:

$$x = (Long - Long_o) * L_{Eq}/360 \tag{4.5a}$$

$$y = (Lat - Lat_o) * L_M/360 \tag{4.5b}$$

$$z = Alt \tag{4.5c}$$

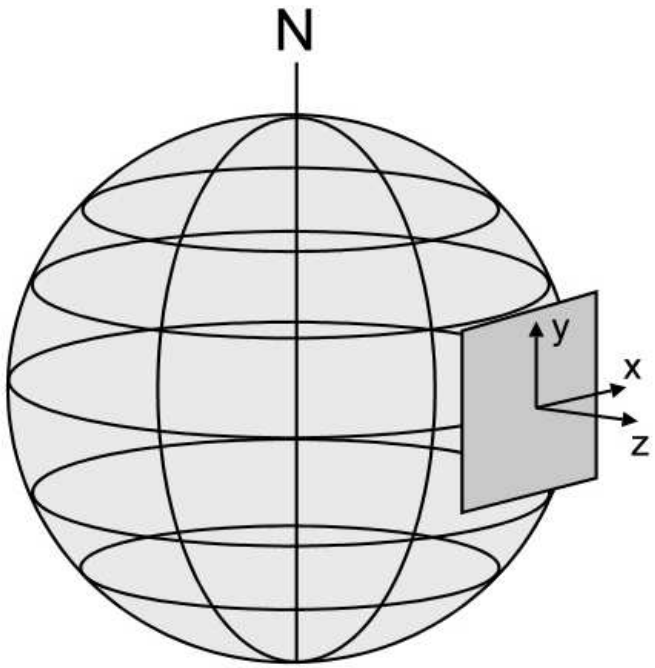

Figure 4.9: Geodetic spherical to Cartesian coordinates

4.2 Selection Algorithm subsystem

The overall purpose of the Selection Algorithm subsystem (in the Urban Wind Effects subsystem, Figure 4.3) is to take an aircraft location in a first generation urban environment and determine which, if any, entry from the WSD can be used to represent the local flow field.

In doing so, the algorithm must be able to determine if a given single building or canyon significantly influences the flow local to the aircraft. The flow local to the aircraft is considered significantly influenced by a single building or canyon if it is inside the wake of the single building or canyon. Figure 4.11 provides an overview of the algorithm, which consists of 4 logic blocks together with a loop.

1. The algorithm first executes logic block 1 which gathers environmental data (the information required to define a first generation urban environment, see Section 2.3). As shown in Figure 4.10, the values for each parameter defining the urban environment (except aircraft position) are stored as constant values inside the Urban Environment Data block, found in the Urban Wind Effects subsystem (Figure 4.3). The parameters n_{wake}, i, and j are initialized to 0, 1, and 2, respectively. The parameter n_{wake} is used to store the number of wakes which are found to contain the aircraft. The parameters i and j are used to keep track of which single building or canyon wakes are being investigated for the purpose of determining whether they contain the aircraft, as each building specified in the first generation urban environment is assigned a unique number.

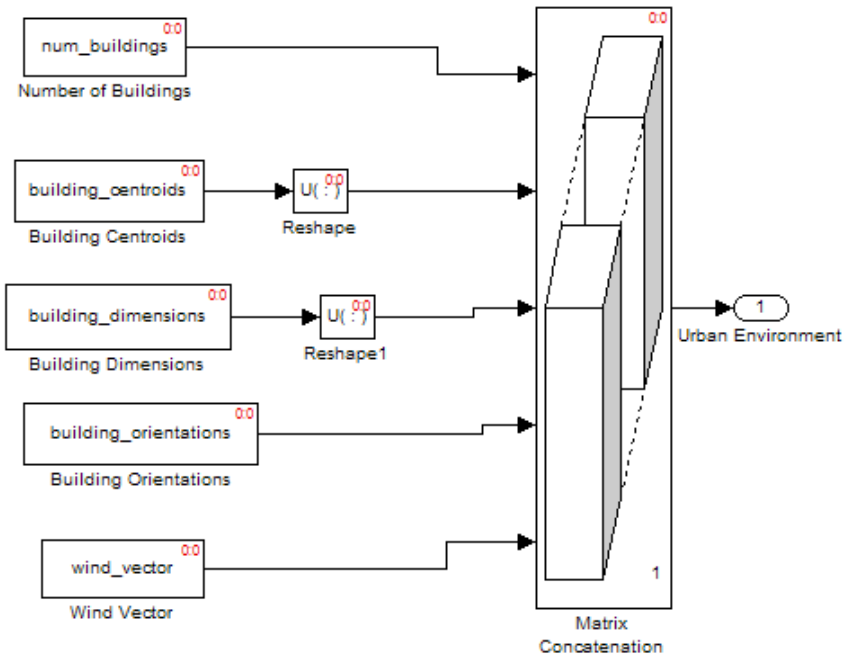

Figure 4.10: Inside Environmental Data block

2. Next, starting with $i = 1$ and $j = 2$, logic block 2 is entered into and a canyon is formed by pairing building 1 ($i = 1$) with building 2 ($j = 2$). From the canyon geometry and the background wind conditions, the canyon wind simulation database (CWSD) is searched to see whether there is an entry which represents the airflow around the canyon (i.e. if there is an available wake). If there is an available wake, buildings 1 and 2 are each marked separately as 'checked' and it is determined whether the aircraft lies within the wake or not. If the wake contains the aircraft then n_{wake} is increased by 1 and the class (single building or canyon) and position in the Database Index File (DIF) of the CFD simulation corresponding to the wake is stored. The loop continues with the procedure discussed above, increasing j by 1 each iteration until $j = n_B$, where n_B is the total number of buildings in the urban environment.

3. When j reaches n_B, logic block 3 is entered. The purpose of this block is to determine whether building 1 (considered as a single building) contains the aircraft in its wake, provided building 1 hasn't been marked as checked (which would indicate the aircraft has been found to lie within the wake of a canyon formed from building 1 and some other building). If it has not been checked, the same method as for a canyon is used to determine whether there is a wake available for building 1. If there is none available, this indicates that not enough single building CFD simulations have been done to populate the WSD and the algorithm returns 'NO SOLUTION' since it cannot be determined if building 1 significantly influences the flow local to the aircraft. The 'NO SOLUTION' result terminates the Selection Algorithm and the current flight simulation. If a wake is available, the same method as for a canyon wake is used to determine whether the wake contains the aircraft. In the case where the wake contains the aircraft, n_{wake} is increased by 1. At this point i is increased by 1 and it is checked whether $i \geq n_B$. If it is not, j is set to $j = i + 1 = 3$ (since $i = 2, j = 1$ has already been considered as canyon and $i = 2, j = 2$ does not represent a canyon) and the canyon checking starts again with $i = 2, j = 3$. After logic block 3 executes for $i = n_B$ the resulting movement to $i = n_B + 1$ will cause the algorithm to begin logic block 4.

4. This block (logic block 4) determines the output of the algorithm based on the value of

n_{wake}. A value of 0 means no wakes were found to contain the aircraft, and therefore the solution is the background wind. A value greater than 1 means the aircraft was found to lie within more than one wake and therefore there is no unique flow field solution from the WSD (hence the 'NO SOLUTION' result). This would imply a scenario such as the aircraft being in a flowfield influenced by both a canyon and a single building not contained in the canyon, and thus a more sophisticated CFD simulation would be required (in this case, a three-building simulation) to represent the resulting flowfield (i.e. this would lead to more advanced generations of the WSD). If $n_{wake} = 1$, the aircraft is in a unique flow field and the corresponding CFD simulation from the database is selected. There are five variables output from the Selection Algorithm describing the outcome (see Figure 4.3 at the beginning of this chapter). If $n_{wake} = 0$ then Cluster Selector is set equal to zero, which tells the Wind Field Analysis function that the aircraft is surrounded by the background wind field. If $n_{wake} = 1$ then Cluster Selector can take on one of two values; if the aircraft is in a single building wake then Cluster Selector is set to a value of 1 and if the aircraft is in a canyon wake Cluster Selector is set to a value of 2. If $n_{wake} > 1$ then Cluster Selector is set equal to 3, which tells the simulation to stop (Cluster Selector is similarly set when the 'NO SOLUTION' result is obtained in logic block 3). The value for Data Selector also depends on n_{wake}. If $n_{wake} = 1$ then Data Selector is set to the number of the entry in the single building or canyon DIF corresponding to the wake in which the aircraft was found. In addition, the height, characteristic length D, and centroid location in the urban environment of the single building or canyon responsible for the flow local to the aircraft are stored as the variables Solution Building Height, Solution Char Length, and Solution Centroid, respectively. If If $n_{wake} \neq 1$ then Data Selector, Solution Building Height, Solution Char Length, and Solution Centroid are all set to zero.

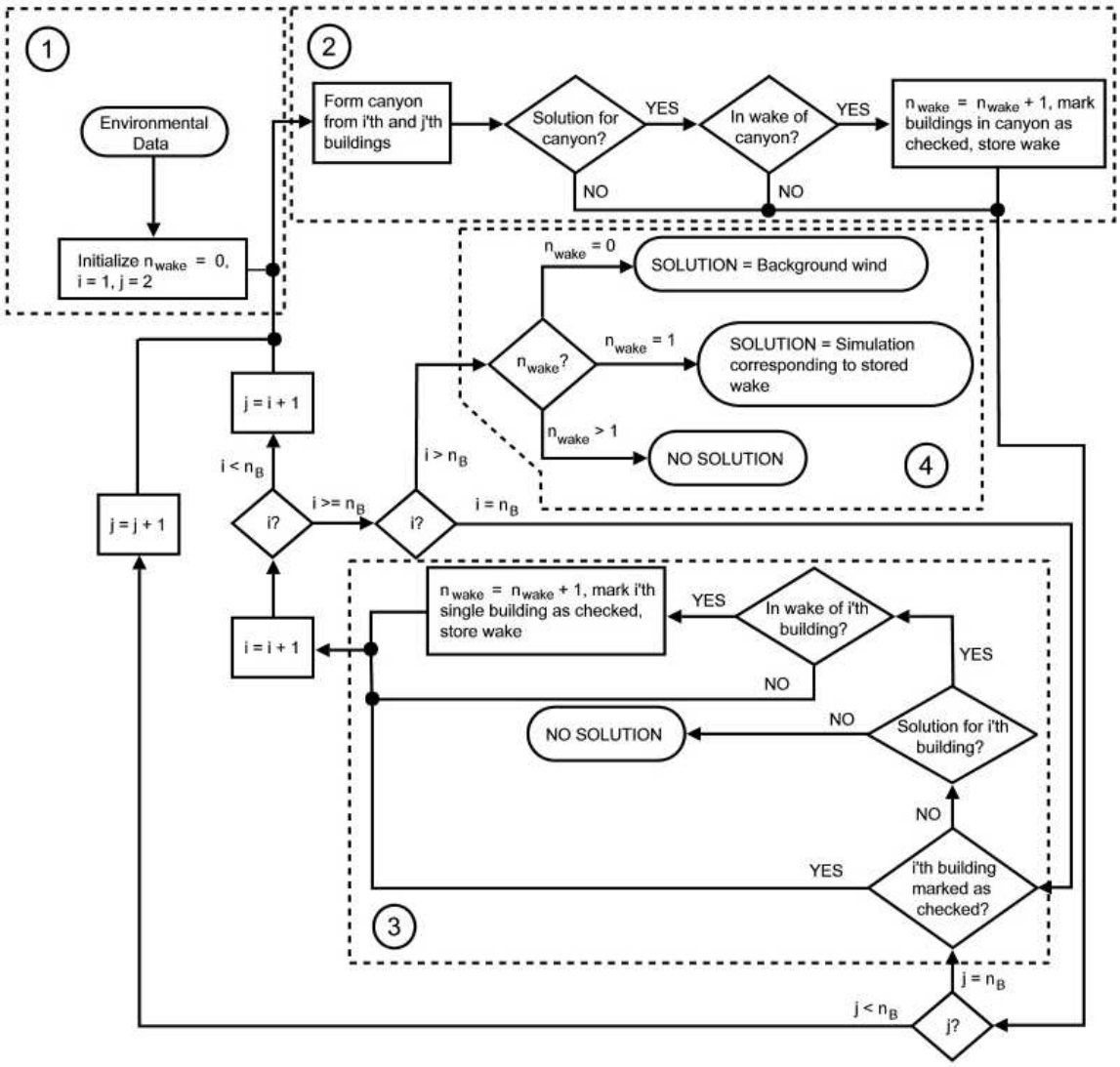

Figure 4.11: Overview of selection algorithm

4.3 Implementation of Selection Algorithm subsystem - Accessing Wake Shape and Determination of Aircraft Containment in Wake

The first step in determining whether the aircraft is in the wake of a given single building or canyon in a specified background wind field is to obtain the wake shape data (in the form of the appropriate wake shape file, WSF) for the given single building or canyon flow. To find

the appropriate WSF, the corresponding position of the single building or canyon flow in the single building or canyon database index file (DIF) needs to be found which in turn requires the position of the single building or canyon flow in the single building or canyon configuration space. The urban environmental data provides all the necessary information (building geometry, background wind vector) to determine the position of the flow in configuration space (e.g. wind incidence, Re, L/W).

With the point in configuration space determined, an attempt is made to match it with an entry in the single building or canyon DIF within set tolerances. Assuming a match is found, the wake shape information is determined from the WSF file corresponding to the matching entry in the single building or canyon DIF. For example, a given canyon flow with a matching entry in the canyon DIF at position 2 would have the WSF name `canyon2wakeshape.txt` as per the conventions laid out in Section 3.3.

Multiplying all spline control points by the characteristic length D of the single building or canyon under investigation, these control points can then be used to create three spline functions: the left, right and top wake boundaries. The storage of wake shape information and creation of splines was discussed in Sections 3.4.3 and 3.5.1. Figures 4.12a-4.12d illustrate the remaining steps. Initially the coordinates describing aircraft location are in the geodetic spherical frame but need to be obtained in the Wind-Centroid-Height (WCH) frame so that the aircraft can be located with respect to the single building or canyon wake boundaries. Equations 4.5a-4.5c in section 4.1 take the aircraft position to the ENU frame from the geodetic spherical frame (Figure 4.12a). To obtain the aircraft coordinates in the WCH frame (Figure 4.12b), the relative position vector $\overrightarrow{p}_{A/C \leftrightarrow Building,ENU}$ between the aircraft and single building or canyon centroid in the ENU frame as shown in Figure 4.12a (calculated as $\overrightarrow{p}_{A/C,ENU} - \overrightarrow{p}_{Building,ENU}$) must first be rotated by the angle $-\theta_{WA}$ about the z axis. The angle θ_{WA} is the wind alignment angle, and it is the angle (positive counter-clockwise) between the background wind vector and the North axis. Such a rotation is accomplished by the rotation matrix

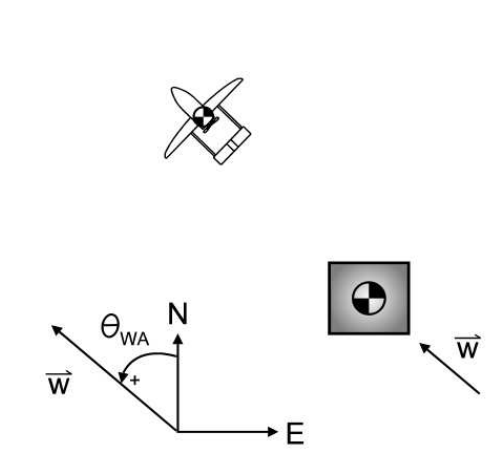

(a) Aircraft and single building in ENU frame

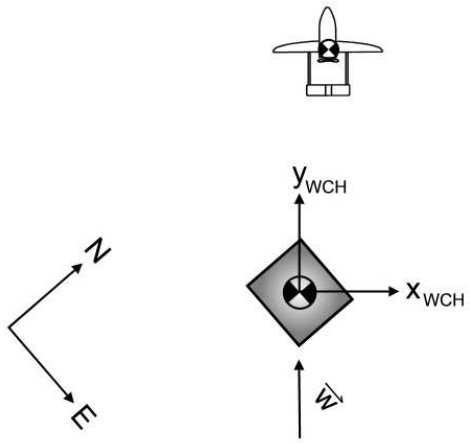

(b) Aircraft and single building in wind-centroid frame

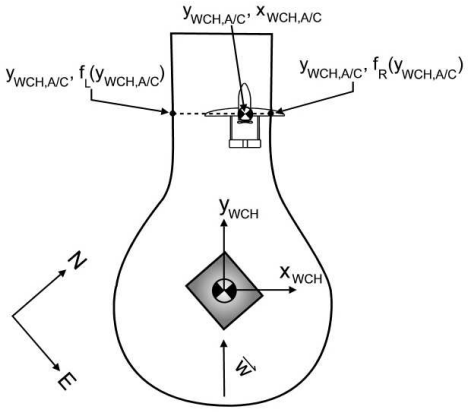

(c) Determine whether aircraft is in between left and right wake boundaries f_L and f_R

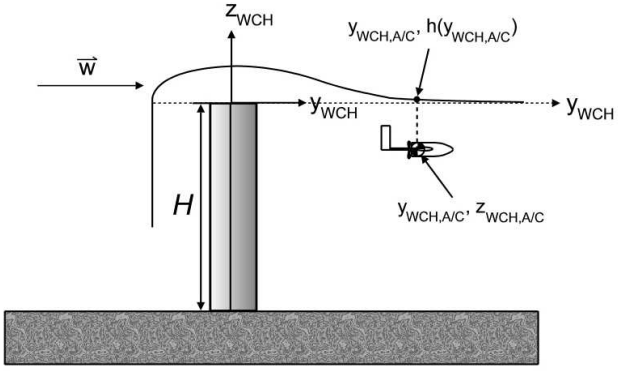

(d) Determine whether aircraft is below wake height boundary h

Figure 4.12: Determination of aircraft containment in wake. A single building is shown, however the same procedure applies for a canyon where, essentially, instead of a building centroid the canyon centroid is used.

$$R(-\theta_{WA}) = \begin{pmatrix} C_{-\theta_{WA}} & -S_{-\theta_{WA}} & 0 \\ S_{-\theta_{WA}} & C_{-\theta_{WA}} & 0 \\ 0 & 0 & 1 \end{pmatrix} = \begin{pmatrix} C_{\theta_{WA}} & S_{\theta_{WA}} & 0 \\ -S_{\theta_{WA}} & C_{\theta_{WA}} & 0 \\ 0 & 0 & 1 \end{pmatrix} \tag{4.6}$$

Next, the aircraft height in the WCH frame is calculated by subtracting the single building or canyon height vector $(0, 0, H)^T$ from the aircraft altitude in the ENU frame. Therefore the aircraft position in the WCH frame ($\vec{p}_{A/C,WCH}$) is calculated using the equation

$$\begin{aligned} \vec{p}_{A/C,WCH} &= R(-\theta_{WA}) \cdot \left[\vec{p}_{A/C,ENU} - \vec{p}_{Building,ENU}\right] - (0, 0, H) \\ &= \left(x_{A/C,WCH}, y_{A/C,WCH}, z_{A/C,WCH}\right) \end{aligned} \tag{4.7}$$

As discussed in Section 3.4.3, the left, right and top wake shape functions are defined in the WCH frame where the x_{WCH} coordinate for the left and right wake shape functions and the z_{WCH} coordinate for the wake height function are both functions of y_{WCH}, as shown in Figures 4.12c and 4.12d. Since the x_{WCH}, y_{WCH}, and z_{WCH} coordinates of the aircraft are also known, all that needs to be done is to determine whether the following conditions are met: (1) the aircraft y_{WCH} coordinate ($y_{A/C,WCH}$) is in the range of the y_{WCH} coordinates describing the wake shape (2), the aircraft x_{WCH} coordinate is in between the x_{WCH} coordinates of the left and right wake shape functions evaluated at $y_{A/C,WCH}$, (3) the the aircraft z_{WCH} coordinate is less than the z_{WCH} coordinate of the wake height function evaluated at $y_{A/C,WCH}$.

4.4 Wind Field Analysis

The overall purpose of the Wind Field Analysis subsystem, assuming that the 'NO SOLUTION' option has not been triggered during the execution of the Selection Algorithm (Figure 4.11), is to use the results of the Selection Algorithm (i.e. which entry in the WSD, if not the background wind vector, can be used to represent the flowfield surrounding the aircraft) to obtain the appropriate wind data and calculate, in the body frame, the wind velocity at the aircraft CoG and the effective rates so that the dynamic model can calculate the aerodynamic forces and

moments through which urban winds affect aircraft flight. The calculation of aerodynamic forces and moments on the aircraft use the provided aerodynamic coefficients and derivatives for the Aerosonde UAV. An aerodynamic coefficient is a non-dimensional force or moment such as the yaw moment coefficient (C_n) described by the equation $C_n = \frac{n}{0.5\rho {V_a}^2 S_{ref}}$ where n is the yaw moment (Figure 4.7), ρ is the freestream air density, V_a is the airspeed, and S_{ref} is the reference area of the aircraft. Therefore knowing the coefficient value, flight and aircraft characteristics one can calculate the yaw moment. Aerodynamic derivatives describe the rate of change of an aerodynamic coefficient with respect to a variable. For example, the aerodynamic derivative C_{nr} describes the rate of change of the yaw moment coefficient (C_n) with respect to yaw rate (r). The dynamic model assumes a linear variation of all coefficients since the derivatives are constant. All aerodynamic coefficients, derivatives and aircraft physical data for the Aerosonde are provided in a configuration file included with the AeroSim blockset.

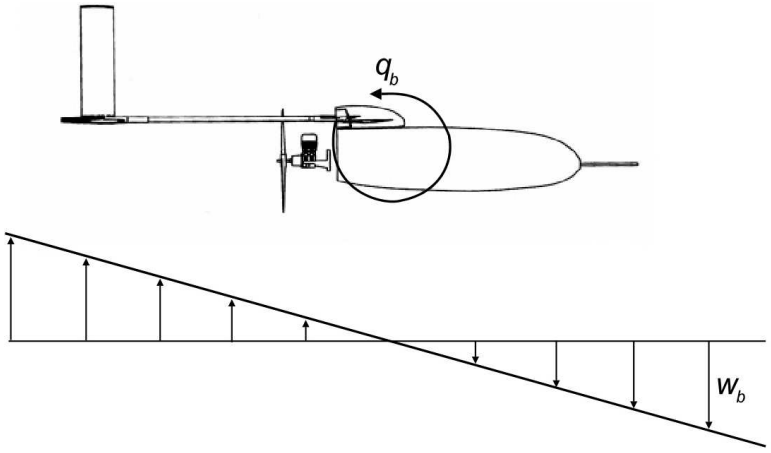

(a) Relative air velocity distribution due to aircraft motion

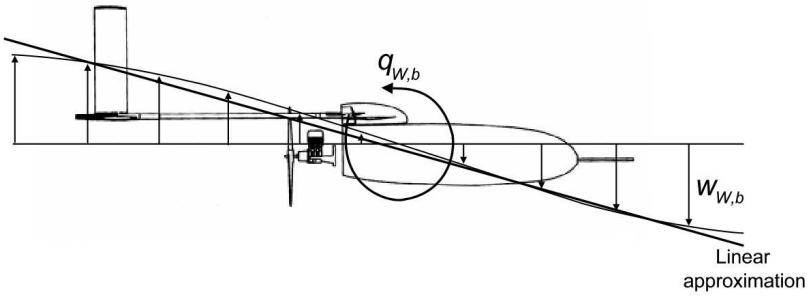

(b) Approximation of effective pitch rate $q_{W,b}$ due to wind

Figure 4.13: Representation of relative flow velocity to dynamic model

The dynamic model takes the aircraft's inertial velocity and angular rates (represented in body frame coordinates) and stores it as a vector $[u_b\ v_b\ w_b\ p_b\ q_b\ r_b]_{body}$, which is used for the

calculation of aerodynamic forces and moments. Referencing Figure 4.7, u_b, v_b and w_b are the x_b, y_b and z_b aircraft velocities in the body frame, respectively, and p_b, q_b, and r represent the aircraft roll, pitch, and yaw rates in the body frame, respectively. In terms of the wind field local to an aircraft, Figure 4.13a llustrates how aircraft rotational motion about one of the body axes produces a linearly varying velocity profile along another body axis (in the case of Figure 4.13a a pitch rate q_b produces a linear w_b air velocity profile along the aircraft x_b axis). Figure 4.13b shows a typical $w_{W,b}$ (z_b component of the inertial wind velocity) profile along the aircraft x_b axis (such as might be encountered in the wake of a building) which approximates a linear variation ('Linear approximation', Figure 4.13b) and therefore can be approximately represented by an effective pitch rate due to wind motion $q_{W,b}$. For example, if the aircraft was actually pitching with rate $q_{W,b}$ the linear approximation to the wind field in Figure 4.13b would be the relative w_b distribution seen by the aircraft due to the pitching motion. Therefore to incorporate the urban wind data into the dynamic model the wind field local to the aircraft can be modeled as a wind vector $[u_{W,b}\ v_{W,b}\ w_{W,b}]_{body}$ representing the actual wind vector at the aircraft CoG and an effective rate vector $[p_{W,b}\ q_{W,b}\ r_{W,b}]_{body}$ to account for the variation of the wind (approximated as linear) across the dimensions of the aircraft. Reversing the sign of the components of $[u_{W,b}\ v_{W,b}\ w_{W,b}]_{body}$ (since we want the aircraft motion relative to the air), the wind and effective rate vectors can then be superimposed on top of the aircraft $[u_b\ v_b\ w_b\ p_b\ q_b\ r_b]_{body}$ vector so that forces and moments due to the effects of urban wind are included in the calculation.

To calculate the rate vector from the CFD wind field data, the four point model of Etkin [66] is used. This method requires wind velocity components (represented in the body axis) at four locations on an aircraft shown in Figure 4.14. Point 0 is the aircraft's centre of mass, l_t is the length of the tail arm, and the value of b' is 85% of the wing span as recommended by Holley and Bryson [67]. This model assumes that the variation of the wind data velocity components $v_{W,b}$, $w_{W,b}$ along the longitudinal axis and $u_{W,b}$, $w_{W,b}$ along the lateral axis are approximately linear. The suitability of this linear approximation is investigated by looking at the distribution of the streamwise and vertical components of the wind across a few different wakes as shown in Figures 4.15a - 4.15c. The sampling axis is chosen to be at constant altitude ($z_{CFD}/H = 0.5$) and aligned with $+x_{CFD}$ (across the wake) since at this orientation it cuts

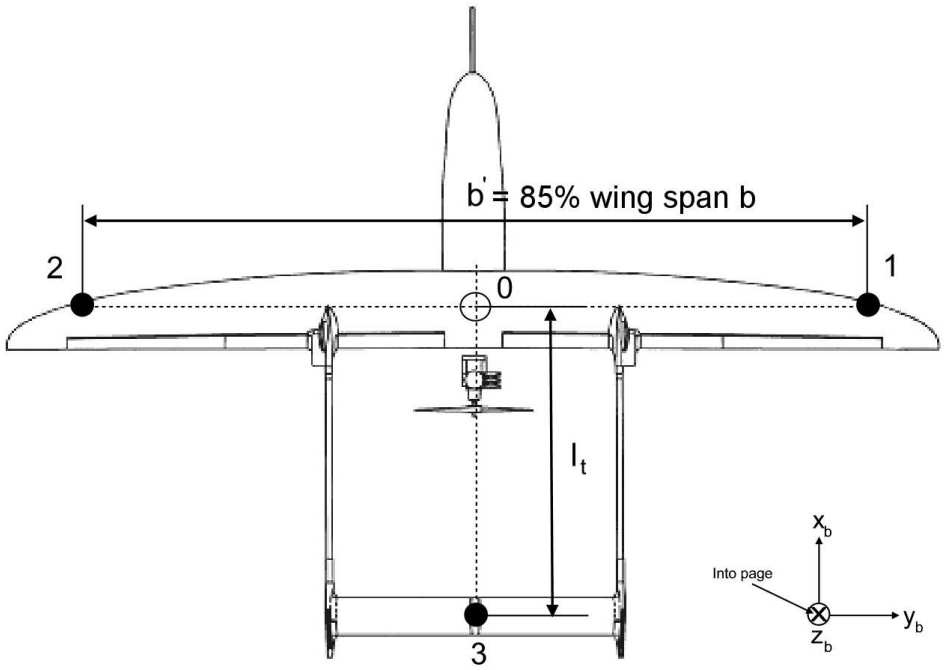

Figure 4.14: 4-point gust gradient model

through the sharpest wind gradients in the flow. If the aircraft is flying wings-level along this axis with the aircraft fuselage aligned with the same axis then the streamwise and vertical wind component distributions correspond to effective yaw ($r_{W,b}$) and pitch ($q_{W,b}$) rates, respectively. Figures 4.16 - 4.18 are plots of these distributions, where the x-axis has the non-dimensionalized variable X_C/W, where X_C is the distance from the single building or canyon centroid and W is the width of the single building or average width of the buildings in the canyon. The black bar represents the approximate tail-to-nose length of the Aerosonde UAV. Essentially the areas of interest are those with a large d^2V_W/dx^2 since this represents a significant rate of change of the linear rate of change of wind velocity with distance, exactly what the 4-point model assumes to not exist in the flow (i.e. the 4-point model assumes $d^2V_W/dx^2 = 0$).

Figure 4.16a is the streamwise wind velocity component distribution across the single building case 1b wake (Figure 4.15a), with location 1 representing a region with one of the largest values of $d^2v_{W,b}/dx^2$ in the wake. This large $d^2v_{W,b}/dx^2$ is caused by the wind velocity transitioning between the accelerated air (from background conditions) around the sides of the buildings and the strip of low velocity air behind the building. In more concrete terms, the

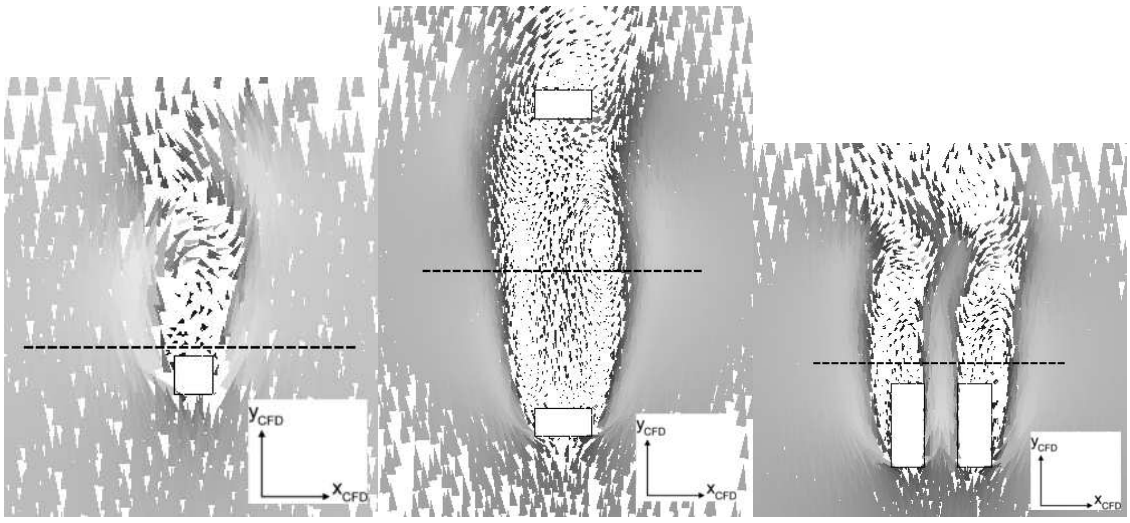

(a) Single building case 1b (b) Canyon case 1b (c) Canyon case 2b

Figure 4.15: Vector plots of the flow around the single building and canyon wakes used to investigate the suitability of the four point model. The dashed line is the horizontal axis along which the wind velocities are sampled, and has an altitude of half the single building or canyon height.

velocity gradient over the right half of the black bar at location 1 is quite steep and the gradient over the left half of the bar is almost horizontal, resulting in different parts of the aircraft experiencing different effective rates. Location 2 is in the shear layer between the accelerated flow and the low velocity flow behind the building and is the ideal region for the application of the 4-point model, since in this $d^2v_{W,b}/dx^2 \approx 0$. Surrounding location 3 are regions with large $d^2v_{W,b}/dx^2$, however, right at location 3 $d^2v_{W,b}/dx^2 \approx 0$ which indicates that the 4-point model holds well in the middle of the wake. Overall, the regions with large $d^2v_{W,b}/dx^2$ form a fairly small fraction of the overall width of the wake and therefore the error in using the four point model in these regions will only affect the aircraft for a very brief time. Figure 4.16b is the vertical wind velocity component distribution across the single building case 1b wake. The same arguments as for Figure 4.16a apply here since the pattern is the same as for the streamwise distribution, except with smaller velocities and $d^2w_{W,b}/dx^2$ values. The location with one of the largest $d^2w_{W,b}/dx^2$ in the wake is shown by the black bar.

Figures 4.17a and 4.17b are the streamwise and vertical wind velocity component distributions, respectively, across the canyon case 1b wake (Figure 4.15b). These plots are the same as the single building case 1b plots (Figures 4.16a and 4.16b) except that the largest wind gra-

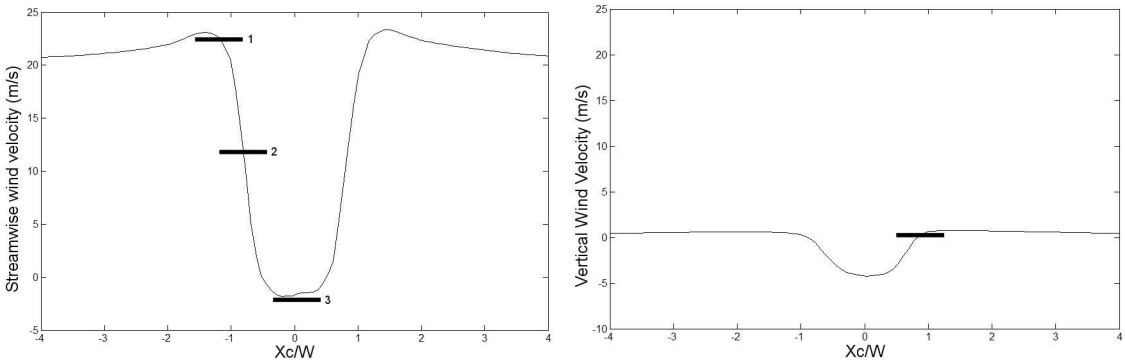

(a) Distribution of the streamwise component of wind velocity across the wake

(b) Distribution of the vertical component of wind velocity across the wake

Figure 4.16: Streamwise and vertical components of wind velocity across the single building case 1b wake. The black bar represents the approximate tail-to-nose length of the Aerosonde UAV.

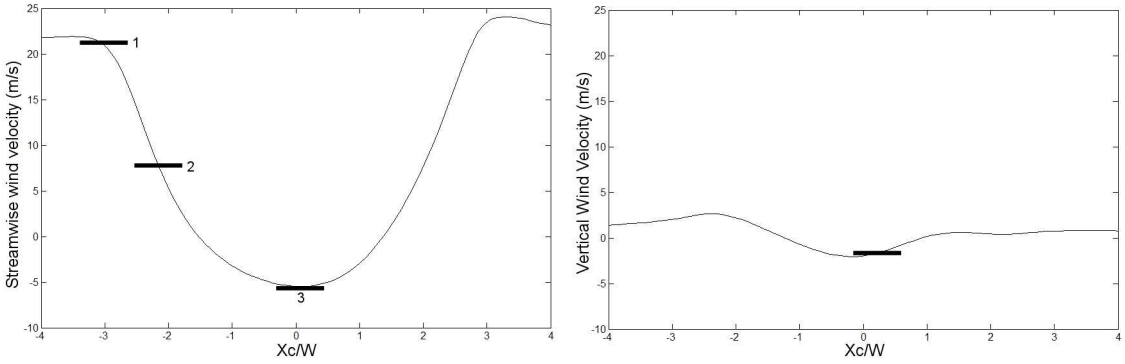

(a) Distribution of the streamwise component of wind velocity across the wake

(b) Distribution of the vertical component of wind velocity across the wake

Figure 4.17: Streamwise and vertical components of wind velocity across the canyon case 1b wake. The black bar represents the approximate tail-to-nose length of the Aerosonde UAV.

dients and $d^2v_{W,b}/dx^2$, $d^2w_{W,b}/dx^2$ values are much smaller. This indicates that the 4-point model is an even better approximation for the flight path shown in Figure 4.15b than for the flight path across the single building case 1b wake as shown in Figure 4.15b.

Figures 4.18a and 4.18b are the streamwise and vertical wind velocity component distributions, respectively, across the canyon case 2b wake (Figure 4.15c). The values of $d^2v_{W,b}/dx^2$ at locations 1 and 2 in Figure 4.18a are approximately the same as from the single building case 1b plot (Figure 4.16a), but the value of $d^2v_{W,b}/dx^2$ at location 3 is larger than at location 3 in Figure 4.16a. There is no significant difference between the largest $d^2w_{W,b}/dx^2$ values for the distribution of the vertical component of the wind across the single building case 1b and

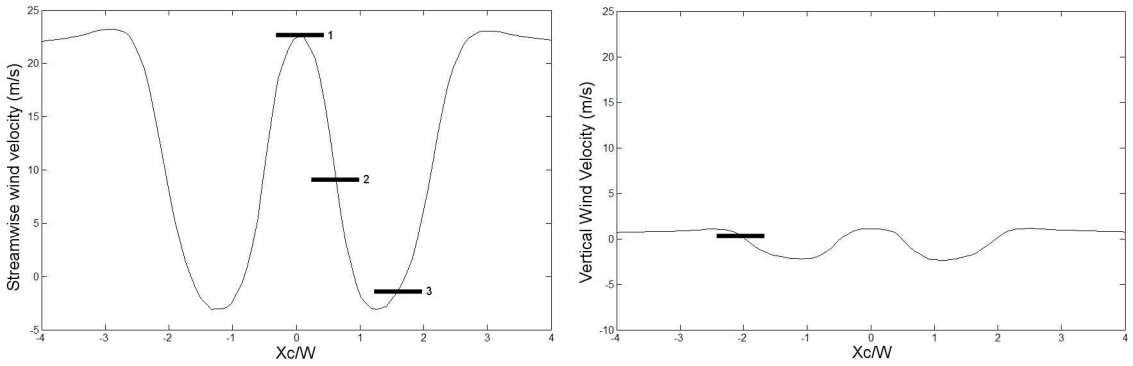

(a) Distribution of the streamwise component of wind velocity across the wake

(b) Distribution of the vertical component of wind velocity across the wake

Figure 4.18: Streamwise and vertical components of wind velocity across the canyon case 2b wake. The black bar represents the approximate tail-to-nose length of the Aerosonde UAV.

canyon case 2b wakes. The results from the distribution of the streamwise wind component indicate that the 4-point model doesn't work quite as well for the flight path across the canyon case 2b wake (as shown in Figure 4.15c) as for the flight path across the single building case 1b wake (as shown in 4.15a). However, a significant part of the canyon case 2b wake is still suitable for the 4-point model.

Under the assumption of linear wind gradients, the velocities $u_{W,b,i}$, $v_{W,b,i}$, $w_{W,b,i}$ at the four points (for example, $w_{W,b,2}$ is the z_b component of the inertial wind velocity at point 2) are used to calculate the effective rates $p_{W,b}$ $q_{W,b}$ and $r_{W,b}$ through the following equations

$$p_{W,b} = \frac{1}{b'}\left(w_{W,b,2} - w_{W,b,1}\right) \tag{4.8}$$

$$q_{W,b} = \frac{1}{l_t}\left(w_{W,b,0} - w_{W,b,3}\right) \tag{4.9}$$

while two possible yaw rates (since a yaw rate sets up a $u_{W,b}$ distribution along the wing and a $v_{W,b}$ distribution along the fuselage) are calculated as

$$r_{W1,b} = \frac{1}{b'}\left(u_{W,b,1} - u_{W,b,2}\right) \tag{4.10}$$

$$r_{W2,b} = \frac{1}{l_t}\left(v_{W,b,3} - v_{W,b,0}\right) \tag{4.11}$$

where the value used for $r_{W,b}$ in the wind effects vector is the average of $r_{W1,b}$ and $r_{W2,b}$. The remaining components of the wind effects vector are given by $u_{W,b} = u_{W,b,0}$, $v_W = v_{W,b,0}$, and $w_{W,b} = (w_{W,b,0} + w_{W,b,1} + w_{W,b,3})/3$.

To summarize, the aircraft's attitude and location of the aircraft's centre of gravity in the urban environment are provided by the dynamic model. This information is used to calculate the locations of points 0 through 4 in the wind velocity field from the CFD solution. The vector $[u_{W,b}\ v_{W,b}\ w_{W,b}\ p_{W,b}\ q_{W,b}\ r_{W,b}]_{body}$ can then be calculated and added to the aircraft motions $[u_b\ v_b\ w_b\ p_b\ q_b\ r_b]_{body}$ (provided by the dynamic model) which is then passed to the Aerodynamics block in the dynamic model (Figures 4.5 and 4.6) so that the effects of wind with respect to aerodynamic forces and moments can be calculated.

The above analysis is done in the Urban Wind Effects subsystem (Figure 4.3). The appropriate CFD simulation data as selected by the Selection Algorithm function is accessed and the vector $[u_{W,b}\ v_{W,b}\ w_{W,b}\ p_{W,b}\ q_{W,b}\ r_{W,b}]_{body}$ is calculated so that the dynamic model can calculate the aerodynamic forces and moments on the aircraft due to urban wind. The inputs to the Wind Field Analysis block are aircraft position, attitude, urban environment data, Cluster Selector, Data Selector (which entry in the WSD is to be analyzed), the Solution Height, centroid location (Solution Centroid, in the ENU frame) and characteristic length (Solution Char Length) of the single building or canyon in whose wake the aircraft was found to be located. If the solution returned by the Selection Algorithm is the background wind solution, the Solution Height, Solution Centroid, and Solution Char Length have a value of zero. Flight simulation terminates if Cluster Selector = 0 (the Selection Algorithm returns no solution). The output variables Urban Wind VelB and Urban Wind RatesB represent the urban wind velocity at the aircraft CoG in the body frame ($[u_{W,b}\ v_{W,b}\ w_{W,b}]_{Body}$) and the effective rates in the body frame ($[p_{W,b}\ q_{W,b}\ r_{W,b}]_{Body}$), respectively.

The wind field analysis differs depending on the value of the Cluster Selector. If it has a value of 0 then the wind field local to the aircraft is just the background wind field, meaning that the output variable Urban Wind VelB is the constant wind vector in the ENU frame rotated to the body frame. Recalling Equation 4.2, a vector in the body frame may be obtained by multiplying the vector in the NED frame by the DCM. However the background wind vector is initially specified in the ENU frame, so first a transformation from the ENU to NED frame

is needed. This is straightforward, since the only difference between the two frames is that the x and y axes are switched and the z axis is of opposite sign. Therefore, the wind vector at the aircraft's CoG in the body frame ($\vec{w}_{A/C,b}$) is given by

$$\vec{w}_{A/C,b} = DCM \cdot \vec{w}_{A/C,NED} = DCM \cdot P_{x\leftrightarrow y,-z} \cdot \vec{w}_{A/C,ENU} \tag{4.12}$$

where

$$P_{x\leftrightarrow y,-z} = \begin{pmatrix} 0 & 1 & 0 \\ 1 & 0 & 0 \\ 0 & 0 & -1 \end{pmatrix} \tag{4.13}$$

is the permutation matrix which switches the x and y axes and reverses the z axis. Because the background wind is constant there exist no gradients and all the effective rates are zero (i.e. Urban Wind RatesB = 0).

If the Cluster Selector has a value of 1 or 2 then the procedure followed is the implementation of the 4-point model. The wind velocity data is extracted from the absolute locations of all four points in the CFD frame. The determination of the aircraft CoG location (point 0 from the 4-point model) in the CFD frame starting from the geodetic spherical frame first requires the use of Equations 4.5a-4.5c to take the aircraft position to the ENU frame from the geodetic spherical frame. Once in the ENU frame, the aircraft position in the WCH frame can be calculated using Equation 4.7. Recalling Figure 4.8, the CFD frame is similar to the WCH frame in that the alignment and labeling of the axes are identical, but the geometric scale and location of the origin are not necessarily the same. The geometric scale may differ because the CFD simulation representing the flow around the single building or canyon of interest in the urban environment has only to match wind incidence, geometric ratio (i.e. L/W), and Reynold's number. It is therefore necessary to introduce a scaling factor $S_g = D_{sim}/D_{real}$ which scales the WCH frame to the CFD frame. The parameter D_{real} is the actual characteristic length of the single building or canyon in the urban environment (the Solution Char Length variable, an output from the Selection Algorithm) and D_{sim} is the characteristic length of the single

building or canyon in the corresponding CFD simulation. To obtain the value for D_{sim} the Cluster Selector and Data Selector variables are used to access the Simulation Characteristics File (SCF) which contains the characteristic length for the simulation. The Cluster Selector determines whether the file is a single building (Cluster Selector = 1) or canyon file (Cluster Selector = 2) and the Data Selector determines the file number. For example, a Cluster Selector value of 2 and a Data Selector value of 1 would indicate a SCF with the name `canyon1.txt`.

Adding the single building or canyon height to the aircraft position in the WCH frame and then scaling the coordinates to the CFD frame scale gives the relative position of the aircraft with respect to the single building or canyon in the CFD frame. To get the absolute position in the CFD frame, this relative position is added to the centroid location in the corresponding single building or canyon CFD simulation ($\vec{p}_{Building,CFD}$). This is obtained from the corresponding SCF in the same manner as D_{sim}. In summary, the aircraft CoG position in the CFD frame ($\vec{p}_{A/C,CFD}$) is given by

$$\vec{p}_{A/C,CFD} = S_g \cdot R(-\theta_{WA}) \cdot \left[\vec{p}_{A/C,ENU} - \vec{p}_{Building,ENU}\right] + \vec{p}_{Building,CFD} \tag{4.14}$$

The locations of points 1-3 from the 4-point model in the CFD frame are calculated by taking their positions relative to the CoG (point 0) in the body frame, transforming these relative position vectors into the CFD frame, and adding them to $\vec{p}_{A/C,CFD}$. The relative position vectors of points 1-3 in the body frame are

$$\vec{x1}_{relA/C,b} = \begin{pmatrix} 0 \\ b' \\ 0 \end{pmatrix}, \quad \vec{x2}_{relA/C,b} = \begin{pmatrix} 0 \\ -b' \\ 0 \end{pmatrix}, \quad \vec{x3}_{relA/C,b} = \begin{pmatrix} -l_t \\ 0 \\ 0 \end{pmatrix} \tag{4.15}$$

where, for example, $\vec{x1}_{relA/C,b}$ is the position of point 1 relative to the aircraft CoG in the body frame. The first step in transforming any one of the vectors to the CFD frame is a rotation to the NED frame through pre-multiplication by DCM^T (Equation 4.3). Next the x

and y axes must be switched and the z-axis reversed through pre-multiplication by $P_{x\leftrightarrow y,-z}$ (Equation 4.13) in order to get the ENU frame coordinates. Finally a rotation of this vector by $-\theta_{WA}$ about the z-axis (Equation 4.6) and a multiplication by the geometric scaling factor S_g puts the vector in the CFD frame. To get the absolute position of one of the points from the 4-point model in the CFD frame, the corresponding relative position vector in the CFD frame is added to the absolute position of the aircraft's CoG in the CFD frame ($\vec{p}_{A/C,CFD}$, Equation 4.14). Therefore a relative position vector to the aircraft CoG in the CFD frame ($\vec{x}_{relA/C,CFD}$) and the corresponding absolute location of the point on the aircraft in the CFD frame ($\vec{p}_{onA/C,CFD}$) are given by the following equations

$$\vec{x}_{relA/C,CFD} = S_g \cdot R(-\theta_{WA}) \cdot P_{x\leftrightarrow y,-z} \cdot DCM^T \cdot \vec{x}_{relA/C,b} \tag{4.16}$$

$$\vec{p}_{onA/C,CFD} = \vec{p}_{A/C,CFD} + \vec{x}_{relA/C,CFD} \tag{4.17}$$

Now that all four points from the 4-point model are located in the CFD frame, one is able to obtain the flow velocity at these points from the CFD simulation. This is accomplished by running CFX in batch mode from the Matlab environment; a completely automated process where the CFD simulation results file is opened by the CFX post-processor (CFX-Post) and a session file is played which instructs CFX-Post to return the flow velocities at the points corresponding to the four points on the aircraft. The command line

```
!C:AnsysInc\CFX\CFX-10.0\bin\cfx5post -batch sessionfile.cse
resultsfile.res
```

breaks out of the Matlab shell into DOS, runs the CFX-Post binary `cfx5post` located in the specified directory, opens the CFX results (`.res`) file, and plays the session (`.cse`) file. The contents of the session file may be changed during flight simulation, but the command line text itself cannot be changed, so a version of this command with a unique results file exists for every combination of Cluster Selector and Data Selector values which correspond to an entry in the WSD. A command line corresponding to a given entry in the WSD has the corresponding

results file written in. During flight simulation the session file is updated with the new locations of the four points. Manually opening a results file in CFX-Post and recording a session wherein the velocities at four points are manually extracted and exported produces a session file which can be used as a template. The CFX User's Manual [61] describes this process in further detail.

Once the wind velocities at the four points have been found in the CFD frame, one must convert them to the aircraft body frame so the body frame wind velocity at the aircraft CoG can be obtained and Equations 4.8-4.11 in section 4.4 can be applied to calculate the effective rates. Recalling that the flow around a single building or canyon in an urban environment is dynamically similar to its representative CFD simulation, equating the Reynolds numbers and noting that the CFD simulation uses air as the working fluid the following relationship is obtained

$$V_{real} = \frac{V_{sim} \cdot D_{sim}}{D_{real}} \tag{4.18}$$

where V_{sim} is the magnitude of the wind velocity obtained from the CFD simulation. This velocity must be scaled to V_{real} and the scale factor relating V_{real} and V_{sim} is simply the geometric scale factor $S_g = D_{sim}/D_{real}$. Scaling V_{sim} to V_{real} gives the velocity vector in the WCH frame ($\vec{V}_{WCH}$), and a rotation of $\vec{V}_{WCH}$ by $+\theta_{WA}$ about the z axis gives the velocity in the ENU frame. Switching the x and y coordinates and flipping the z axis transforms the velocity vector $\vec{V}_{ENU}$ to the NED frame and pre-multiplication by the DCM yields the velocity vector in the body frame. In summary, a velocity vector in the body frame ($\vec{V}_b$) is calculated from a velocity vector in the CFD frame ($\vec{V}_{CFD}$) with the following equation

$$\vec{V}_b = DCM \cdot P_{x \leftrightarrow y,-z} \cdot R(\theta_{WA}) \cdot S_g \cdot \vec{V}_{CFD} \tag{4.19}$$

4.5 Autopilot/Waypoint Navigation

A certain level of aircraft control is necessary so that there exists a measure against which the effects of urban wind on flight performance can be measured. For this purpose a waypoint navigation scheme and an autopilot are designed and integrated into the flight simulation methodology (Figure 4.2). Figure 4.19 provides a top-level overview of the Simulink imple-

mentation of the Autopilot/Waypoint Analysis subsystem (a subsystem of the Urban Wind Effects subsystem, Figure 4.2b). The information required by the autopilot to implement the waypoint analysis scheme is provided by the Aircraft Control State and Waypoint Analysis block.

To successfully navigate a series of waypoints, each of them must be 'checked' by the aircraft in a prescribed order. A waypoint is defined as checked if it is passed by the aircraft within a certain predefined distance of 2.5m (~ 0.88 of the wingspan, b). The path to be followed by the aircraft in going from the previous waypoint (the last waypoint checked by the aircraft) to the target waypoint (the next waypoint on the list to be checked) as per the waypoint navigation scheme is a constant altitude straight line path extending from the previous waypoint to the target waypoint, called the Waypoint Navigation Vector (WNV), as illustrated in Figure 4.20. If the two waypoints have different altitudes then the altitude of the WNV is the altitude of the target waypoint.

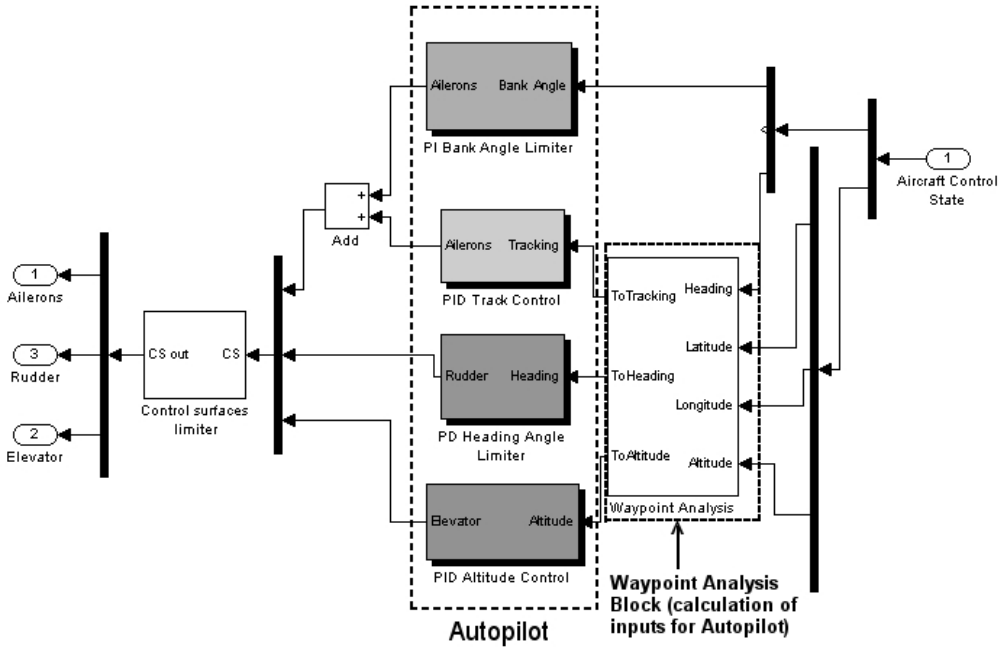

Figure 4.19: Top-level view of the Autopilot/Waypoint navigation subsystem

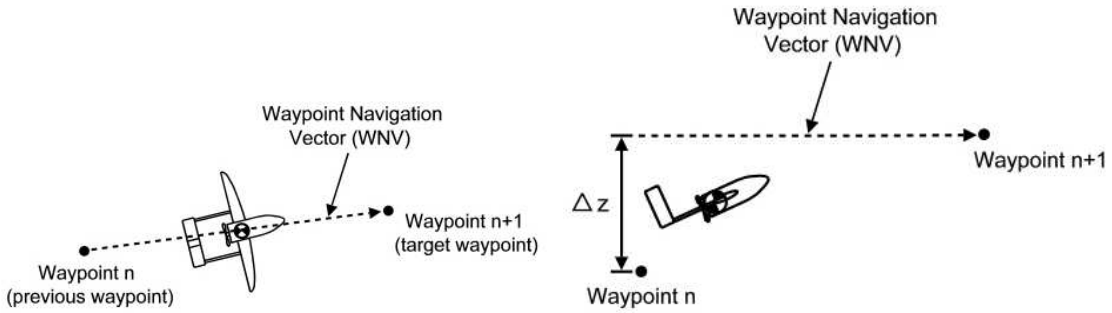

(a) Top view of Waypoint Navigation Vector

(b) Side view of Waypoint Navigation Vector, previous and target waypoints are at altitudes differing by Δz

Figure 4.20: Waypoint Navigation Vector (WNV)

There are five variables used by the autopilot to implement the waypoint navigation scheme: altitude deviation Δz, track deviation Δx, relative heading angle θ_{relH}, New Waypoint Flag, and Heading Correction Flag. Altitude deviation Δz is the difference between the current aircraft altitude and the altitude of the target waypoint. Track deviation Δx is the shortest distance from the aircraft's CoG to the current WNV, as illustrated in Figure 4.21a. The relative heading angle θ_{relH} is the difference between the heading of the aircraft and heading of the WNV, as illustrated in Figure 4.21b. The variable New Waypoint Flag is used to tell the autopilot if the target waypoint has been checked within two time steps of the current time step (New Waypoint Flag = 1 if checked, 0 otherwise). As illustrated in Figure 4.22, this is necessary since derivative controls in the autopilot which act on Δz, Δx, and θ_{relH} will overreact to the sudden changes in Δz, Δx and θ_{relH} which may occur as a result of checking a waypoint. The variable Heading Correction Flag is used to determine whether θ_{relH} is outside the range $-30^\circ \leq \theta_{relH} \leq 30^\circ$, taking a value of 1 if θ_{relH} is outside the range and 0 otherwise. If Heading Correction Flag = 1 then rudder control is activated in the autopilot in order to bring θ_{relH} back within $-30^\circ \leq \theta_{relH} \leq 30^\circ$, otherwise the rudder is brought back to (or maintained at) zero deflection. As such, the aircraft heading is considered to be satisfactorily aligned with the WNV as long as $-30^\circ \leq \theta_{relH} \leq 30^\circ$. For the sake of simplicity, it is desired that the ailerons are to be solely responsible for minimizing Δx, but if the rudder is continuously used to keep $\theta_{relH} \sim 0^\circ$ then the application of rudder deflections would interfere too much with the ailerons with respect to the control of Δx. The aerodynamics of the aircraft are such that it has natural way (i.e. requiring no active controls) of limiting heading angle in a crosswind

when rudder deflection is zero, called weathercock stability, where the fuselage aligns itself with the relative wind. If the crosswind isn't too large (fraction of crosswind magnitude to aircraft forward speed must be less than tan30° =0.58) then the aircraft relative heading will naturally settle into the range $-30° \leq \theta_{relH} \leq 30°$.

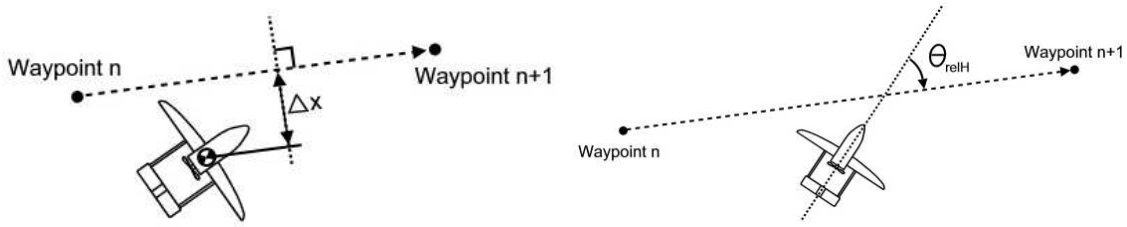

(a) Track deviation Δx

(b) Relative heading angle θ_{relH}

Figure 4.21: Illustration of track deviation Δx and relative heading angle θ_{relH}

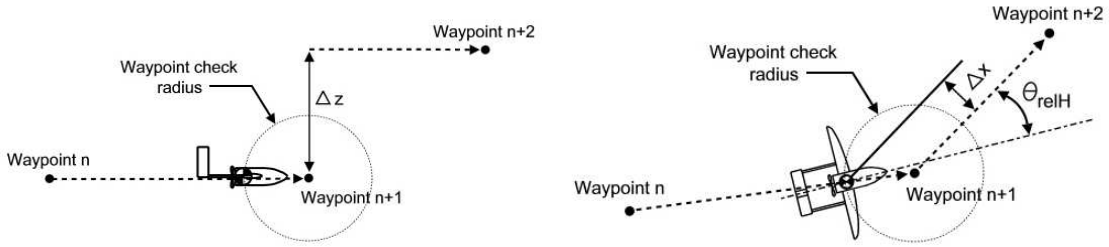

(a) Sudden change in altitude deviation Δz. Right before waypoint n+1 is checked Δz is small, but suddenly jumps to the larger Δz shown in the Figure when waypoint n+1 is checked.

(b) Sudden change in track deviation Δx and relative heading θ_{relH}. Right before waypoint n+1 is checked Δx and θ_{relH} are small, but suddenly jump to the larger values Δx and θ_{relH} shown in the Figure when waypoint n+1 is checked.

Figure 4.22: Demonstration of sudden change in Δz, Δx, and θ_{relH} when switching target waypoints

The calculation of Δz, Δx, θ_{relH}, New Waypoint Flag, and Heading Correction Flag as inputs to the autopilot is performed as follows. Waypoints in the East-North-Up (ENU) frame are specified in a `.txt` file in the order by which they are to be checked by the aircraft. Another `.txt` file is used to store and update the number of waypoints which have been checked by the aircraft during the simulation. By convention, the first waypoint is automatically checked at $t = 0$. At each time step the latitude, longitude and altitude are used to calculate the aircraft position in the ENU frame using Equations 4.5a-4.5c from section 4.1. The Waypoint Navigation Vector (WNV) is calculated by subtracting the previous waypoint location from the target waypoint. If the two waypoints are at different altitudes, the previous waypoint in

the calculation is given an altitude equal to that of the target waypoint. Initially, the previous and target waypoints are obtained by using the `.txt` files which list the waypoints and the current number which have been checked since the last time step. If it is determined that the aircraft location for the current time step is within the predefined distance from the target waypoint found from the `.txt` file, the target waypoint is set as the previous waypoint and the next waypoint on the list is the target waypoint and the WNV is calculated accordingly.

When a new waypoint is checked, New Waypoint Flag is given the value 1 and is held at that value until two time steps have passed after which it is then set to 0. To determine whether two time steps have passed, a `.txt` file is created which keeps track of the simulation time when the last waypoint was checked by the aircraft (Last Check Time), and it is initialized to 0 at $t = 0$. At each time step the Last Check Time is read in, and it is determined whether the current simulation time is at least two time steps past the Last Check Time.

Figure 4.23 illustrates the calculation of θ_{relH} and Δx starting with the WNV, aircraft position, and heading in the ENU frame. The navigation heading angle θ_N is calculated as the angle the WNV makes with the North-axis (positive clockwise). The aircraft heading θ_H (provided by the unmodified dynamic model, Figure 4.1) is passed to the Waypoint Analysis block, but must be slightly modified. As provided the aircraft heading is always a positive number between 0° and 360°, but is modified so that whenever $\theta_H > 180°$ then $\theta_H \Rightarrow \theta_H - 360°$ to get a negative number. The aircraft relative heading angle is then obtained from the calculation $\theta_{relH} = \theta_N - \theta_H$. To calculate Δx the waypoint and aircraft xy coordinates are rotated about the ENU frame origin (positive counterclockwise) by the amount θ_N to obtain the coordinates in the track-aligned frame (y-axis aligned with the WNV). In this frame it is a simple matter to calculate Δx from the aircraft x-coordinate in the track-aligned frame ($x_{A/C,t}$) and the x-coordinate of the waypoint navigation vector in the track-aligned frame ($x_{WNV,t}$) as $\Delta x = x_{WNV,t} - x_{A/C,t}$. Calculation of Δz is simply the aircraft altitude subtracted from the altitude of the target waypoint. Finally, the calculated value of θ_{relH} is compared to the range $-30° \leq \theta_{relH} \leq 30°$ and if it is outside the range then the Heading Correction Flag is set to 1, otherwise it is set to 0.

There are four components to the autopilot as illustrated in Figure 4.19: an altitude-hold PID controller ('PID Altitude Control'), a tracking-hold PID controller ('PID Track Control'),

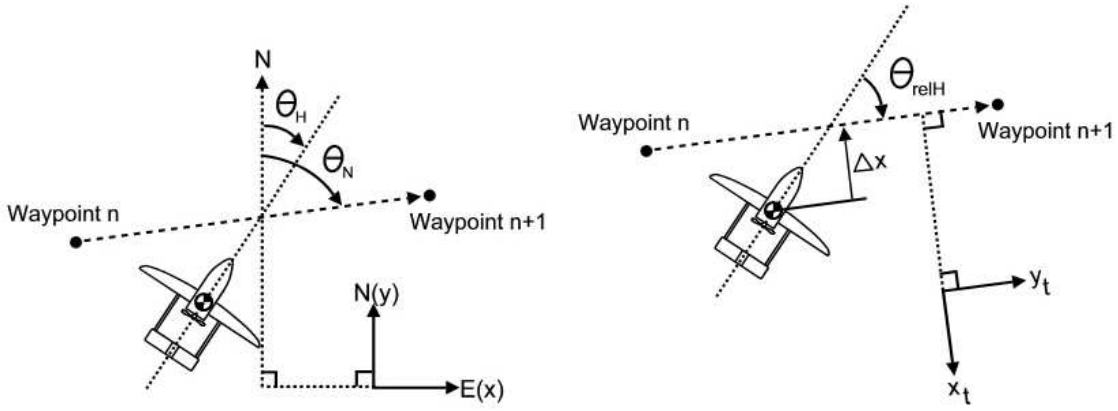

(a) Waypoint navigation vector, aircraft position and heading in the ENU frame. For this aircraft orientation, θ_{relH} is positive.

(b) Waypoint navigation vector, aircraft position and heading in the track-aligned frame. For this aircraft position, Δx is negative.

Figure 4.23: Calculation of θ_{relH} and Δx

a bank angle limiter PI controller ('PI Bank Angle Limiter'), and a relative heading angle limiter PD controller ('PD Heading Angle Limiter') . To simplify matters, the altitude-hold and tracking-hold controllers are decoupled by defining both of them to be responsible for the operation of a different control surface. The altitude-hold controller controls altitude via the elevator and the tracking-hold controller controls the via the ailerons. A wing leveler taken from a pre-existing AeroSim demonstration file is used as a bank angle limiter, and controls via aileron deflections, which are added to the deflections prescribed by the tracking-hold controller. The bank angle limiter works against the tracking-hold controller to limit the absolute bank angle and bank angle rate (roll rate), which is necessary since large bank angles result in sharp drops in altitude and rapid changes in bank angle result in significant oscillations in the aircraft's deviation from the desired track. The gains for the bank angle limiter have been slightly increased from their original values in the wing leveler. The relative heading angle limiter operates the rudder and its purpose is to keep θ_{relH} within the predefined range $-30° \leq \theta_{relH} \leq 30°$ and is only activated when θ_{relH} goes outside this range (i.e. when Heading Correction Flag = 1).

Referencing Figure 4.19, the input for the bank angle limiter only requires the aircraft bank angle which is extracted directly from the Aircraft Control State. The inputs for the altitude-hold controller, tracking-hold controller, and relative heading angle limiter come from the Waypoint Analysis block, which contains a function that calculates the inputs using the

aircraft heading, latitude, longitude, and altitude from the Aircraft Control State as previously discussed. PID Altitude Control requires Δz and New Waypoint Flag, PID Track Control requires Δx and New Waypoint Flag, and PD Heading Angle Limiter requires θ_{relH}, New Waypoint Flag, and Heading Correction Flag. If New Waypoint Flag = 1 the derivative control of all controllers with this variable as an input are turned off until two simulation time steps have passed.

All the controller outputs are routed through the Control Surfaces Limiter block which ensures the prescribed deflections and deflection rates of the control surfaces are kept within predefined limits. The deflection and deflection rate limits for each control surface are $\pm 30^\circ$ and $\pm 45^\circ$/s (sample values given by the AeroSim user's guide [62]), respectively. If a prescribed deflection should be out of range in either the + or - direction, the deflection is cut-off at the corresponding + or - range limit. The deflection rate is checked by comparing the current deflection with the deflection at the previous time step by storing the previous deflections with the corresponding simulation times in a `.txt` file that can be referenced. The deflection rate for the current simulation time $\frac{\Delta \delta_c}{\Delta t}$ is calculated as

$$\frac{\Delta \delta_c}{\Delta t} = \frac{\delta_{c,n} - \delta_{c,n-1}}{t_n - t_{n-1}} \tag{4.20}$$

If $\frac{\Delta \delta_c}{\Delta t}$ is found to be beyond one of the allowed + or - limits then the deflection at the current simulation time is recalculated based on the limiting deflection rate and used to update the aircraft state (in addition to being stored in a `.txt` file for reference at the next time step).

The specific values of the proportional, integral, and derivative gain constants K_p, K_i, and K_d for all controllers in the autopilot (Figure 4.19) were set by direct observation of how well various gain values minimized their respective state variables (i.e. Δz is the state variable corresponding to K_p, K_i, and K_d for PID Altitude Control) under constant Easterly, Westerly, Northerly and Southerly wind conditions of 4.15 m/s ($\sim$15 km/h). Table 4.1 summarizes the gain values for all controllers. Note that the proportional gains for the tracking-hold and bank angle limiter are of opposite sign, as are the integral gains, reflecting the intention that the tracking-hold and bank angle limiter controller are to work against one another.

Figure 4.24a is a schematic diagram of how the altitude-hold controller ('PID Altitude Control', Figure 4.19) operates. Beginning with aircraft altitude z_{ENU}, the Waypoint Analysis

Table 4.1: Gain Values for All Controllers

Controller	K_p	K_i	K_d
Altitude-hold	-0.075	-0.002	-0.1
Tracking-hold	-0.04	-0.005	-0.0825
Relative heading limiter	-0.03	0	-0.065
Bank angle limiter	0.02	0.001	0

function calculates Δz which is used by PID Altitude Control to prescribe an elevator deflection δ_e which is passed to the Dynamic Model to get a new z_{ENU}. A positive Δz value means the aircraft is below the target altitude and so the proportional, integral, and derivative gain constants should be negative numbers since a negative elevator deflection works to pitch the aircraft nose up and increase altitude (decrease Δz). Figure 4.24b shows the performance of the altitude-hold controller when the aircraft is flying a Northerly track with an initial altitude 10 m below the target altitude ($\Delta z = 10$ m). Four simulations are performed using Easterly, Westerly, Northerly, and Southerly background winds, all with a magnitude of 4.25 m/s. The aircraft successfully maintains altitude within ± 1 metre of the target altitude after only $\sim 2-3$ s for the Southerly wind case and ~ 10 s for all other cases. The aircraft initially climbs more rapidly for the Southerly wind case since here the aircraft is flying directly into the wind causing an increase in lift. All cases except the Southerly wind case exhibit a similar pattern over the entire simulation time, whereas the aircraft altitude for the Southerly case stays below the target altitude.

Figure 4.25a is a schematic diagram of how the tracking-hold controller ('PID Tracking Control', Figure 4.19) operates. Starting with the aircraft latitude and longitude the Waypoint Analysis block calculates the track deviation Δx and the value for New Waypoint Flag, both of which are used by PID Track Control to prescribe an aileron deflection δ_a which is passed to the Dynamic Model to get a new latitude and longitude. As previously discussed and illustrated in Figure 4.23b, a positive Δx means that the aircraft's right wing tip points towards the WNV (i.e. the WNV is displaced from the aircraft along the direction of the $+y_b$ body-frame axis, Figure 4.7). Since a negative δ_a will work to push the aircraft along $+y_b$ and therefore reduce Δx the gain constants are required to be negative (so a positive Δx input will produce a negative δ_a). Figure 4.25b shows the performance of the tracking-hold controller when the

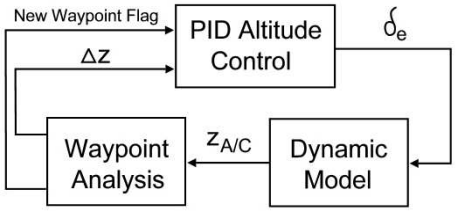

(a) Schematic view of altitude-hold controller operation

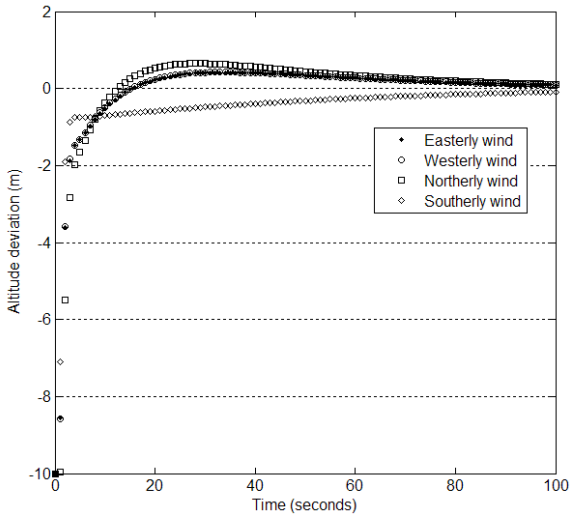

(b) Performance of altitude-hold controller

Figure 4.24: Altitude-hold controller

aircraft is given an initial value of $\Delta x = 10$m with respect to a Northerly track at constant altitude. The background winds specified for the tracking-hold controller simulations are the same as those used for the altitude-hold controller simulations (Figure 4.24b). The aircraft successfully maintains the desired track within ± 1 m of the target WNV (which in this case is directly North) after ~ 12 s for all wind cases. All cases exhibit a similar pattern over the entire simulation.

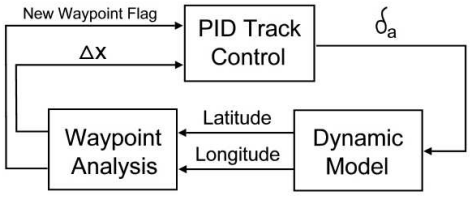

(a) Schematic view of the tracking-hold controller operation

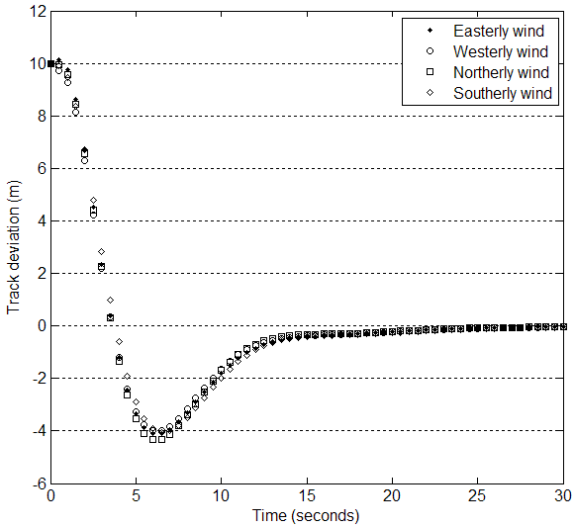

(b) Performance of tracking-hold controller

Figure 4.25: Tracking-hold controller

Figure 4.26 is a schematic diagram of how the relative heading angle limiter ('PD Heading Angle Limiter', Figure 4.19) operates. Starting with the aircraft heading θ_H the Waypoint Analysis block calculates the relative heading angle θ_{relH} and the values for New Waypoint Flag and Heading Correction Flag, all of which are used by PD Heading Angle Limiter to prescribe a rudder deflection δ_r which is passed to the Dynamic Model to get a new aircraft heading θ_H. A negative δ_r works to yaw the aircraft clockwise and therefore reduce the relative heading angle (Figure 4.21b), indicating that the controller gains should be negative. Figure 4.27a shows the performance of the relative heading angle limiter under a Southerly wind with a speed of 4.25 m/s while the aircraft is following a pair of tracks at constant altitude as shown in Figure 4.27b. As expected, the relative heading angle θ_{relH} jumps to $\sim -40°$ when waypoint 2 is checked due to the switching of target waypoints (Figure 4.22b). At this θ_{relH} the Heading Correction Flag is set to 1 and the relative heading angle limiter is activated which works to bring θ_{relH} above $-30°$. The autopilot, in attempting to follow WNV 2 (Figure 4.27b), prescribes a strong negative aileron deflection which, through aerodynamic coupling, produces a positive yawing moment in addition to reducing the track deviation. This yawing moment pushes θ_{relH} above $+30°$ but is resisted by the relative heading angle limiter which keeps θ_{relH} close to $+30°$ until the autopilot is no longer attempting to push θ_{relH} above $+30°$ (i.e. until the track deviation is low enough that the prescribed aileron deflections aren't strong enough to yaw the aircraft to such an extent).

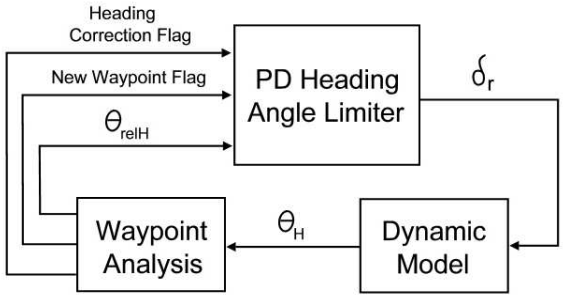

Figure 4.26: Schematic view of the relative heading angle limiter operation

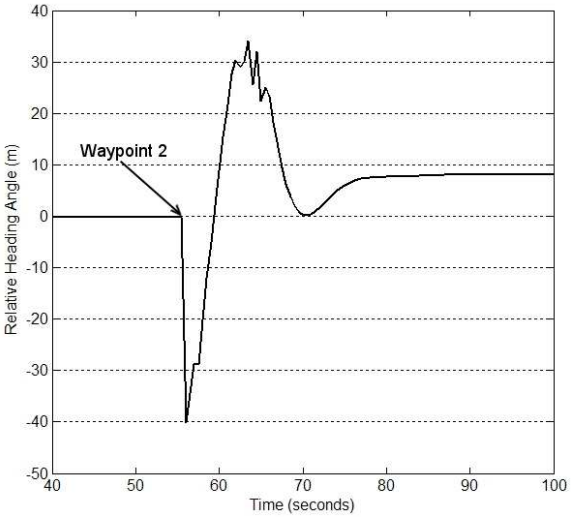

(a) Performance of relative heading angle limiter under a Southerly wind of 4.15 m/s, following the tracks shown in Figure 4.27b

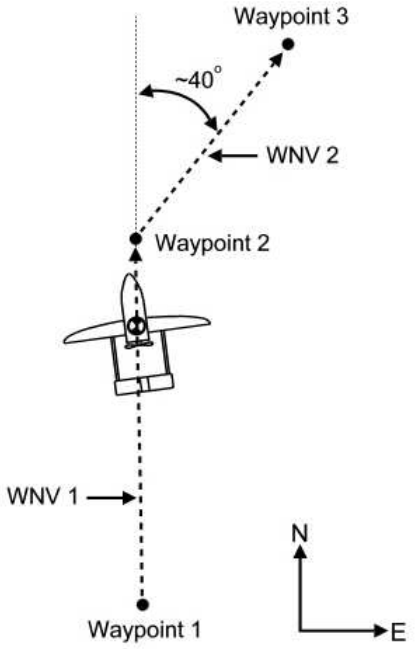

(b) Illustration of the two tracks (represented by WNV 1 and WNV 2) the aircraft is to follow in succession in order to investigate the performance of the relative heading angle limiter and bank angle limiter

Figure 4.27: Relative heading angle limiter

Figure 4.28a is a representative diagram of the bank angle limiter. This is essentially a wing-leveler taken directly from an Aerosonde flight demo provided with the AeroSim blockset. It reads in the bank angle of the aircraft θ_{bank} and prescribes aileron deflections δ_a to reduce the angle to zero. As illustrated in Figure 4.19, these aileron deflections are added to the aileron deflections prescribed by the tracking-hold controller. The combined purpose of these two controllers is to control the aircraft track while keeping the bank angle at reasonable levels. The magnitude of the gain constants are increased slightly from their original values in order to maintain tighter control over bank angle variations. Figure 4.28b shows the performance of the bank angle limiter under the same flight path and conditions as for the relative heading angle limiter (Figure 4.27b). The most notable region is right after the second waypoint has been checked. At this point the target track is switched to WNV 2 (Figure 4.27b) causing a sudden increase in Δx (Figure 4.22b) which in turn causes the autopilot to strongly bank the aircraft. The bank angle limiter successfully limits the maximum bank angle to $\sim 35°$.

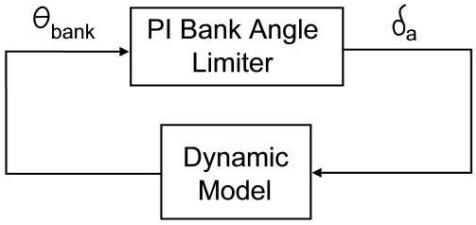

(a) Schematic view of the bank angle limiter opration

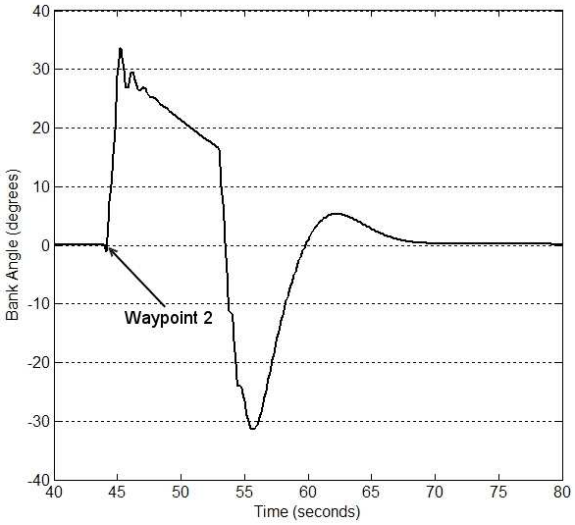

(b) Performance of bank angle limiter under a Southerly wind of 4.15 m/s, following the tracks shown in Figure 4.27b

Figure 4.28: Bank angle limiter

Chapter 5

Results of Flight Simulation Through an Urban Environment

Figures 5.1 - 5.4 illustrate the urban environment in which aircraft flight is simulated. A top view and three-dimensional view of the buildings which make up the urban environment are shown in Figures 5.1 and 5.2, respectively. The buildings are placed in a constant background Westerly wind of 4.15 m/s (∼8 kts, ∼15 km/h). Each of the buildings in the top view (Figure 5.1) are assigned a unique number and labeled accordingly (e.g. the label 'B3' refers to building # 3), and Table 5.1 provides a description of the geometry and orientation of each of these buildings in the urban environment.

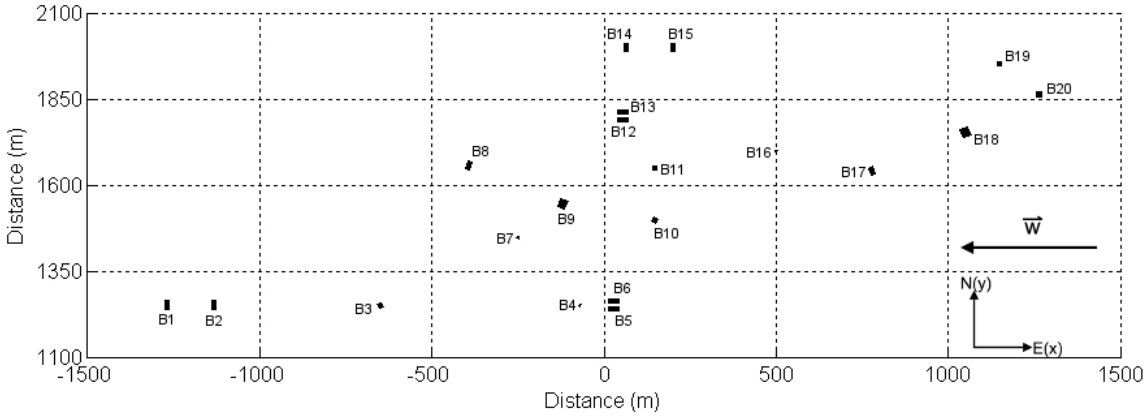

Figure 5.1: Top view of buildings in the urban environment

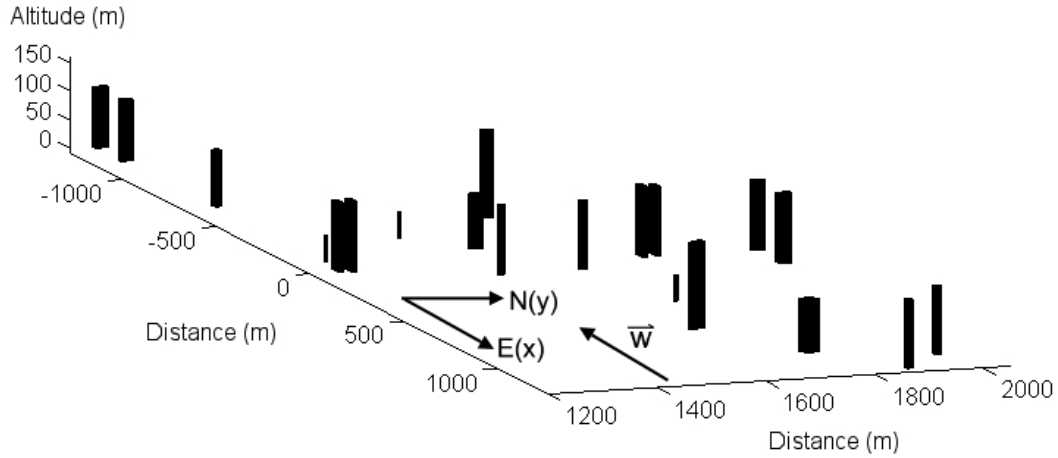

Figure 5.2: Three-dimensional view of buildings in the urban environment

Table 5.1: Buildings in the Urban Environment

Building #	**Height (m)**	**Width (m)**	**Length (m)**	**Orientation (wrt Eastern direction)**
1, 2	107.5	12.06	24.12	0°
3	100	12.06	12.06	22.5°
4	45	5.1	5.1	159.75°
5, 6, 12, 13	122.95	12.06	30.15	90°
7, 16	45	5.1	5.1	157.5°
8	153.46	12.06	24.12	157.5°
9	92.43	24.12	24.12	157.5°
10	120.6	12.06	12.06	158°
11, 19, 20	120.6	12.06	12.06	0°
14, 15	122.95	12.06	24.12	0°
17	153.46	12.06	24.12	22.5°
18	92.43	24.12	24.12	22.5°

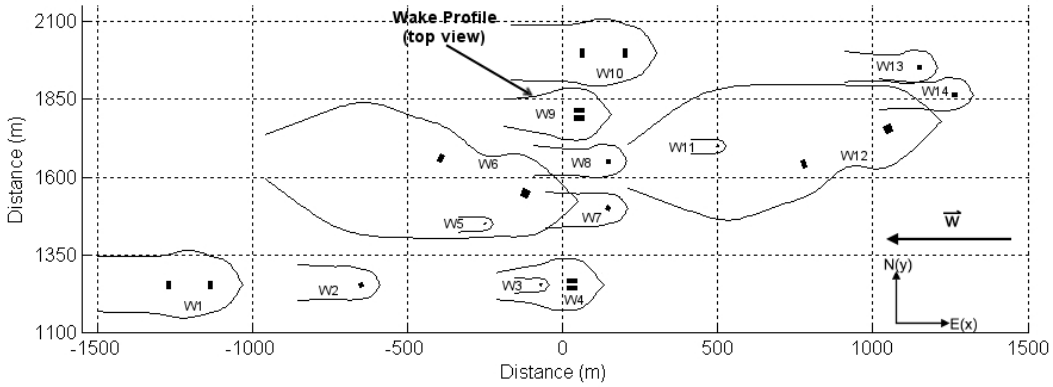

Figure 5.3: Top view of wakes in the urban environment

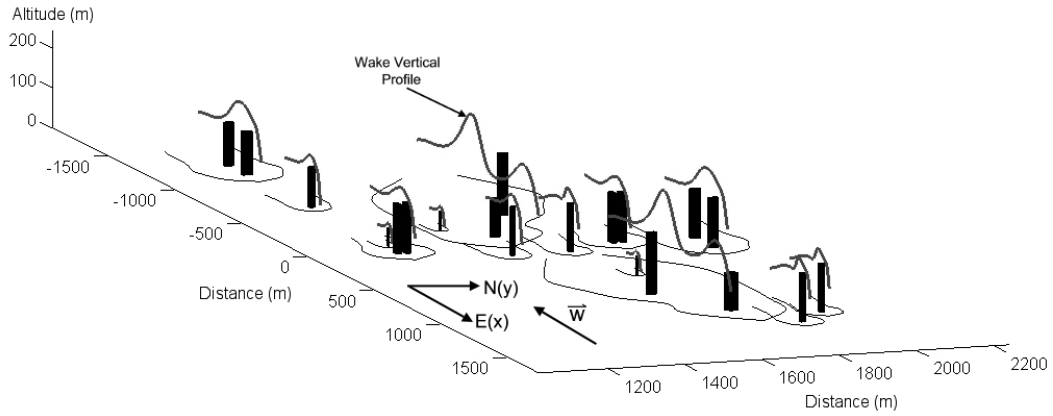

Figure 5.4: Three-dimensional view of urban environment including top wake profiles

A top view of the urban environment showing the left and right boundary wake shape functions and a three-dimensional view showing the vertical boundary wake shape functions for all single buildings and canyons in the environment are shown in Figures 5.3 and 5.4. Each of the wakes in the top view (Figure 5.3) are assigned a unique number and labeled accordingly (e.g. the label 'W3' refers to wake # 3), and Table 5.2 provides a description of each wake in the urban environment, such as the building(s) involved in the creation of the wake, the wind incidence angle, and in the case of a canyon the windward and leeward buildings and the canyon geometry. The values for all parameters that are used to describe a given wake in the urban environment have the same values as the CFD simulation of the wind data in the wake unless otherwise noted with the subscript 'CFD'. For example, wake 7 (W7) is formed by a single building with a wind incidence angle of $\theta_W = 22°$ but is represented by a CFD

Table 5.2: Wakes in the Urban Environment

Wake #	**Class and Buidings Involved**	**Description**
1	Canyon, B1 (leeward) and B2 (windward)	$\theta_W = \theta_{W,CFD} = 0°$, FlipData = 0, $Re = 7.21\times10^6$, $R_\perp/R_{\|\|_{ww}} = 2$, $R_\perp/R_{\|\|_{lw}} = 2$, $S/H_{avg} = 1.08$, $S/H_{avg_{CFD}} = 1$ (skimming flow), $\Delta H/D_{avg} = 0$, $H_{avg}/D_{avg} = 4.56$
2	Single building, B3	$\theta_W = 157.5°$, $\theta_{W,CFD} = 22.5°$, FlipData = 1, $Re = 4.73\times10^6$, $L/W = 1$
3	Single building, B4	$\theta_W = 20.25°$, $\theta_{W,CFD} = 22.5°$, FlipData = 0, $Re = 2\times10^6$, $L/W = 1$
4, 9	Canyon, B5 (windward) and B6 (leeward), B12 (windward) and B13 (leeward)	$\theta_W = \theta_{W,CFD} = 0°$, FlipData = 0, $Re = 8.68\times10^6$, $R_\perp/R_{\|\|_{ww}} = 2.5$, $R_\perp/R_{\|\|_{lw}} = 2.5$, $S/H_{avg} = 1/10.2 \approx 0.1$, $\Delta H/D_{avg} = 0$, $H_{avg}/D_{avg} = 3.79$
5, 11	Single building, B7	$\theta_W = \theta_{W,CFD} = 22.5°$, FlipData = 0, $Re = 2\times10^6$, $L/W = 1$
6	Canyon, B8 (leeward) and B9 (windward)	$\theta_W = \theta_{W,CFD} = 22.5°$, FlipData = 0, $Re = 8.17\times10^6$, $R_\perp/R_{\|\|_{ww}} = 1$, $R_\perp/R_{\|\|_{lw}} = 2$, $S/H_{avg} = 2.25$, $\Delta H/D_{avg} = 1$, $H_{avg}/D_{avg} = 4.02$
7	Single building, B10	$\theta_W = 22°$, $\theta_{W,CFD} = 22.5°$, FlipData = 0, $Re = 4.73\times10^6$, $L/W = 1$
8, 13, 14	Single building, B11, B19, B20	$\theta_W = \theta_{W,CFD} = 0°$, FlipData = 0, $Re = 4.73\times10^6$, $L/W = 1$
10	Canyon, B14 (leeward) and B15 (windward)	$\theta_W = \theta_{W,CFD} = 0°$, FlipData = 0, $Re = 7.21\times10^6$, $R_\perp/R_{\|\|_{ww}} = 2$, $R_\perp/R_{\|\|_{lw}} = 2$, $S/H_{avg} = 1.23$, $S/H_{avg_{CFD}} = 1$ (skimming flow), $\Delta H/D_{avg} = 0$, $H_{avg}/D_{avg} = 4.56$
12	Canyon, B17 (leeward) and B18 (windward)	$\theta_W = 157.5°$, $\theta_{W,CFD} = 22.5°$ FlipData = 1, $Re = 8.17\times10^6$, $R_\perp/R_{\|\|_{ww}} = 1$, $R_\perp/R_{\|\|_{lw}} = 2$, $S/H_{avg} = 2.25$, $\Delta H/D_{avg} = 1$, $H_{avg}/D_{avg} = 4.02$

simulation with $\theta_{W,CFD} = 22.5°$ (Table 5.2) since $\theta_W = 22°$ is within the wind incidence tolerance range ($\pm 11.25°$) of an existing CFD simulation with $\theta_{W,CFD} = 22.5°$. Additionally, wake 12 is formed by a canyon with a wind incidence angle of $\theta_W = 157.5°$ but is represented by a simulation with $\theta_{W,CFD} = 22.5°$ with the wind data flipped (FlipData = 1) as per the

canyon $\theta_W \rightarrow \theta_{W,CFD}$ mappings in Section 3.5. A consequence of flipping the wind data can be seen by comparing the top view of this wake (W12) with wake 6 in Figure 5.3. The buildings forming wake 6 are essentially the buildings in wake 12 mirrored about an axis aligned with the wind, resulting in a $\theta_W = 22.5$ which is represented by the same $\theta_{W,CFD}$ as wake 12 but does not require the wind data to be flipped (FlipData = 0). This results in the wake 6 shape being a mirror image of the wake 12 shape about an axis aligned with the wind.

It is the urban environment as previously described through which the aircraft is to navigate three flight paths, each defined by a series of waypoints to be followed in numerical order. For each path two flight simulations are performed for comparison purposes. One simulates aircraft flight in constant wind (neglects the presence of the buildings) and the other takes the urban winds generated by the buildings (variable wind) into account. With respect to wall-clock time, the slowest the flight simulations run is when the aircraft is flying through a wake. In this case it take an average of ~ 130 s on the wall-clock to run 0.1 s of simulation. Almost the entirety of the simulation time is taken up by the execution of the Selection Algorithm and Wind Field Analysis (more specifically, retrieving wind data from CFX-Post) blocks.

Figure 5.5 shows a top view of the Path 1 waypoints ('WP1' and 'WP2', to be followed in the order WP1 $\rightarrow$ WP2) and the aircraft ground track from just the constant wind simulation, since at this spacial resolution there is no visible difference between the constant and variable wind simulations due to the effectiveness of the tracking-hold controller. The altitude of the waypoints is 60 m and the aircraft track passes through wakes W10, W9, W8, W7 (Figure 5.3, Table 5.2) in that order. Figures 5.6a, 5.6b, and 5.6c are wind velocity vector plots of the flow around the buildings in wakes W10, W8 and W7, respectively, at $z_{CFD}/H_{CFD} = 0.5$ (where H_{CFD} is the single building or canyon height in the corresponding CFD simulation) with the aircraft path through the wake shown. A $z_{CFD}/H_{CFD} = 0.5$ is used since the aircraft altitude throughout this mission with respect to the height of the canyon and single buildings always corresponds to a z_{ENU}/H which gives $z_{CFD}/H_{CFD} \approx 0.5$ in the CFD frame. As for wake W9, Figure 5.5 reveals that the aircraft barely enters the wake windward of the building and as such the effect of this wake on aircraft flight is not a concern. Since the aircraft is flying across the wakes, the main regions of interest (as discussed previously in sections 3.4.3 and 3.5.1) are the accelerated flow around the edges of the single building or windward building (in the case

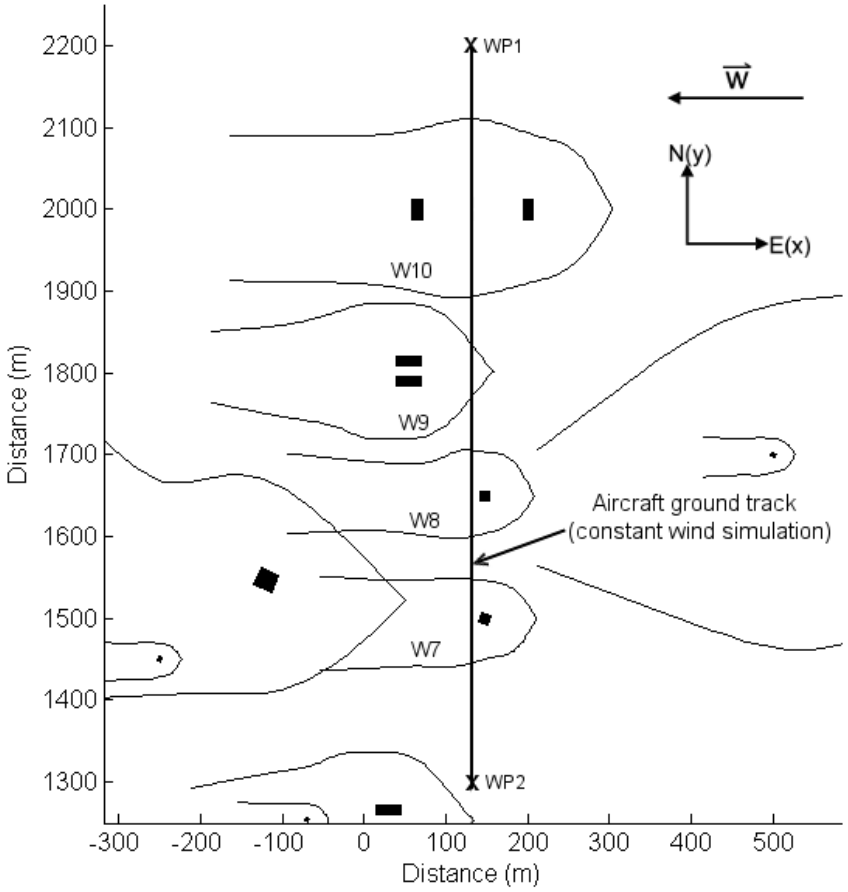

Figure 5.5: Top view of Path 1 starting at waypoint 1 ('WP1'), passing through wakes W10, W9, W8, W7 and ending at waypoint 2 ('WP2'). The aircraft ground track is from the constant wind simualtion, the difference between the constant and variable wind simulations is not visible at this resolution.

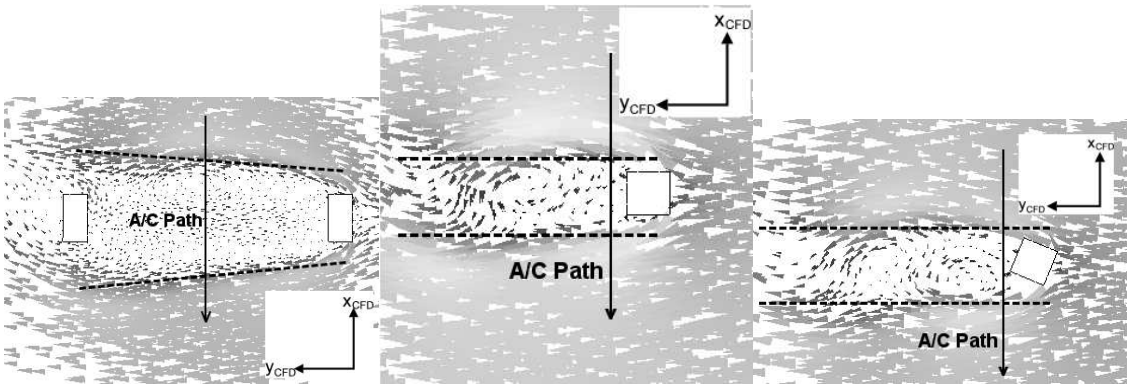

(a) Wake 10 (W10) (b) Wake 8 (W8) (c) Wake 7 (W7)

Figure 5.6: Vector plots of wind velocity in wakes along Path 1

of the canyon), the low velocity flow behind the single building or windward building, and the wind velocity gradient dv_W/dx (in the CFD frame) which forms along the 'ridges' located by the dashed lines in Figures 5.6a - 5.6c.

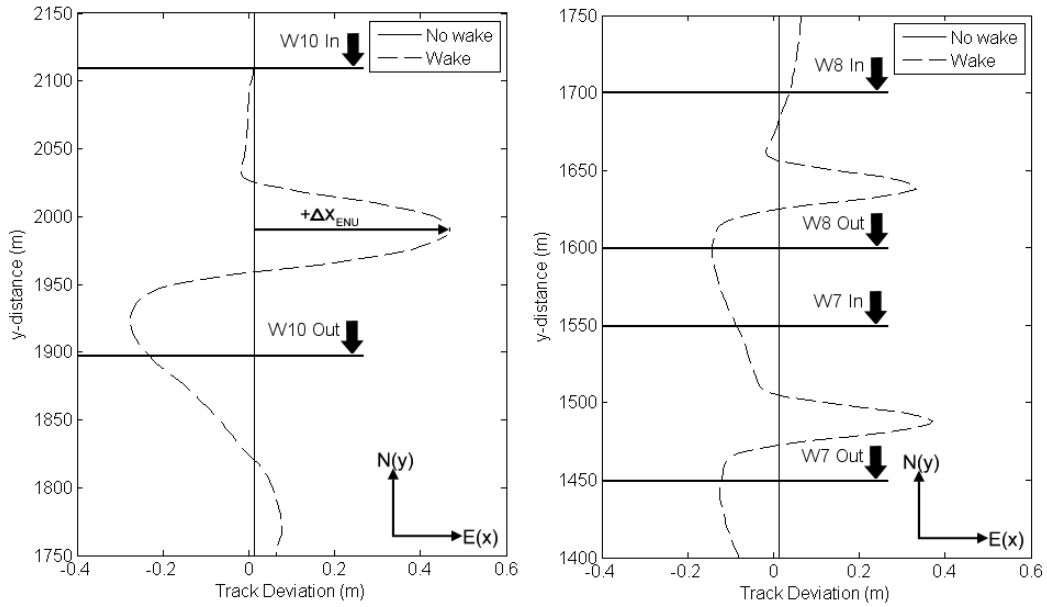

Figure 5.7: Track deviation throughout all wakes along Path 1, starting at the right of the top plot and progressing left. Positive track deviation is in the Eastern direction. Markers indicate where a given wake is entered (e.g. 'W10 In') and exited (e.g. 'W10 Out') by the aircraft.

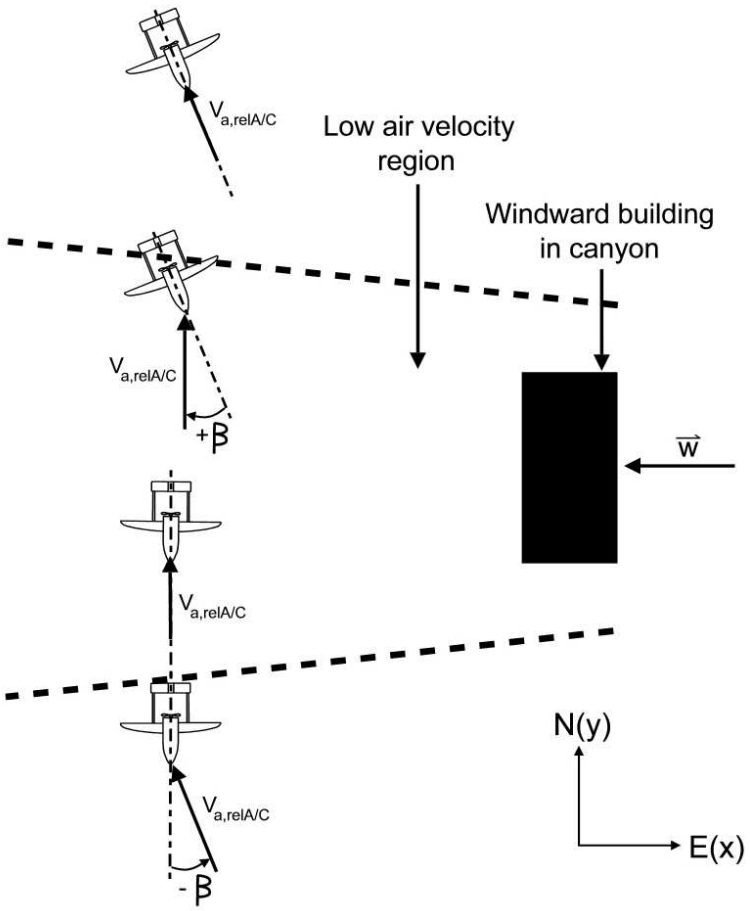

Figure 5.8: Illustration of how the low air velocity region behind a building affects aircraft sideslip β

Figure 5.7 is a detailed plot of the track deviation in the Easterly direction (Δx_{ENU}) as the aircraft passes through all the wakes along Path 1 (in the $-y_{ENU}$, Southerly, direction). The locations where the aircraft enters and exits each wake are labeled, for example the location where the aircraft enters wake 10 (first wake encountered along Path 1) is labeled 'W10 In' and the location where the aircraft exits the wake is labeled 'W10 Out'. The differences between the track deviations for constant and variable wind are all quite small, the largest being $\Delta x_{ENU} \approx 0.5$ m (~ 0.18 wing span b) in wake 10. Inside wakes 10, 8, and 7 the track deviation does not change much in the wake until the aircraft gets to the low velocity air behind the building which then causes a positive jump in Δx_{ENU} which is quickly followed by a drop in Δx_{ENU} as the low wind velocity region is exited. As illustrated by Figure 5.8, when the aircraft first enters the wake (in this case, wake 10) the fuselage is aligned with the

air velocity relative to the aircraft (includes the relative air velocity due to aircraft motion and urban wind). When the aircraft enters the strip of low velocity air the direction of the relative air velocity suddenly changes so as to form a non-zero angle with the fuselage axis (Figure 5.8) and thus creating a sideslip angle β. As illustrated in Figure 5.8, a positive change in sideslip causes an increase in aerodynamic force along the aircraft $-y_b$ axis thus pushing the aircraft in the Eastern direction and thereby accounting for the initial increase in Δx_{ENU} seen in Figure 5.7. The subsequent drop in Δx_{ENU} is due to the reverse of the situation previously described. Inside the low velocity strip of air the fuselage eventually aligns itself with the relative air velocity (Figure 5.8) and then when the low air velocity region is exited the sideslip angle β decreases causing a force on the aircraft in the Westerly direction and thus giving rise to the $-\Delta x_{ENU}$ seen in Figure 5.7.

The Δx_{ENU} plots in wakes 8 and 7 show the same basic pattern and the plot in wake 10 is similar except that the increase and subsequent decrease of Δx_{ENU} are larger. The larger increase in wake 10 is due to the fact that the low velocity air region in wake 10 is wider along the aircraft path than wakes 8 or 7 (which means the aircraft is spending longer in this region) and due to the recirculation in the middle of the wake (Figure 5.6a) along the aircraft flight path which is directed back towards the windward building and pushes the aircraft further in the $+\Delta x_{ENU}$ direction (in addition to the effect of the low velocity air region as illustrated in Figure 5.8). Recirculation of this strength is not observed along the aircraft path through wakes 8 and 7 (Figures 5.6b and 5.6c). The larger decrease in Δx_{ENU} from wake 10 as opposed to wakes 8 and 7 is likely due to a stronger autopilot response to the larger Δx_{ENU} increase.

Figure 5.9 is a detailed plot of the altitude deviation Δz_{ENU} from the constant waypoint altitude of 60 m. Due to the effectiveness of the autopilot, the differences between the altitude deviations for constant and variable wind are quite small with the largest being $\Delta z_{ENU} \approx 0.13$ m ($\sim 0.05b$) in wake 10. The most noticable deviations are caused by the region of low velocity air and the surrounding ridges of accelerated flow (dashed lines in Figures 5.6a - 5.6c), and a common pattern is shared between wakes 10, 8, and 7 as the aircraft moves through the wakes (right to left in Figure 5.9). Using wake 10 as an example, just before the aircraft enters the region of low velocity air it encounters a ridge of accelerated flow which causes an increase in lift due to the increase in relative air velocity, causing an increase in altitude ('Altitude

Increase 1', peak 'A' in Figure 5.9). As the aircraft moves into the low velocity region there is a subsequent drop in altitude ('Altitude Drop 1') due to the decrease in relative air velocity, then another altitude increase as the aircraft exits the low velocity region into the second ridge of accelerated flow ('Altitude Increase 2', peak B). Finally an altitude drop ('Altitude Drop 2') occurs due to the joint effect of the aircraft moving out of the accelerated flow region into constant background wind conditions and the autopilot working to reduce the altitude from its previous high ('Altitude Increase 2'). The double peak pattern is also shown in Figure 5.9 for both wakes 7 and 8 as well.

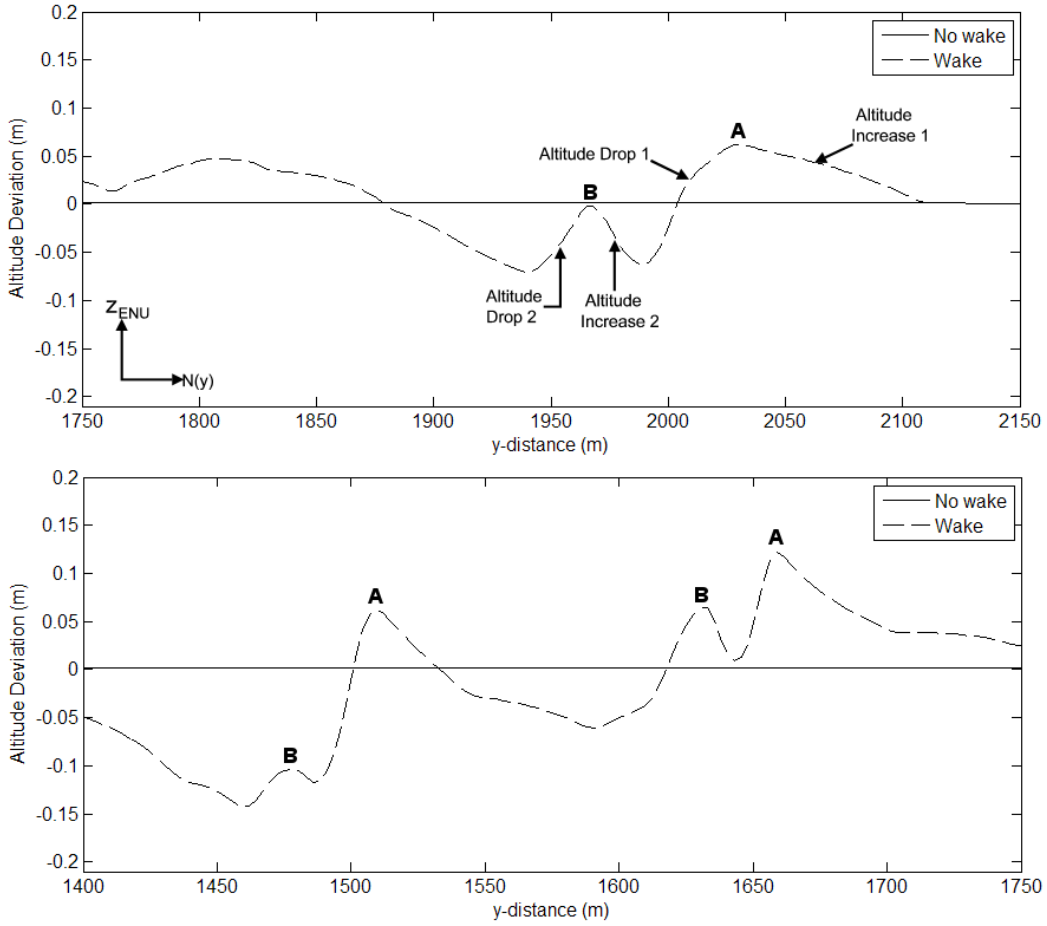

Figure 5.9: Altitude deviation throughout all wakes along Path 1, starting at the right of the top plot and progressing left. Markers indicate where a given wake is entered and exited by the aircraft.

Overall the track and altitude deviations are small, all less than a fifth of the aircraft wing span b. Additionally, the aircraft bank angle θ_{bank}, relative heading θ_{relH}, and pitch angle θ_{pitch}

stay within $-6° < \theta_{bank} < 6°$, $-5° < \theta_{relH} < 12°$, and $0° < \theta_{pitch} < 5°$ respectively. More significant deviations would be expected if (1) the background wind velocity was increased, as this would generally increase the wind velocity gradients (2) the aircraft weight is reduced as this would provide less inertial resistance to forces and moments due to urban winds and (3) the building scale was increased and/or the aircraft speed decreased, as this would allow the aircraft to spend more time inside regions with large wind gradient values. Given that current aircraft forward speed is ∼25 m/s and the width of the low velocity region plus the surrounding ridges in wake 10 (the widest of the three wakes) along the aircraft path is ∼ 2.5 building lengths (2.5 × 24.12 m = 60.3 m) the aircraft is only being directly affected by the wake for ∼60.3 m/25 m/s ≈ 2.4 s.

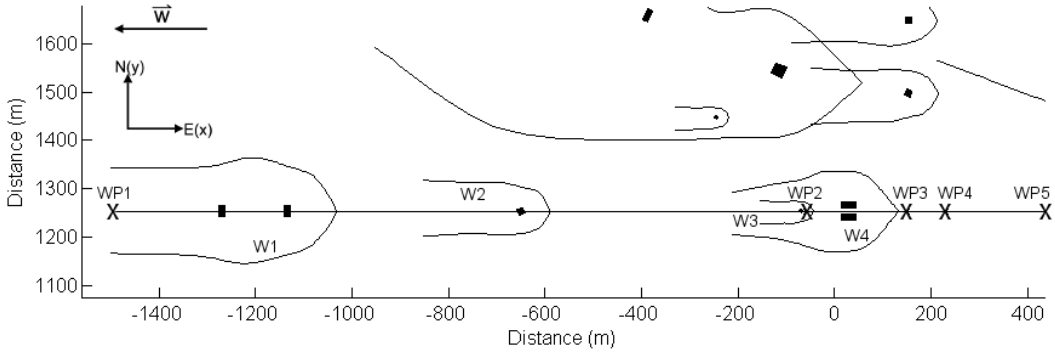

Figure 5.10: Top view of Path 2 starting at waypoint 1 ('WP1'), passing through wakes W1, W2, and W4 and ending at waypoint 5 ('WP5'). The aircraft ground track is from the constant wind simulation, the difference between the constant and variable wind simulations is not visible at this resolution.

Figure 5.10 shows a top view of the Path 2 waypoints to be followed and the aircraft track from the constant wind (solid line) and variable wind (dashed line) simulations (where again at this resolution no difference can be distinguished between the two). The altitude of the waypoints varies, with waypoints WP1, WP2 having an altitude of 110 m and WP3, WP4, WP5 having an altitude of 65 m. Figure 5.11a is a sideview of Path 2 showing the aircraft passing over the various buildings where it can be seen that the aircraft passes through a large portion of wake 1 (Figure 5.11b) but only a small portion of wake 2, illustrating the importance of the vertical wake profile. Wake 3 is completely contained inside wake 4 but since the aircraft passes over wake 3 the Selection Algorithm does not find any problems (recall that the aircraft

can only be in one wake at a time in order for the Selection Algorithm to determine which single building or canyon, if any, influences the flow local to the aircraft otherwise it outputs a 'NO SOLUTION' result indicating in this case a more sophisticated CFD database entry is required such as a 3 building simulation). The locations of the waypoints are such that the aircraft is required to descend down to 65 m from 110 m while flying in between the buildings in wake 4.

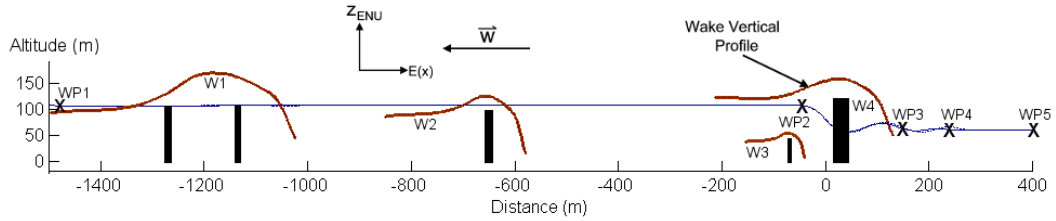

(a) Sideview of Path 2 in its entirety

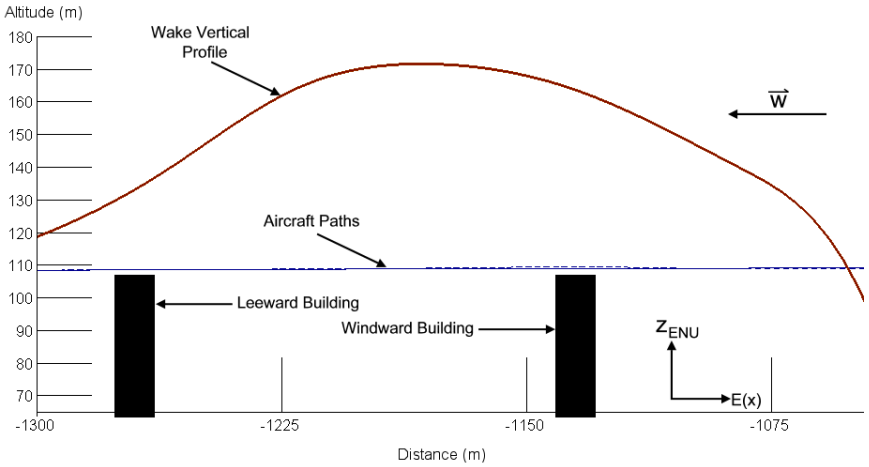

(b) Close up of Path 2 over the buildings in wake 1

Figure 5.11: Side view of Path 2. The constant wind simulation is represented by the solid line and the variable wind simulation is represented by the dashed line. All other buildings in the environment other than those responsible for wakes W1-W4 are omitted for clarity.

Figures 5.12a and 5.12b are wind velocity vector plots of the flow over the buildings in wakes 1 and 2, taken from a plane passing through the canyon or single building centroid and aligned with the background wind. The region of interest from these plots is the flow above rooftop level, along the aircraft path. Also provided are Figures 5.13a and 5.13b which show the effects of the flow visualized in Figures 5.12a and 5.12b on the aircraft's altitude compared with the constant wind simulation. As the aircraft enters wake 1 (labeled 'W1 In' in Figure

5.13a) downwind of the leeward building, it encounters slightly negative vertical wind velocities (Figure 5.12a) caused by the flow curling around the top of the leeward building resulting in an initial small drop in aircraft altitude, as shown in Figure 5.13a. Followed by this small drop in altitude is a small increase in altitude as the aircraft flies over the leeward building and encounters slightly increased vertical wind motions as the air is rushing over the top of the building (Figure 5.12a). As the aircraft moves past the leeward building and continues its flight between the two buildings in the canyon it first encounters negative vertical motions (much larger than those encountered downwind of the leeward building) due to flow recirculation (as previously discussed in section 3.5) inside the canyon and then a region of low velocity air just downwind of the windward building, as shown in Figure 5.12a, both of which result in a drop in aircraft altitude. Although in this simulation the aircraft flight is accomplished without incident, it should be noted that for higher wind speeds the recirculation may be strong enough to push the altitude below rooftop level such that the autopilot is not powerful enough to get the aircraft back above rooftop level before the windward building is reached. As the aircraft arrives over the windward building the vertical air motions caused by the flow rushing over the windward building (much more significant than for the leeward building) push the aircraft upwards, increasing altitude.

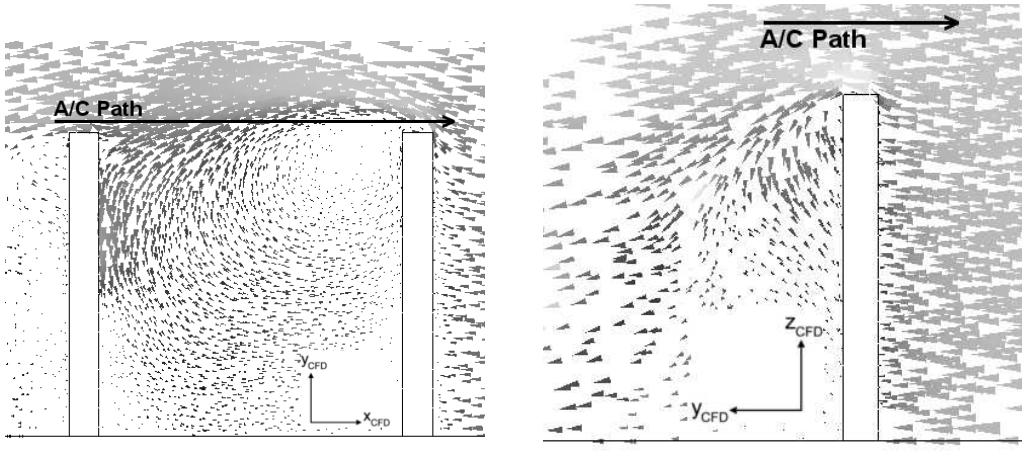

(a) Wake 1 (W10) (b) Wake 2 (W2)

Figure 5.12: Vector plots of wind velocity over buildings in wakes 1 and 2 along Path 2

As the aircraft flies over the single building in wake 2 the altitude plot (Figure 5.13b) shows only a very slight increase in altitude due to the vertical air motions over the building. These

motions are smaller in magnitude than those over the windward building in wake 1 (due to the lack of a recirculation zone as seen in the canyon configuration) and the aircraft is flying further above rooftop level of the building in wake 2 than the buildings in wake 1 (recall from Figure 5.11a that the aircraft only just passes through this wake).

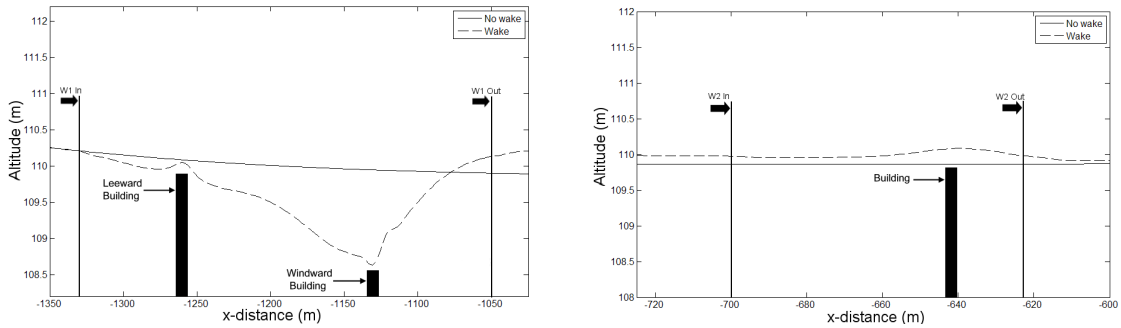

(a) Altitude deviation through wake 1

(b) Altitude deviation over the single building in wake 2

Figure 5.13: Detailed plots of altitude deviation over the two buildings in wake 1 and the single building in wake 2. The buildings in the Figures are simply position markers and as such their dimensions and relative height do not represent reality (the buildings in wake 1 are actually the same height).

Figure 5.14 is a vector plot of the wind velocity taken from the CFD simulation which represents the flow around the buildings in wake 4, taken from a horizontal plane at $H_{CFD}/z_{CFD} = 0.5$. As illustrated in Figure 5.11a the altitude is not constant throughout wake 4 owing to the fact that waypoints 2 and 3 are at different altitudes, however the vector plot at $H_{CFD}/z_{CFD} = 0.5$ is a good representation of the flow the aircraft experiences while flying just downwind of the two buildings and in between the buildings. This is the region of main interest since the flow is being accelerated through the canyon due to a venturi-like effect (discussed previously in Section 3.5) which works to increase aircraft altitude while the autopilot is working to decrease altitude to reach waypoint 3. The results of this dynamic is illustrated in Figure 5.15. Oscillations in aircraft altitude are observed for both the constant and variable wind simulations due to the action of the autopilot attempting to decrease altitude as the aircraft is flying directly into the wind. As expected, the aircraft altitude for the variable wind simulation (dotted line) is generally kept slightly higher than for the constant wind simulation (solid line) with effects lasting after the region of accelerated flow is exited. The largest difference between the variable and constant wind simulations is ~ 2.5 m ($\sim 0.88b$).

As previously discussed, simulations with larger buildings, higher wind speeds and an aircraft with a lower stall speed or weight would result in more significant effects due to urban wind.

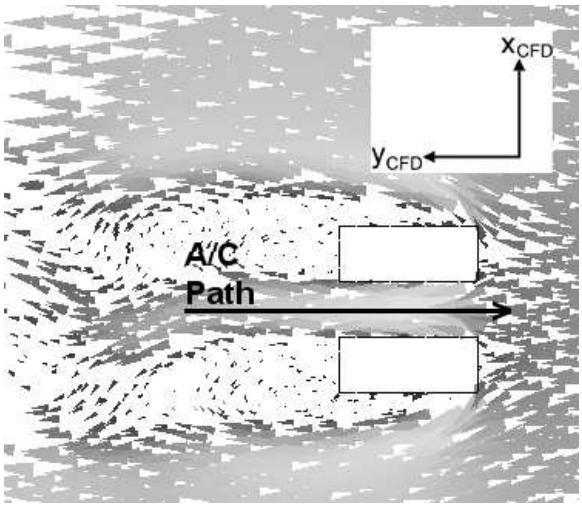

Figure 5.14: Vector plot of wind velocity around bulidings in wake 4

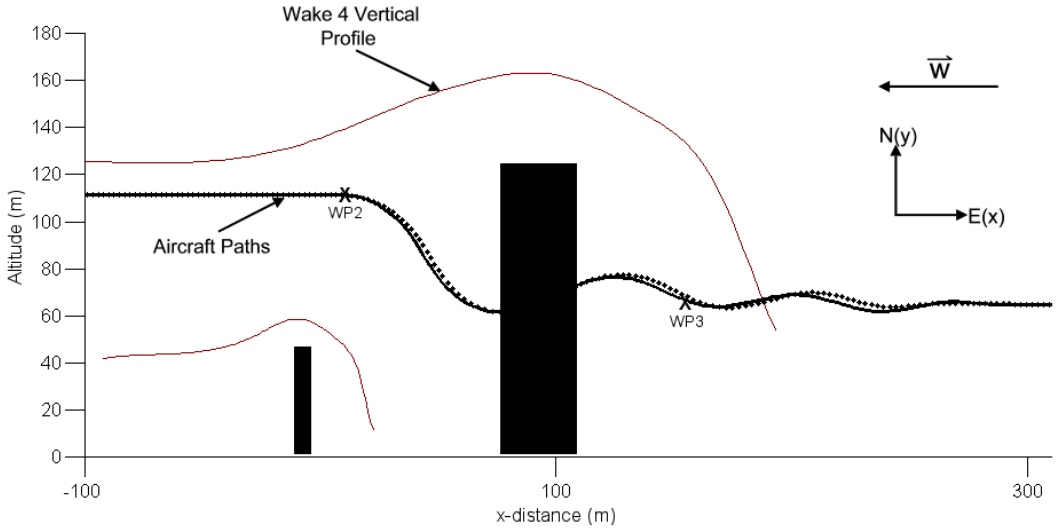

Figure 5.15: Aircraft altitude through the buildings in wake 4, switching from waypoint 2 (altitude = 110 m) to waypoint 3 (altitude = 65 m). The variable wind simulation is represented by the dotted line and the constant wind simulation is represented by the solid line.

A top view and three-dimensional view of the Path 3 waypoints and the aircraft track from the constant wind (solid line) and variable wind (dashed line) simulations are provided by Figures 5.16 and 5.17. The aircraft passes through wakes 6, 9, and 13 and the altitude of the

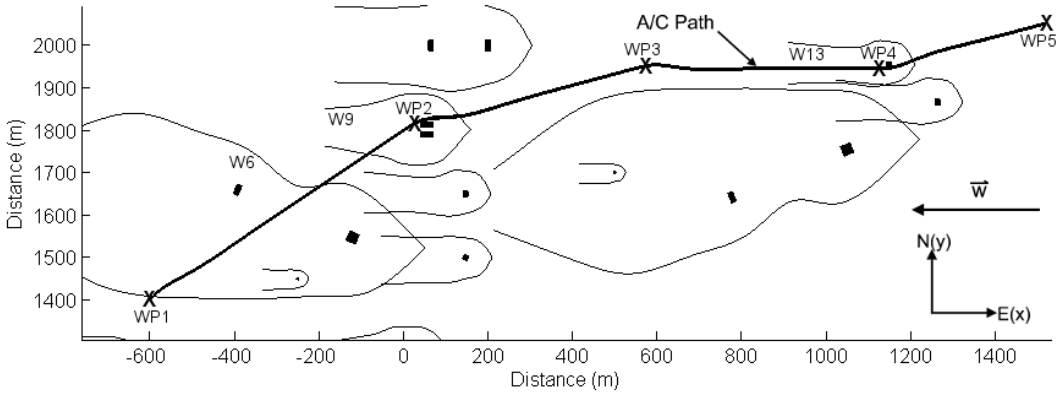

Figure 5.16: Top view of Path 3 starting at waypoint 1 ('WP1'), passing through wakes W6, W9, and W13 and ending at waypoint 5 ('WP5')

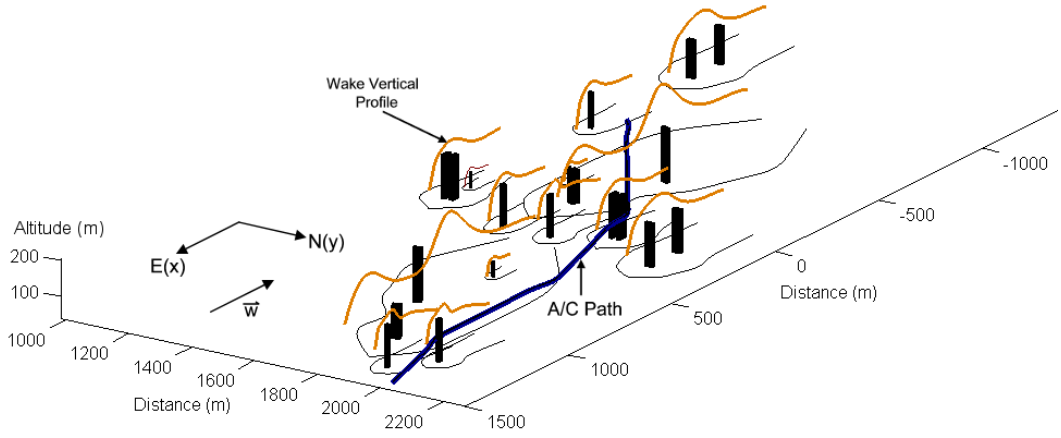

Figure 5.17: Three-dimensional view of Path 3

waypoints is constant at 65 m. At the resolution of Figures 5.16 and 5.17 no difference can be discerned between the constant and variable wind simulation paths. Additionally, the aircraft path looks as though it collides with the Northernmost building in wake 9 (B13, Table 5.1) and the single building in wake 13.

Figure 5.18 is a close-up of the variable wind (dashed line) and constant wind (solid line) simulation aircraft tracks with the aircraft fuselage and wing axes superimposed on the variable wind track, where the length of the axes shown are $\sim 3\times$ larger than in reality. The flow the aircraft experiences in the wake is the same as the wind velocity vector plot shown previously in Figure 5.14 during the discussion of flight along Path 2 through wake 4. As shown in Figure 5.18, after waypoint 2 has been checked the aircraft has to turn further to the East to track

waypoint 3, and combined with the fact that the accelerated flow around the North side of the Northerly building in wake 9 (Figure 5.14) helps push the aircraft Westward, a small deviation ($\sim$ 1 m) between the variable and constant wind tracks results.

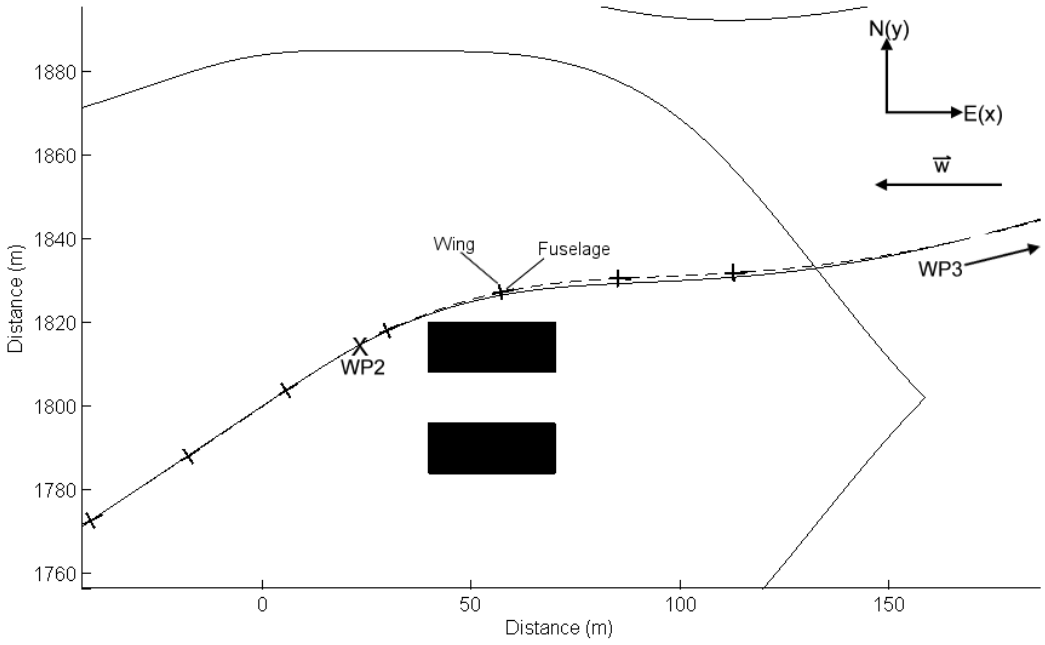

Figure 5.18: Close-up of the aircraft paths (variable wind path is dashed, constant wind path is solid) past the buildings in wake 9. The aircraft nose is at the end of the fuselage axis which is farther from the wing axis, and the length of the axes shown are $\sim$3$\times$ larger than in reality.

Figure 5.19 shows the aileron and elevator deflections prescribed by the autopilot just before and after waypoint 2 is checked by the aircraft (black dots locate when the waypoint is checked). The stress that the canyon wake puts on the autopilot with respect to aileron control (Figure 5.19a) is overshadowed by the aileron deflections prescribed just after WP2 is checked (the aileron deflection rate is near the maximum rate of 45°/s), when the autopilot is adjusting to the new Waypoint Navigation Vector (WNV). However, the presence of the canyon wake does put noticeably more stress on the autopilot with respect to elevator control than does a constant wind field (Figure 5.19b). The maximum elevator deflection rate in the variable wind plot is $\sim$ 0.75 of the maximum elevator rate of 45°/s). In this case the autopilot does not need to work the elevator too hard to follow the new WNV since WP2 and WP3 are at the same altitude.

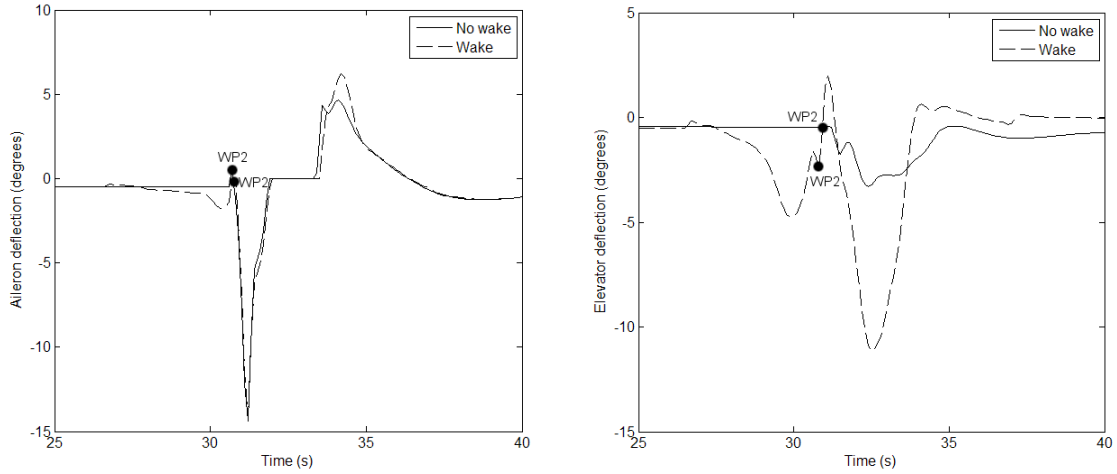

(a) Aileron deflection through wake 9

(b) Elevator deflection through wake 9

Figure 5.19: Aileron and elevator deflection through wake 9. The approximate times when waypoint 2 is checked for the constant and variable wind simulations are located by black dots labeled 'WP2'.

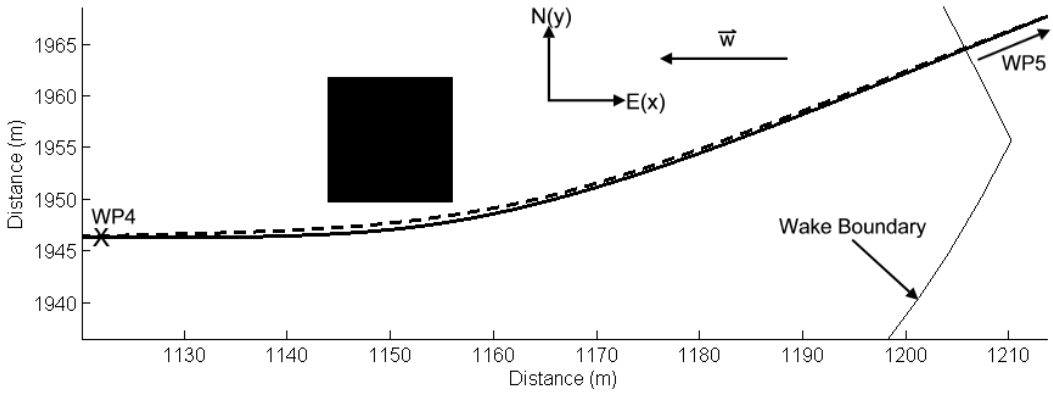

Figure 5.20: Close-up of aircraft paths (variable wind path is dashed, constant wind path is solid) past the building in wake 13

Figure 5.20 shows the variable and constant wind aircraft tracks as the aircraft turns around the single building in wake 13 to track waypoint 5. What is significant here is not necessarily the magnitude of the difference between tracks (only about $\sim$1 m $\approx 0.35b$) but the direction in which the variable wind track differs from the constant wind track. The variable wind track is moved closer to the building and therefore suggests that with higher wind speeds and larger buildings this path through the urban environment is potentially dangerous since the aircraft could be pushed into the building. The reason the aircraft moves closer to the building is illustrated by Figures 5.21 and 5.22. Figure 5.21 shows the aircraft axes from the variable

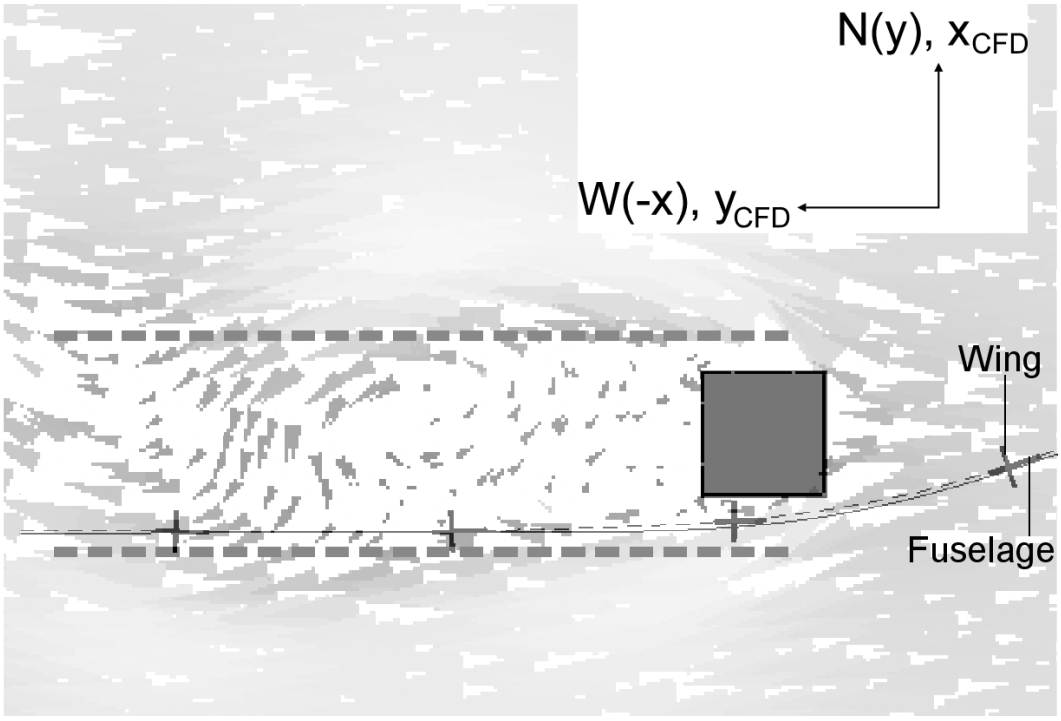

Figure 5.21: Aircraft axes superimposed on a vector plot of the wind velocity around the single building in wake 13 (aircraft $\sim$3$\times$ scale)

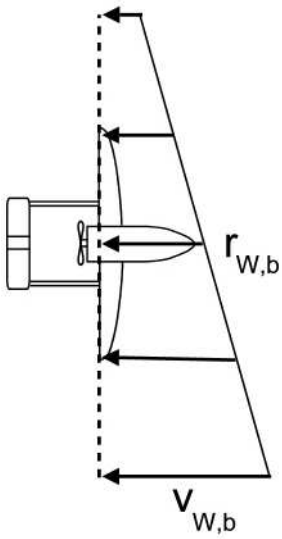

Figure 5.22: Linear velocity distribution ($v_{W,CFD}$) along aircraft wing due to aircraft orientation in wake 13 (Figure 5.21), resulting in a -ve effective yaw rate -$r_{W,b}$

wind simulation superimposed on the vector plot of the wind velocity from the CFD simulation representing the flow in wake 13, as previously shown in Figure 5.6b for Path 1 through wake 8

(wake 8 and wake 13 are represented by the same CFD simulation). As the aircraft approaches and flies beside the building it is flying approximately along the ridge (dashed line) between the accelerated flow around the sides of the building and the low velocity region downwind of the building. In this orientation, there is a steamwise wind velocity gradient setup along the aircraft wing axis due to the large $dv_{W,CFD}/dx$ along the ridge. As illustrated by Figure 5.22 such a velocity distribution results in an effective yaw rate (-ve) as per the 4-point model previously discussed in Section 4.4. The dynamics of the aircraft are such that a negative raw rate causes the aircraft to bank in the $-\theta_{bank}$ direction (Figure 4.7), and combining this with the fact that the autopilot is required to bank the aircraft in the same direction to produce a force in the Northerly direction in order to track waypoint 5 (Figure 5.20), the aircraft is pushed closer to the building than it would be in the case of constant wind. This suggests that for such an aircraft flight path the autopilot should be tuned such that aileron deflections which push the aircraft in the direction of the building are less aggressive, for example allowing the aircraft to temporarily drift off the desired track away from the building.

Figure 5.23 shows the aileron and elevator deflections prescribed by the autopilot just before and after waypoint 4 is checked by the aircraft. It should be noted that by this time in the flight simulation the time plots of the control surface deflections for constant and variable wind are slightly offset due to small differences in the flight path. The prescription of aileron deflections (Figure 5.23a) is again dominated by the acquisition of a new WNV after WP4 is checked (the aileron deflection rate is near the maximum of 45°/s). However, the building wake does make a slight contribution; in the variable wind simulation, just before WP4 is checked, a fairly sharp aileron deflection in the negative direction is prescribed to oppose the negative roll moment caused by the aircraft flying along the 'ridge' of the wake, as previously discussed. The presence of the building wake puts noticeably more stress on the autopilot with respect to elevator control than does a constant wind field (Figure 5.23b, the maximum elevator deflection rate in the variable wind plot just before and after WP4 is checked is near the maximum rate). As was the case when checking WP2 in wake 9, the autopilot does not need to work the elevator too hard since WP4 and WP5 are at the same altitude.

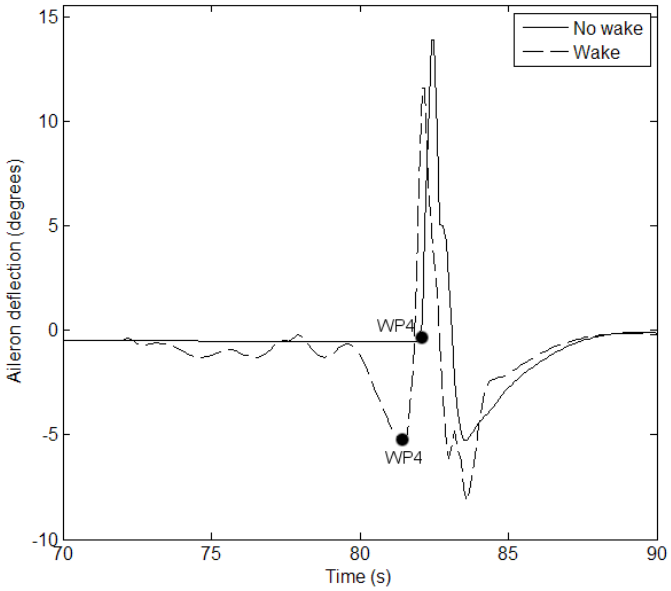

(a) Aileron deflection through wake 13

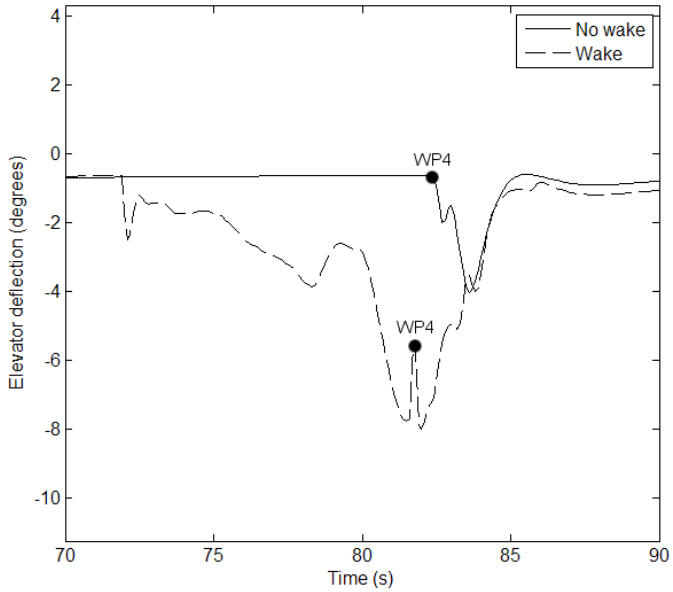

(b) Elevator deflection through wake 13

Figure 5.23: Aileron and elevator deflection through wake 13. The approximate times when waypoint 4 is checked for the constant and variable wind simulations are located by black dots labeled 'WP4'.

Chapter 6

Conclusions/Recommendations

Motivated by potential reconnaissance, surveillance, human-risk reduction, military, and law enforcement applications of a UAV in urban areas, a first generation methodology is presented which allows for the prediction of aircraft performance in an urban environment. However, instead of simulating the airflow in an entire urban area of interest, the urban area is considered to be composed of discrete single buildings and canyons, around which the flow is relatively straightforward to simulate. In addition, the general characteristics of single building and canyon flow have been extensively studied and are well understood. Under assumptions about urban geometry and wind, a Selection Algortihm is presented which determines which single buildings or canyons influence the flow local to the aircraft at a given location through the use of building and canyon wake shapes. The wind data corresponding to the single buildings and canyons which influence the flow around the aircraft during a mission is retrieved from a wind simulation database (WSD) of completed CFD simulations and interfaced with a dynamic Simulink model of the Aerosonde UAV. A basic autopilot and waypoint navigation system is added to the dynamic model which is then used to simulate flight of the Aerosonde UAV in an urban environment to demonstrate the predictive capabilities of the methodology.

The mesh used to obtain CFD results does not show global grid convergence for the test case. However, signficant regions of the flow (specifically rooftop shear stress and the velocity gradients seperating the low velocity strip of air from the surrounding flow) strongly suggest that convergence could be achieved with a subsequent refinement. These regions themselves show clear convergence as the mesh is refined from coarse to fine. The validation case matches

the trends of the experimental data well enough such that confidence is placed in the ability of the CFD solver (Ansys CFX) to capture the critical features of the single building and canyon flows under investigation. In agreement with established theory, the CFD simulations of single building flows exhibit recirculation patterns such as vortex shedding and vortices are clearly observed in the canyon CFD simulations with $S/H = 1$ (skimming flow).

The results of the flight simulations are found to be consistent with the characteristics of the flow around the building structures and provide insight into the effects that buildings have on flight performance. Given the scale of the buildings, background wind speed, size and speed of the Aerosonde UAV, and the effectiveness of the autopilot, it is observed that disruptions to the flight of the Aerosonde UAV caused by the flow around single buildings and canyons is minimal (on the order of about half a wing span b). However, the presence of the building wakes requires the work rate of the control surfaces to be significantly higher, in particular that of the elevator. Performing simulations of aircraft flight using buildings of a much larger scale, similar to buildings in downtown areas of major North American cities, with a higher background wind speed would produce more significant flight path deviations. Implementing the methodology with a smaller air vehicle such as a MAV would increase flight path deviations as well (it is lighter and has a lower cruising speed than a UAV). Nonetheless, the simulations reveal potentially dangerous flight paths, particularly when the aircraft is heading directly into the background wind while turning around a building or flying closely over a rooftop.

Further development of the first generation methodology involves building up the single building and canyon simulation databases, starting with the geometries in the First Generation Geometry Configuration Set. Additional research into urban building geometries and canyon flow patterns would aid in choosing more simulations (i.e. choice of Re, geometry, wind incidence) with which to fill the databases. In particular, simulations with higher Re (achieved by either increasing the background wind speed, building scale, or both) are desired. For a given CFD simulation, a higher Re allows the building to be scaled to larger dimensions during flight simulation through Re matching. As previously discussed, for moderate wind speeds of ~ 4 m/s the single buildings and canyons in the current database can only be scaled to dimensions much smaller than those of typical buildings in downtown areas. Additional developments to the methodology aside from building up the single building and canyon simulation databases

would be considered as contributing to a second generation of the methodology. For example, the current Selection Algorithm checks every wake in the urban environment at every time step to see which wakes contain the aircraft. The algorithm would be much more efficient if it were modified so that it would only check single building or canyon wakes which are less than a predefined distance from the position of the aircraft (i.e. wakes which have a chance of containing the aircraft). The wind simulation database would benefit from a more thorough grid convergence study and validation, and an investigation of the flow field well past $t = 20$ s. A more realistic autopilot should be implemented, one which models control surface lag and uses coupled deflections (i.e. where both ailerons and rudder are used to control aircraft track). Most significantly, a second generation methodology would include CFD simulations of urban geometries with more than two buildings, requiring additional research into which 2+ building simulations generate significant winds and ways of dealing with denser urban environments (for example, if the aircraft is found in two wakes it may be possible that one wake dominates the flow local to the aircraft to such an extent that the other wake may be ignored).

Bibliography

[1] T. Hegazy, B. Ludington, G. Vachtsevanos, "Reconnaissance and Surveillance in Urban Terrain with Unmanned Aerial Vehicles", *Norweigian University of Science and Technology Publication*, 2004.

[2] K. Mullens, E. Pacis, S. Stancliff, A. Burmeister, T. Denewiler, M. Bruch and H.R. Everett, "An Automated UAV Mission System", *AUVSI Unmanned Systems in International Security 2003 (USIS 03)*, London, England, September 9-12, 2003.

[3] D. Murphy, J. Cycon, "Applications for mini VTOL UAV for law enforcement", *SPIE Proc. 3577: Sensors, C3I, Information, and Training Technologies for Law Enforcement*, Boston, MA, November 3-5, 1998.

[4] M. Peot, T. Altshuler, A. Breiholz, R. Bueker, K. Fertig, A. Hawkins and S. Reddy, "Planning sensing actions for UAVs in urban domains", *SPIE Europe Symposium on Optics/Photonics in Security Defence*, September 26-28, 2005.

[5] P. Pettersson, P. Dohertya, "Probabilistic Roadmap Based Path Planning for an Autonomous Unmanned Aerial Vehicle", *Proceedings of the ICAPS Workshop on Connecting Planning and Theory with Practice*, 2004.

[6] R. Prazenica, A. Kurdila, R. Sharpley and J. Evers, "Vision-Based Geometry Estimation and Receding Horizon Path Planning for UAVs Operating in Urban Environments", *Proceedings of the 2006 American Control Conference*, Minneapolis, Minnesota, USA, June 14-16, 2006, 2004.

[7] D. Shim, H. Chung, H. Kim and S. Sastry, "Autonomous Exploration in Unknown Urban Environments for Unmanned Aerial Vehicles", *AIAA Guidance, Navigation, and Control Conference and Exhibit*, San Francisco, California, August 15 - 18, 2005.

[8] W. Theurer, "Typical building arrangements for urban air pollution modelling", *Atmospheric Environment*, vol. 33, 1999.

[9] R. K. Arning, S. Sassen, "Flight Control of Micro Aerial Vehicles", *AIAA Guidance, Navigation and Control Conference and Exhibit*, Providence, Rhode Island, August 16 - 19, 2004.

[10] J. Boris, "Dust in the Wind: Challenges for Urban Aerodynamics", *35th AIAA Fluid Dynamics Conference and Exhibit*, Toronto, Ontario Canada, June 6 - 9, 2005.

[11] M. Bottema, "Urban Roughness Modelling in Relation to Pollutant Dispersion", *Atmospheric Environment*, vol. 31, 1997.

[12] R. Britter, S. Hanna, "Flow and Dispersion in Urban Areas", *Annual Review of Fluid Mechanics*, Annual Reviews, 2003.

[13] C. Chang, R. Meroney "Concentration and flow distributions in urban street canyons: wind tunnel and computational data", *Journal of Wind Engineering and Industrial Aerodynamics*, vol. 91, 2003.

[14] M. Bottema, "Urban Roughness Modelling in Relation to Pollutant Dispersion", *Atmospheric Environment*, vol. 31, 1997.

[15] P. Kastner-Klein, R. Berkowicz, and R. Britter, "The influence of street architecture on flow and dispersion in street canyons", *Meteorology and Atmospheric Physics*, vol. 87, 2004.

[16] L. Hunter, I. Watson and G. Johnson, "Modelling Air Flow Regimes in Urban Canyons", *Energy and Buildings*, vol. 15, 1990, vol. 16, 1991.

[17] S. Murakami, R. Ooka, A. Mochida, S. Yoshida and S. Kim, "CFD analysis of wind climate from human scale to urban scale", *Journal of Wind Engineering and Industrial Aerodynamics*, vol. 81, 1999.

[18] E. Plate, "Methods of Investigating Wind Fields - Physical Models", *Atmospheric Environment*, vol. 33, 1999.

[19] Z. Sorbjan, M. Uliasz "Some Numerical Urban Boundary-Layer Studies", *Boundary-Layer Meteorology*, vol. 22, 1982.

[20] J. Counihan, "Simulation of an Adiabatic Urban Boundary Layer in a Wind Tunnel", *Atmospheric Environment*, vol. 7, 1973.

[21] P. Hildebrand, B. Ackerman, "Urban Effects on the Convective Boundary Layer", *Journal of the Atmospheric Sciences*, vol. 41, 1983.

[22] A. Martilli, "Numerical Study of Urban Impact on Boundary Layer Structure: Sensitivity to Wind Speed, Urban Morphology, and Rural Soil Moisture", *Journal of Applied Meteorology*, vol. 41, 2002.

[23] G. Patnaik, J. Boris, F. Grinstein and J. Iselin, "Large Scale Urban Simulations with FCT", *Scientific Computation*, 2005.

[24] G. Panaik, J. Boris and F. Grinstein, "Large Scale Urban Simulations with the MILES Approach", *16th AIAA Computational Fluid Dynamics Conference*, Orlando, Florida, June 23-26, 2003.

[25] J. He, C. Song, "Evaluation of pedestrian winds in urban area by numerical approach", *Journal of Wind Engineering and Industrial Aerodynamics*, vol. 81, 1999.

[26] P. Neofytou, A.G. Venetsanos, D. Vlachogiannis, J.G. Bartzis, A. Scaperdas, "CFD simulations of the wind environment around an airport terminal building", *Environmental Modelling Software*, vol. 21, 2006.

[27] P. Oliveira, B. Younis, "On the prediction of turbulent flows around full-scale buildings", *Journal of Wind Engineering and Industrial Aerodynamics*, vol. 86, 2000.

[28] A. Baskaran, A. Kashef, "Investigation of air flow around buildings using computational fluid dynamics techniques", *Engineering Structures*, vol. 18, 1996.

[29] J. Baik J. Kim, "A Numerical Study of Flow and Pollutant Dispersion Characteristics in Urban Street Canyons", *Journal of Applied Meteorology*, vol. 38, 1998.

[30] C. Chang, R. Meroney, "Numerical and physical modeling of bluff body flow and dispersion in urban street canyons", *Journal of Wind Engineering and Industrial Aerodynamics*, vol. 89, 2001.

[31] A. Kovar-Panskus, P. Louka, J. Sini, E. Savory, M. Czech, A. Abdelqari, P.G. Mestayer and N. Toy, "Influence of Geometry on the Mean Flow Within Urban Street Canyons: A Comparision of Wind Tunnel Experiments and Numerical Simulations", *Water, Air, and Soil Pollution: Focus*, vol. 2, 2002.

[32] D. Lakehal, W. Rodi, "Calculation of the flow past a surface-mounted cube with two-layer turbulence models", *Journal of Wind Engineering and Industrial Aerodynamics*, vol. 67 68, 1997.

[33] R. Martinuzzi, C. Tropea, "The flow around surface-mounted prismatic obstacle placed in a fully developed channel flow", *Journal of Fluids Engineering*, vol. 115, 1993.

[34] R. Meroney, B. Leitl, S. Rafailidis and M. Schatzmann, "Wind-tunnel and numerical modeling of flow and dispersion about several building shapes", *Journal of Wind Engineering and Industrial Aerodynamics*, vol. 81, 1999.

[35] Oke TR, "Street design and the urban canopy layer climate" *Energy and Buildings*, vol. 11, 1988.

[36] W. Smith, J. Reisner and C.Y.J. Kao, "Simulations of Flow Around a Cubical Building: Comparison with Towing-Tank Data and Assessment of Radiatively Induced Thermal Effects", *Atmospheric Environment*, 2001.

[37] F. Lien, E. Yee, "Numerical Modelling of the Turbulent Flow Developing Within and Over a 3-D Building Array, Part I: A High-Resolution Reynolds-Averaged Navier-Stokes Approach", *Boundary-Layer Meteorology*, vol. 112, 2004.

[38] Y. Zhang, S. Arya and W. Snyder, "A Comparison of Numerical and Physical Modeling of Stable Atmospheric Flow and Dispersion Around a Cubical Building", *Atmospheric Environment*, vol. 30, 1996.

[39] L. Muratet, S. Doncieux and J. Meyer, "A biomimetic reactive navigation system using the optical flow for a rotary-wing UAV in urban environment", *Proceedings of ISR2004*, Paris, 2004.

[40] M. Orr, S. Rasmussen, E. Karni and W. Blake, "Framework for Developing and Evaluating MAV Control Algorithms in a Realistic Urban Setting", *2005 American Control Conference*, Portland, OR, USA, June 8-10, 2005.

[41] B. Stoor, S. Pruett and M. Duquette, "Urban Simulation Environment", *AIAA Modeling and Simulation Technologies Conference and Exhibit*, Keystone, Colorado, August 21-24, 2006.

[42] B. Etkin, "Turbulent Wind and Its Effect on Flight", *AIAA Journal*, vol. 18, 1981.

[43] J. Jang, C. Tomlin, "Autopilot Design for the Stanford DragonFly UAV: Validation through Hardware-in-the-Loop Simulation", *AIAA Guidance, Navigation, and Control Conference and Exhibit*, Montreal, Canada, August 6-9, 2001.

[44] S. Rasmussen, P. Chandler, "MultiUAV: A Multiple UAV Simulation for Investigation of Cooperative Control", *Proceedings of the 2002 Winter Simulation Conference*, 2002.

[45] L. Singh, J. Plump, M. McConley and B. Appleby, "Software Enabled Control: Autonomous Agile Guidance and Control for a UAV in Partially Unknown Urban Terrain", *AIAA Guidance, Navigation, and Control Conference and Exhibit*, Austin, Texas, August 11-14, 2003.

[46] Jason Etele, "Overview of Wind Gust Modelling with Application to Autonomous Low-Level UAV Control", *Carleton University*, Canada, 2006.

[47] I. Eliasson, B. Offerle, C.S.B. Grimmond, S. Lindqvist, "Wind fields and turbulence statistics in an urban street canyon", *Atmospheric Environment*, vol. 40, 2006.

[48] KAPER, Aerial Photography E-Resources, "Kite Flying Around Wind Obstacles", http://www.kaper.us/basics/BASICS_040502_hunt_windflow.html

[49] FLICKR, Urban Canyon in Chicago, "Urban Canyon", http://www.flickr.com/photos/ambimb/128954286/

[50] Geocities, "Canada and 9 Caribbean Islands", http://www.geocities.com/johnsquier/Caribbean/Caribbean.htm

[51] Wikimedia Commons, "Vancouver", http://commons.wikimedia.org/wiki/Image:Vancouver_downtown.jpg

[52] Alder-Weiner Research Company, "Adler-Weiner Chicago Qualitative Center", http://www.awres.com/QualitativeCenter/

[53] Zinester, "Great Escape", http://archives.zinester.com/50810/131333/210549_houston_downtown.jpg

[54] Britannica Online Encyclopedia, http://www.britannica.com/eb/art-74278/Downtown-Edmonton-stands-alongside-city-parkland

[55] Frank M. White, *Fluid Mechanics*. Fifth Edition, New York: McGraw-Hill, 2003.

[56] James A. Voogt, "Urban Heat Islands: Hotter Cities", actionbioscience.org, http://www.actionbioscience.org/environment/voogt.html, 2004.

[57] Vancouver weather data from the Government of Canada, http://vancouver.weatherstats.ca/wind_speed

[58] Y. Tominaga, A. Mochida, S. Murakami, S. Sawaki, "Comparison of various revised k-ϵ models and LES applied to flow around a high-rise building model with 1:1:2 shape placed within the surface boundary layer", *Journal of Wind Engineering and Industrial Aerodynamics*, vol. 96, 2008.

[59] T. Meng, K. Hibi, "Turbulent measurements of the flow field around a high-rise building", *Journal of Wind Engineering*, Jpn. vol. 76, 1998 (in Japanese).

[60] *CFX-5 Solver Theory*, ANSYS Canada Ltd., 2004.

[61] *CFX-Post Documentation*, ANSYS Canada Ltd., 2004.

[62] Unmanned Dynamics Ltd.,"AeroSim User Guide", http://www.u-dynamics.com, v1.2, 2002.

[63] M.J. Mahoney, "Pointing an Instrument on an Airborne Platform", http://mtp.jpl.nasa.gov/notes/pointing/pointing.html

[64] "Earth, size and shape of", *Grolier Encyclopedia of Knowledge*, Vol. 6, Connecticut: Grolier, 1991.

[65] Aerspaceweb.org, "Parts of an Aircraft", http://www.aerospaceweb.org/question/design/q0101.shtml

[66] Bernard Etkin, "Dynamics of Atmospheric Flight", John Wiley and Sons, Inc., 1972.

[67] W.E. Holley and A.E. Bryson Jr., "Wind modeling and lateral control for automatic landing", *Journal of Spacecraft*, vol. 14, February, 1977.

[68] Aerosonde Pty Ltd, Australia, *Technical Brief and Specifications Mk 4.1 Aerosonde*, May 2007.

[69] Aerosonde Pty Ltd, Australia, "Aircraft Overview", http://www.aerosonde.com/aircraft/

[70] Polecat Aeroplane Works, "Flight Path Geometry and Sideslip", http://www.polecataero.com/articles/using-the-rudder-in-thermal-flying/